Master's thesis

2019

Jonas Tjemsland

Master's thesis

NTNU
Norwegian University of
Science and Technology
Faculty of Natural Sciences
Department of Physics

Jonas Tjemsland

Antinuclei as a Signature of Dark Matter

May 2019

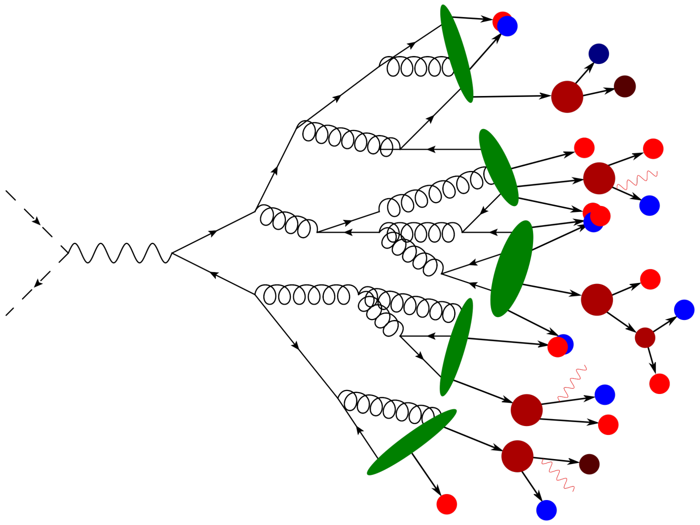

NTNU
Norwegian University of
Science and Technology

NTNU
Norwegian University of
Science and Technology

NTNU
Norwegian University of
Science and Technology

Antinuclei as a Signature of Dark Matter

Jonas Tjemsland

Master of Science (MSc) in Physics
Submission date: May 2019
Supervisor: Michael Kachelriess

Norwegian University of Science and Technology
Department of Physics

Abstract

Antideuteron and antihelium have been proposed as a detection channel for dark matter annihilation and decay in the Milky Way due to the low expected astrophysical background. Today it is common to use a coalescence model on an event-by-event basis in a Monte Carlo framework when estimating the antinucleus signal for both various dark matter models and the astrophysical background. However, this model lacks a microphysical picture and has been shown to not fit recent production spectra of antideuterons in proton-proton collisions well. Here we develop a new coalescence model for deuteron, helium-3, tritium and their antinuclei based on the Wigner function representations of the produced nuclei states. This approach includes both the size of the formation region, which is process dependent, and momentum correlations in a semi-classical picture. The model contains a single, universal parameter which is fixed by fitting the model to the production spectra of antideuterons in proton-proton interactions. Using this value, the model describes well the production of antideuteron in electron-positron annihilations and antihelium-3 in proton-proton collisions. The new coalescence model is in turn applied on the antideuteron and antihelium-3 production in dark matter annihilations and the secondary background in the Galaxy. The flux estimated using the new model differs at most by a factor 2–3 compared to the old model, which is small compared to the uncertainties related to the propagation through the Galaxy.

Sammendrag

Antideuteron og antihelium er blitt foreslått som en deteksjonskanal for spalting og annihilasjon av mørk materie i Melkeveien på grunn av en forventet lav astrofysisk bakgrunnstøy. I dag er det vanlig å bruke en standard partikkelvekstmodell per hendelse i en Monte Carlo simulering når antinukleussignalet fra både den mørke materien og bakgrunnsstøyen estimeres. Imidlertid mangler denne modellen et mikrofysisk bilde og har vist seg å ikke beskrive de siste produksjonsspekterene av antideuteron i proton-proton-kollisjoner godt. Her utvikler vi en ny partikkelvekstmodell for deuteron, helium-3, tritium og deres antinukleuser som er basert på å beskrive tilstanden til de produserte nukleusene som Wigner-funksjoner. Denne tilnærmingen gjør det mulig å inkludere både størrelsen på formasjonsregionen, som er prosessavhengig, og impulskorrelasjoner i et semi-klassisk bilde. Modellen inneholder en enkelt universell parameter som er fastsatt ved å tilpasse modellen til produksjonsspekterene av antideuteroner i proton-proton-kollisjoner. Denne verdien beskriver deretter bra produksjonen av antideuteron i elektron-positron-annihilasjoner og antihelium-3 i proton-proton-kollisjoner. Den nye partikkelvekstmodellen blir deretter benyttet på antideuteron- og antihelium-3-produksjon i annihalasjon av mørk materie og sekundær bakgrunnsstøy i galaksen. Den nye modellen gir på det meste en faktor 2–3 høyere fluks sammenlignet med den gamle modellen, som igjen er lite sammenlignet med usikkerhetene knyttet til nukleusenes forplantning gjennom galaksen.

Preface

This thesis is the result of research conducted during the two last semesters in the two-year Master of Science in Physics programme at the Norwegian University of Science and Technology (NTNU). First and foremost, I must thank my supervisor Prof. Michael Kachelrieß for invaluable guidance during this work. I am grateful for the support from the Research Council of Norway that made it possible for me to attend the 2nd antideuteron workshop at UCLA in Los Angeles 26th to 29th March 2019, as well as a short stay at Stanford, where I presented the main results of this thesis. I would also like to thank S. Ostapchenko for insights into the physical interpretation of the alternative formation model developed in this thesis, as well as collaborating on the paper published on the subject. At last, I am grateful for the support and encouragement from friends and family, in particular my beloved wife, during the past year.

Jonas Tjemsland

Jonas Tjemsland
15th May 2019
Trondheim, Norway

Contents

Abbreviations and notation

Abbreviations

CDM cold dark matter 12, 16, 18, 19

CMB cosmic microwave background 9, 12, 13, 17, 18

CoM centre-of-momentum 1, 39, 40, 44, 51, 53, 60, 66, 68, 70, 93, 97

DD double-diffractive 46

DGLAP Dokshitzer-Gribov-Lipatov-Altarelli-Parisi 34, 35

DM dark matter 1–9, 12, 13, 15–25, 33, 39, 41, 43, 44, 51, 75–78, 81–84, 86, 88–90

FRW Friedman-Robertson-Walker 9, 15

HDM hot dark matter 16, 17

ISM interstellar matter 24, 79, 80

LHC Large Hadron Collider 25, 46, 89

MC Monte Carlo 1, 2, 27, 35–39, 42, 45–47, 51, 53–56, 77, 89

MOND modified Newtonian dynamics 21, 22

ND non-diffractive 46, 47

NFW Navarro-Frenk-White 4–6, 82

QCD quantum chromodynamics 2, 19, 27–31, 37, 41, 60

QFT quantum field theory 21, 27, 37

SM Standard Model 13, 18–21, 23–25, 28, 30

SUSY supersymmetry 21, 25

WIMP weakly interacting massive particle 2, 3, 9, 13, 18–23, 75, 84–88, 90

Notation

Natural units with $\hbar = c = k_\mathrm{B} = 1$ will be used throughout this thesis. Three-vectors are denoted by boldface characters $\boldsymbol{V} = (V_x, V_y, V_z)$. Four-vectors are written with a Greek index as $V^\mu = (V^0, \boldsymbol{V})$. Moreover, $V \equiv |\boldsymbol{V}|$. The signature of the metric is chosen as -2, such that the metric tensor in Minkowski space becomes $\eta^{\mu\nu} = \mathrm{diag}(1, -1, -1, -1)$. Einstein's summation convention is used when an index repeat. If not otherwise stated, Greek indices $(\alpha, \beta, \gamma, ...)$ are used to index space-time, while Latin indices $(i, j, k, ...)$ are used to index Euclidean space. In other words, $x^i x^i \equiv x^1 x^1 + x^2 x^2 + x^3 x^3$ and $x^\alpha x_\alpha = x^0 x^0 - x^i x^i$. If the limits of an integral are not given, then it is assumed that the limits are set to infinity. For example,

$$\int f(\Omega)\, \mathrm{d}^d\Omega \equiv \int_{-\infty}^{\infty} f(\Omega)\, \mathrm{d}^d\Omega\,.$$

1 Introduction

Antideuteron and antihelium have been suggested as a promising detection channel for dark matter (DM) due to the low expected astrophysical background [1]. The process of computing the yields of these antinuclei in different DM models is usually split into three parts. First, a Monte Carlo (MC) event generator is used to compute the antiprotons and antineutrons resulting from DM annihilations or decays in the Milky Way. Next, a model that describes the formation of antinuclei from the antinucleons is employed. Finally, the antinucleus source spectrum is propagated through the Galaxy. The largest uncertainties in this scheme are related to the propagation models, while the second largest are related to the antideuteron formation model. Presently, the search for cosmic ray antinuclei is performed by the AMS-02 experiment on board the International Space Station, while the GAPS balloon experiment is expected to fly during the next solar minimum period around 2020 or 2021 [2, 3]. The AMS-02 experiment launched in 2011 and is expected to be in operation until 2024. No cosmic ray antideuterons have yet been observed. However, AMS-02 has reported the detection of six possible antihelium-3 events in the momentum range $< 100\,\mathrm{GeV}$, and even two possible antihelium-4 events [4].

The production of light clusters of (anti)nuclei like (anti)deuteron, (anti)helium-3 or (anti)tritium is usually described by coalescence models [5, 6]. That is, the formation is described by imposing a formation model on nucleons that have nearly completed their formation. In e^+e^- and DM annihilations, one imposes typically the coalescence condition in momentum space, requiring that any nucleons with a momentum difference Δk in the nucleon centre-of-momentum (CoM) frame less than some free parameter p_0 merge. Due to the lack of a microphysical understanding, p_0 must be calibrated by experimental data. Traditionally, the nucleon spectra were assumed to be uncorrelated and isotropic, in which case the coalescence condition could be applied on the average nucleon spectra resulting from a given process. However, this approximation does not hold in general [7]. When estimating the antinuclei yield, it is therefore today common to employ the coalescence condition on an event-by-event basis such that the nucleon correlations provided by MC simulations are taken into account [8].

The existing per-event coalescence model is phenomenological, lacks an underlying microphysical picture and the numerical value of its free parameter varies considerably between different experiments. In this thesis, an alternative per-event coalescence model for (anti)deuteron, (anti)tritium and (anti)helium-3 in phase space is therefore proposed. The model is based on the Wigner function representation of the nucleons and nucleus, which includes in a semi-classical treatment both the size of the formation region, which depends on the given process, and momentum correlations. In other words, it includes constraints on both space and momentum variables. The model contains a single, universal parameter that can be estimated from a microphysical picture. From the physical interpretation of the parameters as the spatial distribution of the formation process, we obtain $\sigma_{(e^+e^-)} = \sigma_{(pp)}/\sqrt{2} \simeq 5\,\mathrm{GeV}^{-1} \simeq 1\,\mathrm{fm}$. This value agrees well with the fit by experimental data on the production of antideuterons in pp-collisions at 0.9, 2.76 and 7 TeV [9]. Using this value, the model describes well the production of antihelium-3 in pp collisions and antideuteron production in e^+e^- annihilations at the Z resonance [10, 11].

Next, the detection prospects of cosmic ray antideuteron and antihelium-3 are discussed with a focus on the difference between the newly developed Wigner function based formation model and the old coalescence model. Contributions to the antinuclei yield from both the secondary background and DM annihilations are estimated. The propagation through the Galaxy is taken into account using the two-zone propagation model. The new Wigner function based coalescence model differs at most by a factor 2–3 compared to the old coalescence model, which is a small difference compared to the uncertainties related to the propagation through the Galaxy.

Thesis structure

This thesis consists of seven chapters including the introduction and conclusion. Below we outline the structure of the thesis and the content of each chapter.

The next two chapters serve as a motivation as well as an introduction to cosmic ray antinuclei and DM. In chapter 2, we discuss evidences for and general properties of DM with focus on weakly interacting massive particles (WIMPs) as a DM candidate. This will serve as a motivation for this work, as well as an introduction of DM properties that will become important in later chapters. Chapter 3 is dedicated to the discussion of basic properties of quantum chromodynamics (QCD) and MC event generators, which is the main tool used when estimating the particle production in various high energy collisions. In chapter 4, we discuss existing formation models for light nuclei and calibrate them to experimental data. The main focus is on the coalescence condition evaluated per-event within the MC. In chapter 5, we develop an alternative formation model and compare it to the existing state of the art per-event coalescence model. In chapter 6, we estimate the antideuteron and antihelium-3 flux on Earth from secondary production and WIMP annihilations in the Galaxy, with a focus on the difference between the old and new formation models. Finally, a conclusion is given in chapter 7.

In addition, this thesis includes three appendices. In appendix A, some important properties and formula from special relativity are reviewed. In appendix B, we review the subject of Wigner functions and Weyl transforms, stating amongst other the conventions used. Lastly, the relevant cross section parametrisations used when discussing the antinucleus propagation are listed in appendix C.

2 Dark matter and cosmology

One of the great unsolved puzzles in physics today is related to the existence of dark matter (DM). Despite an enormous amount of evidence for its existence, its nature has yet to be determined. This chapter is divided into five sections. In the first two sections, evidences for DM on galactic and galactic cluster scales are discussed. Next, DM on cosmological scales are discussed with focus on how DM fit into the standard cosmological picture as a thermal relic. Finally, the last two sections considers possible DM candidates and detection methods, with a focus on weakly interacting massive particles (WIMPs).

2.1 Dark matter in galaxies

2.1.1 Rotation curves

Arguably the most notable evidences for DM are related to measurements of the rotation curve of spiral galaxies, defined as the orbital speed $v(r)$ at a distance r from the galactic centre. The difference between the mass implied by the rotation curve and the luminosity serves as a strong evidence that most spiral galaxies are located in a large halo of DM [12]. This will now be discussed further.

Assume that the matter in a spiral galaxy follow circular orbits. The centripetal acceleration due to the circular motion at a distance r from the galactic centre is $a_r(r) = v(r)^2/r$. The ordinary mass in spiral galaxies can be well approximated by a thin disk with a small bulge around the galactic centre. It is common to assume that the mass distribution is proportional to the luminosity, which typically decreases exponentially as $L(r) = L_0 e^{-r/D}$ with $D \sim 5\,\mathrm{kpc}$ in spiral galaxies [13]. Thus, at large distances from the galactic centre, the gravitational force can be approximated by that of a central point mass. In this case, the acceleration due to Newtonian gravitation is $a_r(r) = GM(r)/r^2$, where $M(r)$ is the mass inside r and G is the gravitational constant. Equating the centripetal and gravitational accelerations yields

$$v(r) = \sqrt{\frac{GM(r)}{r}}. \tag{2.1}$$

In other words, one expects that the rotation curve decreases as $v(r) \sim 1/\sqrt{r}$ in the outer regions of the galaxies.

The rotation curve can be determined by measuring the Doppler shift of spectral lines from stars and gas at different distances from the centre of the galaxies [12, 13]. The general result is that few spiral galaxies exhibit the $1/\sqrt{r}$ decline in their rotation velocities as expected from the calculation above, which suggests that there are more matter in the galaxies than just the visible matter. As an example, consider the rotation curve of the Milky Way shown in figure 2.1. The rotation curve of the Milky Way is hard to measure and there are large uncertainties at large r mainly due to poorly known distances. In any case, the general behaviour is clear: at large distances, the rotation curve remains more or less constant.[1] In order to explain the discrepancy, one may include a spherically symmetric mass distribution known as the dark halo, as shown in figure 2.1. This leads to a lower bound on the DM density in the Galaxy of $\Omega_{\mathrm{DM}} \gtrsim 0.1$, where $\Omega_X \equiv \rho_X/\rho_{\mathrm{crit}}$ [14].

2.1.2 Density profiles

This thesis will focus on antinucleus production in DM annihilations. In order to estimate the final flux at Earth, one must have a model for the distribution of the DM in the Galaxy. We will consider three profiles often used in the literature: the isothermal, Navarro-Frenk-White (NFW) and Einasto profiles.

Isothermal Profile

As discussed above, the rotation curve $v(r)$ for most spiral galaxies remains constant at large r. This can be explained by assuming that the galaxies are located in the centre of a spherically symmetric mass distribution with a density profile $\rho(r)$. The mass located within a sphere of radius r is

$$M(r) = \int_0^r 4\pi r^2 \rho \,\mathrm{d}r\,. \tag{2.2}$$

By using equation (2.1) and solving for $\rho(r)$, one obtains the density profile

$$\rho(r) = \frac{v^2}{4\pi G r^2}. \tag{2.3}$$

Thus, the DM density must decrease as $1/r^2$ at large r to describe the behaviour of the rotation curve. This is much slower than the visible matter, which roughly follow he exponential decrease in luminosity.

The density profile in equation (2.3) is only suitable to describe the density in the regions of constant rotation curve. Furthermore, the profile yields a constant rotation

---

[1] Measurements of objects that are not a part of the disk, such as globular clusters and dwarf galaxies, show that $v(r)$ remains constant until $\sim 100\,\mathrm{kpc}$ and then decreases until $\sim 300\,\mathrm{kpc}$ [12]. This is quite impressive considering that the Andromeda Galaxy has a diameter of $\sim 20\,\mathrm{kpc}$ and is a distance $\sim 700\,\mathrm{kpc}$ from the Milky Way.

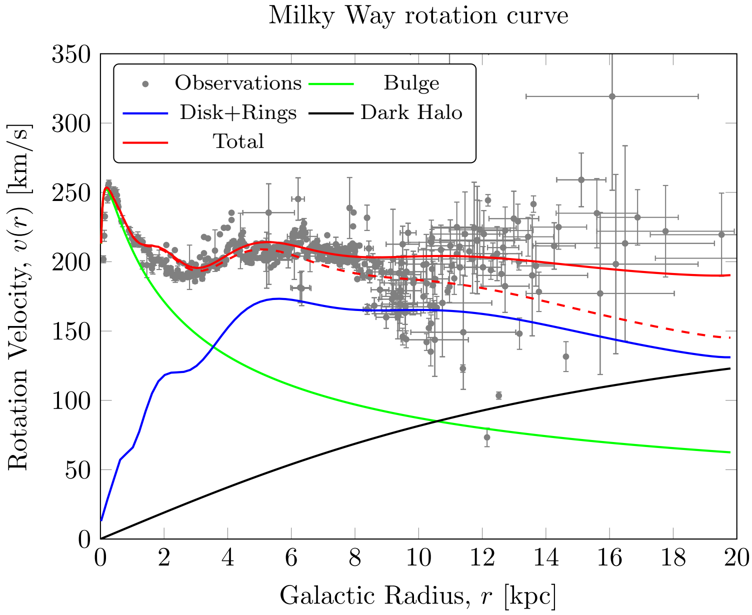

Figure 2.1: Parametrisation of the Milky Way rotation curve by Sophue et al. (2009) [15] at $r \lesssim 20\,\mathrm{kpc}$. The experimental data were measured using amongst other HI, HII and CO tangent lines (see Refs. [12, 15] and references therein). The total rotation curve (solid red) is decomposed into the contributions from the bulge (green), disk (blue) and dark halo (black). The contribution from the bulge and disk alone (dashed red) cannot explain the data at large r. Other characteristics, such as the dip at $\sim 9\,\mathrm{kpc}$, can be reproduced by considering additional perturbations.

curve even for low r and has thus a mass singularity at $r = 0$. This problem can be fixed by introducing a finite core radius $a \neq 0$ in such a way that $\rho(r)$ is constant for $r \ll a$. This leads to the so-called *isothermal profile* [16]

$$\rho_{\mathrm{iso}}(r) = \frac{\rho_s}{1 + (r/a)^2}, \tag{2.4}$$

where a and ρ_s are parameters that must be determined by experiments for each galaxy.

NFW profile

The DM density profile in a large mass range, from micro-halos to galaxy clusters, can be approximated by the *NFW profile*

$$\rho(r) = \frac{\rho_s}{(r/a)^\gamma (1 + r/a)^{3-\gamma}}, \tag{2.5}$$

where $\gamma = 1$ [17, 18], which was empirically obtained using N-body simulations of galaxy formation. Note that this profile behaves as $\sim r^{-1}$ for small r and $\sim r^{-3}$ for large r and does not include the contribution from the baryonic feedback from stars. Thus, it does not necessarily describe a dynamically relaxed system. Regardless, it is today one of the most used DM density profiles.

Einasto profile

Newer and larger simulations reveals that most halos are significantly denser than the best-fit NFW-profile, and that some halos follow the NFW profile well, while others are better approximated by a steeper profile [18]. Improved fits require additional free parameters, such as making γ in equation (2.5) a free parameter. Alternatively, one may use the *Einasto profile* [18]

$$\rho(r) = \rho_s \exp\left\{-\frac{2}{\alpha}\left[\left(\frac{r}{a}\right)^{\alpha} - 1\right]\right\}, \tag{2.6}$$

where α is an additional free parameter, that been shown to describe N-body haloes even better than the NFW profile.

Profile parameters

The profile parameters can be estimated using N-body simulations or by fitting the models to experimental data. We will be using the parameters given by Ref. [19] and listed in table 2.1. These parameters are found by fitting the profiles to the local DM density $\rho_\odot$ and the total DM mass contained within a radius of 60 kpc. We follow Ref. [19] and assume that $\rho_\odot = 0.3\,\mathrm{GeV/cm^3}$ and that the distance to the galactic centre is $r_\odot = 8.3\,\mathrm{kpc}$. Note that there are large uncertainties in these parameters. For example, $\rho_\odot$ is only determined within a factor 2–3 [14].

Table 2.1: Best fit parameters for the NFW, Einasto and isothermal profiles, taken from Ref. [19].

Profile	a [kpc]	ρ_s [GeV/cm^3]	α
NFW	24	0.18	-
Einasto	28	0.033	0.17
Isothermal	4.4	1.4	-

2.2 Dark matter in cluster of galaxies

2.2.1 The virial theorem and the Coma Cluster

One of the first evidences for DM were put forward by the Swiss astronomer Fritz Zwicky in 1933 after he estimated the mass of the Coma Cluster using the virial theorem. It can be shown (see e.g. Ref. [20] for a simple proof) that the potential energy U of a gravitationally bound and dynamically relaxed system can be written as

$$U = \frac{1}{2}\sum_{i=1}^{N}\sum_{j=1,j\neq i}^{N} G\frac{m_i m_j}{|\boldsymbol{r}_j - \boldsymbol{r}_i|} = \frac{1}{2}\frac{\mathrm{d}^2}{\mathrm{d}t^2}\sum_{i=1}^{N} m_i \boldsymbol{r}_i^2 - 2T, \tag{2.7}$$

where the sum runs over the particles in the system and $T = \sum_i m_i v_i^2/2$ is the total kinetic energy. Time averaging over a sufficiently large time yields

$$\langle U \rangle = -2\langle T \rangle , \tag{2.8}$$

which is the simplest form of the virial theorem for a gravitationally bound and dynamically relaxed system. The gravitational potential energy of a system can in general be written on the form

$$\langle U \rangle = -\alpha \frac{GM^2}{r}, \tag{2.9}$$

where $\alpha = \mathcal{O}(1)$ and r is a characteristic radius of the system. For a galaxy cluster it is observed that $\alpha \approx 0.4$ and $r = r_h$, where r_h is the radius that contains half the total mass, is a good choice [20]. Inserting equation (2.9) into the virial theorem (2.8) and solving for M yields

$$M = \frac{\langle v^2 \rangle r_h}{\alpha G}. \tag{2.10}$$

We can now estimate the mass of the Coma cluster using the numerical values given in Ref. [20]. The velocity dispersion along the line of sight is found, using redshift measurements, to be $\langle v_r^2 \rangle \approx 880\,\mathrm{km/s}$. Assuming that the velocity dispersion is isotropic, the mean square velocity is simply $\langle v^2 \rangle \approx 3\times 880\,\mathrm{km/s}$. Estimating the half-mass radius r_h of a galaxy cluster is quite difficult, but assuming that the mass-to-light ratio is constant and that the cluster is spherical, it can be approximated using the luminous matter. The observed distribution of the galaxies in the Coma Cluster indicates $r_h \approx 1.5\,\mathrm{Mpc}$. The aforementioned numerical values inserted into equation (2.10) gives an estimated mass $M_{\mathrm{Coma}} \approx 2 \times 10^{15} M_\odot$. On the other hand, the mass of X-ray emitting gas is estimated to be $M_{\mathrm{Coma,gas}} \approx 2 \times 10^{14} M_\odot$ while the mass of the stars is estimated to be $M_{\mathrm{Coma,stars}} \approx 3 \times 10^{13} M_\odot$. This means that less than $2\,\%$ of the mass of the Coma cluster comes from stars and about $10\,\%$ from observable intracluster gas, the rest being DM. Note, however, that we cannot deduce from these estimates whether the DM is baryonic or not.

2.2.2 Gravitational lensing and the Bullet Cluster

In the previous subsection we saw how the virial theorem could be used to estimate the mass of a galactic cluster and how a potential discrepancy compared to the luminous matter is an indication of the existence of DM. Another method to estimate the mass is by using gravitational lensing. According to Einstein's general theory of relativity (see section 2.3.1) the trajectory of photons is deflected by a point mass by an angle proportional to the mass and inversely proportional to the impact parameter b [20]. Thus, by measuring the angle of deflection of photons from distant objects, one can in principle estimate the mass of galaxies and galactic clusters.

A more compelling evidence lies in the possibility of using gravitational lensing to create a lensing map. The "Bullet Cluster" (1E0657-56) and more recently the lensing cluster MACS J0025.4-1222, give an unique picture of the nature of DM [18]. These clusters consist in fact of two clusters each that merged recently on cosmological time scales. In both clusters, the gravitational lensing reveals two substructures that are offset compared to the baryon distribution observed by X-ray, as shown in figure 2.2. In other words, the baryonic mass decelerated in the collision, whereas most of the total mass moved ballistically. This indicates both the existence of DM and that the DM is weakly interacting.

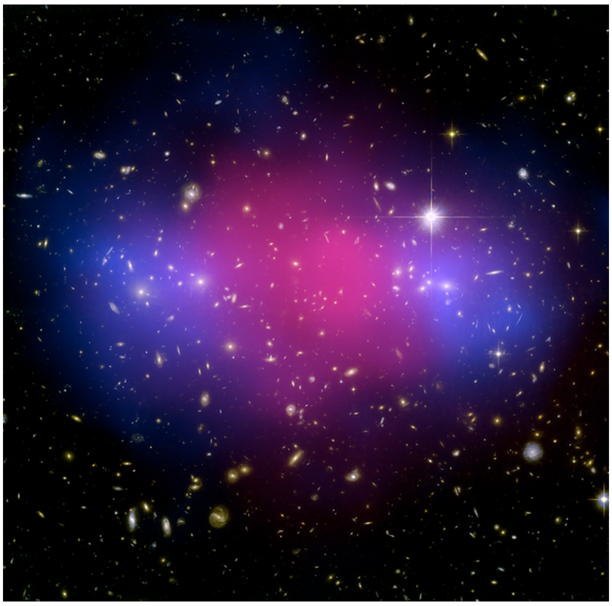

Figure 2.2: Lensing mass (blue), X-ray map (pink) and optical map of the MACS J0025.4-1222 cluster [21]. The image shows a system where two Galaxy clusters have collided, creating a separation between the visible baryonic mass and the total mass. Image credit: X-ray (NASA/CXC/Stanford/S. Allen); Optical/Lensing (NASA/STScI/UC Santa Barbara/M. Bradac)

2.3 Dark matter on cosmological scales

The existence of DM has a profound impact on the evolution of Universe and cosmological studies may thus impose constraints on possible DM candidates. An introduction to cosmology is therefore called for. In this section, we will include an introduction to the standard cosmological picture and discuss how WIMPs, which are the favoured DM candidates, fits this picture as a thermal relic. In addition, we will discuss how the cosmic microwave background (CMB) is used to estimate the non-baryonic DM content in the Universe. Most of the content of this section is discussed in amongst other Refs. [14, 20, 22].

2.3.1 Curvature of space

The cosmological principle is a central concept of modern cosmological models. It states that the Universe is homogeneous and isotropic on large scales at each moment of its evolution. In other words, the observed general properties, such as energy density, are the same for all observers in all directions. This does of course not hold for small scales, say our Solar system or our Galaxy. Note that a space that is isotropic around two or more points is also homogeneous, but a homogeneous space is not necessarily isotropic. Observations of the CMB (see section 2.3.3) indicate that the Universe is perceived as isotropic from Earth. Nothing indicates that the location of our Solar system and Galaxy is special, and so the Universe must in fact be homogeneous and isotropic.

The homogeneity and isotropy of the Universe can be used to create a model that describes the overall geometry and evolution of space. The homogeneous and isotropic Universe can in polar coordinates be described by the line element

$$\mathrm{d}s^2 = \mathrm{d}t^2 - a^2(t)\left[\frac{\mathrm{d}r^2}{1-kr^2} + r^2\left(\mathrm{d}\theta^2 + \sin^2\theta\,\mathrm{d}\phi^2\right)\right], \tag{2.11}$$

where $a(t)$ is the time dependent scale factor and k is the curvature parameter. This metric is known as the Friedman-Robertson-Walker (FRW) model when $a(t)$ is chosen such that the metric obeys the Einstein equation. At any time t, the coordinate r can be rescaled as $R = a(t)r$, which keeps the geometry intact. The normalisation $a(t_0) = 1$, where t_0 is the present time, is often used. The distribution of galaxies must be smoothed out in the FRW model, i.e. the velocity of individual galaxies must be zero.[2] One can thus choose a coordinate system in which each galaxy remains at the fixed position (r_i, θ_i, ϕ_i) as space expands and increases the distance between the galaxies. This is known as *comoving* coordinates.

By rescaling the radial coordinate, the curvature parameter k can be chosen to take only the three discrete values $k = \{0, +1, -1\}$, which corresponds to a flat, closed and

---

[2] The motion of individual galaxies can be diffusive and "random", as this does not violate the homogeneity.

open universe, respectively. The space in a flat universe is Euclidean and is of infinite size, a closed universe has a spherical geometry and is of finite size, while an open universe has a hyperbolic geometry and is of infinite size.

The curvature of space-time is described by the Einstein equation,

$$G_{\mu\nu} = 8\pi G T_{\mu\nu} + \Lambda g_{\mu\nu}, \tag{2.12}$$

where $G_{\mu\nu} = R_{\mu\nu} - g_{\mu\nu}R/2$ is the Einstein tensor, G is the Newtonian gravitational constant, $T_{\mu\nu}$ is the energy-momentum tensor and Λ is the cosmological constant. This equation describes the relationship between the curvature of space-time and the energy-momentum content. In other words, it describes how energy and momentum curve space-time. It is common to assume that the content of the Universe is a perfect fluid. For a specific frame the energy-momentum tensor for the perfect fluid is

$$T_{\mu\nu} = \mathrm{diag}(P, \rho, \rho, \rho) = -P g_{\mu\nu} + (P + \rho) u_\mu u_\nu, \tag{2.13}$$

where $g_{\mu\nu}$ is the metric described by equation (2.11), P is the isotropic pressure, ρ is the energy density and u_μ is the four-velocity ($u = (1, 0, 0, 0)$ in comoving coordinates).

Inserting the FRW metric (2.11) and the energy-momentum tensor for a perfect fluid (2.13) into the Einstein equation (2.12) leads to the Friedmann equations

$$H^2 \equiv \left(\frac{\dot{a}}{a}\right)^2 = \frac{8\pi}{3} G\rho - \frac{k}{a^2} + \frac{\Lambda}{3}, \tag{2.14}$$

and

$$\frac{\ddot{a}}{a} = \frac{\Lambda}{3} - \frac{4\pi G}{3}(\rho + 3P), \tag{2.15}$$

where we defined the Hubble parameter $H(t) = \dot{a}(t)/a(t)$. These equations can be used to describe the evolution of the Universe. At the present time, $H_0 = \dot{a}(t_0)/a(t_0)$, where $H_0 = 100h\,\mathrm{km\ s^{-1}Mpc^{-1}}$ with $h \simeq 0.678$ is the Hubble constant.[3] In other words, the present day Universe is expanding.

2.3.2 Constituents of the Universe

When discussing the energy density contribution of different constituents of the Universe, it is common to express it in terms of the relative fractions

$$\Omega_i \equiv \frac{\rho_i}{\rho_\mathrm{c}} = \frac{8\pi G}{3H^2}\rho_i, \tag{2.16}$$

where i can be mass (m), radiation (r) or vacuum (v). Here $\Omega \equiv \Omega_\mathrm{m} + \Omega_\mathrm{r} + \Omega_\mathrm{v} = 1$ corresponds to a flat universe, $\Omega < 1$ corresponds to an open universe and $\Omega > 1$

---

[3] Hubble's law follows in the approximation of small redshift.

corresponds to a closed universe. The energy density required to obtain a flat universe ($k = 0$) is denoted by ρ_c and called the *critical density*. Current measurements indicates in fact that the Universe is close to flat. Solving the Friedman equation (2.14) for ρ gives

$$\rho_\mathrm{c} = \frac{3H^2}{8\pi G}. \tag{2.17}$$

The effect on the evolution of the Universe from the different constituents can be found using the useful equation

$$\dot{\rho}(t) = -3H(\rho + P) \tag{2.18}$$

which follows directly from equations (2.14) and (2.15). Alternatively, it can be derived from the first law of thermodynamics in an adiabatic evolution of the Universe. Using this equation, one can find the time dependence of the scale factor $a(t)$. However, one must first find the relation between the pressure P and energy density ρ of the different constituents.

Matter Matter can be well approximated by a pressureless gas, $P = 0$. The energy density ρ_m is thus just the rest energy of the matter. Note that relativistic matter, such as relativistic neutrinos, are often included in the radiation content.

Radiation The energy density ρ_r and pressure P_r for a photon gas are related by (see section 2.3.4)

$$P_\mathrm{r} = \frac{1}{3}\rho_\mathrm{r}. \tag{2.19}$$

Vacuum Finally, consider the effect of the cosmological constant Λ in the Einstein equation (2.12). The cosmological constant Λ measures the curvature of an empty classical space-time. Its effect is equivalent to a stress tensor $T_{\Lambda\mu\nu} = \Lambda g_{\mu\nu} 8\pi G$, which contributes to either expansion or contraction of the Universe. Thus Λ corresponds to a non-zero energy density $\rho_\Lambda \equiv \Lambda/8\pi G$, often referred to as a vacuum energy density. Comparing the energy-momentum tensor $T_{\Lambda\mu\nu}$ to that of a perfect fluid (eq. (2.13)) yields

$$P_\mathrm{v} = -\rho_\mathrm{v}. \tag{2.20}$$

Thus, a positive vacuum energy density implies a negative pressure which accelerates the expansion of the Universe. This is known as dark energy. There is currently no fundamental theory for the cosmological constant, and it is thus common to assume that it is constant and positive, as indicated by present observations.

The evolution of the Universe can be found by using the general pressure and energy density relation, $P = w\rho$, in equation (2.18). The result is

$$\rho(t) \propto a^{-3(1+w)}. \tag{2.21}$$

Using then the Friedmann equation (2.14), gives the time dependence of the scale factor,

$$a(t) \propto t^{2/(3+3w)} = \begin{cases} t^{3/2} & \text{for matter } (w = 0), \\ t^{1/2} & \text{for radiation } (w = 1/3), \\ \mathrm{e}^t & \text{for vacuum } (w = -1). \end{cases} \tag{2.22}$$

In all three cases, the Universe expands without limit. In the early hot and dense Universe, one can approximate the state as only consisting of relativistic matter. At later times, the non-relativistic matter will dominate over the radiation. Eventually, the energy density will be dominated by Λ. In the radiation and matter dominated universe, the Universe starts from a singularity and a hot Big Bang. However, it is important to note that one expects the classical gravity to break down when $\rho \sim M_{\mathrm{Pl}}^4$. DM will contribute to the energy content of the Universe, and has thus a large impact of its evolution. In addition, DM is a crucial part of, amongst other, structure formation, but this will not be discussed here.

2.3.3 Cosmic microwave background radiation

The total amount of DM in the Universe can be obtained by studying the observed CMB anisotropies shown in figure 2.3. Until recombination, when the Universe was about 378,000 years old, the photons were strongly coupled to a sea of electrons and baryons through scattering with the electrons. At some time however, the Universe was cold enough to allow electrons and protons to combine and form atoms. This allowed the photons to decouple and create a free stream of photons that constitutes the CMB one observes at Earth today. The CMB is today well described by black-body radiation with a temperature $T_0 = 2.73\,\mathrm{K}$, but shows tiny temperature fluctuations corresponding to small regions of different densities that evolved into the stars and galaxies we see today.

One can get a good deal of information about the early Universe by studying the deviations from the Planckian spectrum. This is usually done by studying the temperature anisotropies at or below the 10^{-6} level. The anisotropies are usually expressed as an expansion of the CMB in spherical harmonics [14, 23]:

$$T(\theta, \phi) = \sum_{lm} a_{lm} Y_{lm}(\theta, \phi). \tag{2.23}$$

The monopole term corresponds to the mean temperature $T = 2.73\,\mathrm{K}$. The largest anisotropy is the dipole term $l = 1$, and is interpreted as being the Doppler boost of the monopole. Hence, the dipole term becomes a frame dependent quantity that can be used to determine the absolute rest frame of to the CMB. In the study of higher order multipoles, the dipole contribution is usually removed, as is the case in figure 2.3. By studying the higher order multipoles in certain cosmological models, it is possible to constrain cosmological parameters. The current recommended values related to the constituents of the Universe are $\Omega_{\mathrm{b}} h^2 = 0.02226 \pm 0.00023$ (baryonic matter density), $\Omega_{\mathrm{c}} h^2 = 0.1186 \pm 0.0020$ (cold non-baryonic matter), $h = 0.678 \pm 0.09$, $\Omega_\Lambda = 0.692 \pm 0.12$ (cosmological constant) and $\Omega_{\mathrm{tot}} = 1.0002 \pm 0.0026$ [14, 23]. Thus, the Universe is close to flat and its energy content consists of about 69 % dark energy and 26 % DM in the form of cold dark matter (CDM) (see section 2.3.4).

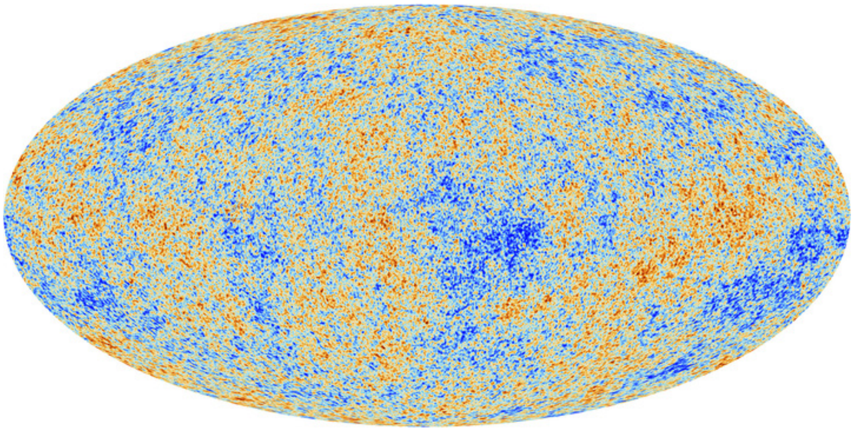

Figure 2.3: Temperature map of the CMB anisotropies from 2013 as observed by ESA's Planck mission [24]. The temperature fluctuations are indicated by colour differences, with a temperature range of $\pm 200\,\mu$K. Image credit: ESA/Planck Collaboration

Perhaps more important than the constraints on cosmological parameters, the CMB has lead to new insights into the early Universe and structure formation. In addition, it is perceived by many as the most important evidence for the existence of DM. These features, together with the basic evolution described earlier and the thermal freeze-out of DM described in the next subsection, constitute the basis for the standard model of cosmology, ΛCDM.

2.3.4 Thermal history, thermal relics and the WIMP miracle

Now that the fundamental understanding of the evolution of the Universe and DM is set, we can turn to the question of how there can be a non-zero abundance of DM at all. As mentioned before, the main focus of this thesis will be on WIMPs as candidates for DM. We will therefore now discuss how particle DM can fit into the standard cosmology as a thermal relic, and how this favours WIMPs as DM candidates. That is, the WIMPs were once in thermal equilibrium with Standard Model (SM) particles, but at some point they went out of equilibrium to create the DM abundance we observe today. In the previous subsections, the evolution of the Universe was assumed to be adiabatic. This is a good approximation in most of the evolution. However, in order to explain the present Universe, deviations must be taken into account. The discussions in this subsection follow Refs. [18, 22, 25].

Equilibrium statistical physics

Before one starts discussing thermal relics, one should recall some basic equilibrium statistical physics. The one-particle distribution function of a free gas in kinetic equilibrium is given by

$$f(p) = \frac{1}{\exp[\beta(E-\mu)] \pm 1}, \tag{2.24}$$

where $\beta = 1/T$ and μ is the chemical potential. This equation describes the expected number of particles in a given energy state $E = \sqrt{m^2 + \boldsymbol{p}^2}$. The lower sign $(-)$ gives the Bose-Einstein statistics for bosons, while the upper sign $(+)$ gives the Fermi-Dirac distribution for fermions. The number density n, energy density ρ and pressure P can be written in terms of the one-particle distribution function $f(p)$ as[4]

$$n = g \int \frac{\mathrm{d}^3 p}{(2\pi)^3} f(p), \quad \rho = g \int \frac{\mathrm{d}^3 p}{(2\pi)^3} E f(p), \quad P = g \int \frac{\mathrm{d}^3 p}{(2\pi)^3} \frac{p^2}{3E} f(p), \tag{2.25}$$

where g accounts for the internal degrees of freedom. For example, $g = 2$ for photons because they are massless spin-1 particles. In the non-relativistic limit $T \ll m$, this reduces to the classical Maxwell-Boltzmann statistics,

$$n = g \left(\frac{mT}{2\pi}\right)^{3/2} \exp\{-\beta(m-\mu)\}, \tag{2.26}$$

which implies that the number of non-relativistic particles is exponentially suppressed for a small chemical potential μ. In the relativistic limit $T \gg m$ and $T \gg \mu$, equation (2.25) becomes

$$n = \frac{gT^3}{2\pi^2} \int_0^\infty \frac{x^2}{e^x \pm 1} \propto T^3, \tag{2.27a}$$

$$\rho = 3P = \frac{gT^4}{2\pi^2} \int_0^\infty \mathrm{d}x \, \frac{x^3}{e^x \pm 1} \propto T^4. \tag{2.27b}$$

Since the non-relativistic species are suppressed, the pressure and energy density in the Universe can be approximated by the relativistic species as

$$\rho_{\text{rad}} = 3P_{\text{rad}} = \frac{\pi^2}{30} g_* T^4, \tag{2.28}$$

where $g_* = g_*(T)$ is an effective relativistic degree of freedom.

From the second law of thermodynamics, $T \, \mathrm{d}S = \mathrm{d}U + P \, \mathrm{d}V$ and $U \equiv \rho V$, one finds $\mathrm{d}S = \mathrm{d}[(\rho + P)V/T]$, implying that

$$S = \frac{\rho + P}{T} V. \tag{2.29}$$

---

[4] The expression for the pressure can either be taken as a definition in itself, or be derived by considering the usual definition of pressure as the momentum flux through a surface.

This has two important consequences. Firstly, using equation (2.28), one finds

$$s = \frac{2\pi^2}{45} g_{*s} T^3, \tag{2.30}$$

where now $g_{*s} = g_{*s}(T)$ is the effective degree of freedom for the entropy density. Secondly, using the continuity equation (2.18) and equation (2.28), one can show that $\mathrm{d}S \,/\, \mathrm{d}t = 0$. Thus, the entropy S is conserved in an early FRW universe. In fact, the baryon to photon ratio $\eta \approx 6 \times 10^{-10}$ in our Universe is extremely small, implying that the entropy is still approximately constant. Since both n and s scales as $\propto a^{-3}$, it convenient to consider the time evolution of the parameter $Y \equiv n/s$.

Dark matter as thermal relics

As can be seen from equations (2.30) and (2.22), the temperature in the radiation dominated period of the early Universe scales as $T \propto a^{-1} \propto t^{-1/2}$. This large temperature had several effects. Atoms, nuclei and even hadrons are dissolved in the epoch where the temperature exceeds the corresponding binding energies, $T \gtrsim B$. Furthermore, particles with masses m_X can be produced in interactions like $\bar{Y}Y \leftrightarrow \bar{X}X$ when $T \gtrsim 2(m_X - m_Y)$. For DM particles, the interactions[5]

$$\chi\bar{\chi} \leftrightarrow e^+e^-, \mu^+\mu^-, q\bar{q}, W^+W^-, ZZ, HH, ..., \tag{2.31}$$

would be efficient at temperatures $T \gg m_i$ ($i = \chi, e^-, q, ...$). It is thus often assumed that the DM production and annihilation reactions were initially in equilibrium. The common rate of production and annihilation at chemical equilibrium can be written as

$$\Gamma_{\mathrm{ann,eq}} = \langle \sigma_{\mathrm{ann}} v \rangle \, n_{\mathrm{eq}}, \tag{2.32}$$

where σ_{ann} is the DM annihilation cross section, v is the relative velocity of the two DM particles and n_{eq} is the DM number density. Assuming that the production and annihilation processes remained in thermal equilibrium, the number of produced DM particles decreased exponentially with decreasing temperature, as determined by the Maxwell-Boltzmann distribution (2.26). Since the number density increases as $n \propto a^{-3} \propto T^3$ and the expansion rate of the Universe increases as $H = \dot{a}a^{-1} \propto T^2$, most scattering rates $\Gamma = n\sigma v$ increase faster than the expansion rate of the Universe for $t \to 0$. The *Gamov criterion* tells us that a reaction becomes ineffective if its rate Γ drops below the expansion rate H. Thus, at some time, the DM particles went out of chemical equilibrium.[6] This is known as chemical freeze-out, and may be an explanation of the abundance of

---

[5] The DM particles should be chargeless and cannot therefore interact with the photon.

[6] Alternatively, the interaction rate may drop below the expansion rate due to decreasing cross section, but this will not be discussed.

DM observed today. At a later time, energy transfer processes like $\chi\nu \to \chi\nu$ became ineffective, taking the DM particles out of thermal equilibrium. This is known as kinetic freeze-out. We will next consider the chemical freeze-out in more detail.

The evolution of the number density of a thermal relic, $\mathrm{d}N_X/V = \mathrm{d}(a^3 n_X)/a^3$, in the expanding Universe is determined by the interaction rate $\Gamma n_X = \langle\sigma_{\mathrm{ann}}v\rangle n_X^2$. At chemical equilibrium, the evolution should be zero. These observations lead to the Boltzmann equation (see [22] for a more thorough derivation)

$$\frac{1}{a^3}\frac{\mathrm{d}}{\mathrm{d}t}\left(a^3 n_X\right) = -\left\langle\sigma_{\mathrm{ann}}v\right\rangle\left(n_X^2 - n_X^{\mathrm{eq}2}\right). \tag{2.33}$$

Assume that the freeze-out occurs in the radiation dominated period of the Universe. Then, equation (2.22) gives $H = \dot{a}/a = 1/2t$. Using the dimensionless variables $x \equiv m/T$ and $Y \equiv n/s$ and the constant entropy, $\mathrm{d}S/\mathrm{d}t = 0$, one can recast the Boltzmann equation (2.33) as

$$\frac{x}{Y_{\mathrm{eq}}}\frac{\mathrm{d}Y}{\mathrm{d}x} = -\frac{\Gamma_{\mathrm{ann,eq}}}{H}\left[\left(\frac{Y}{Y_{\mathrm{eq}}}\right)^2 - 1\right], \tag{2.34}$$

which makes the previous intuitive Gamov criterion more clear: The relative change of the comoving number density Y is determined by $\Gamma_{\mathrm{ann,eq}}/H$ multiplied by the deviation from equilibrium. When $\Gamma_{\mathrm{ann,eq}} \sim H$, Y flattens out. That is, the reaction is no longer efficient and the DM particles goes out of equilibrium. Equation (2.34) can now in principle be solved numerically. Note, however, that the thermally averaged cross section $\langle\sigma v\rangle$ depends on the amplitudes $|\mathcal{A}_{fi}|^2$ of the allowed DM processes and is thus model dependent. In any case, one can gain more insight by considering approximate solutions in the two limiting cases $x_f \ll 3$ and $x_f \gg 3$, known as hot dark matter (HDM) and CDM, respectively. Here, x_f refers to the temperature at which freeze-out occurs. Some typical evolutions of $Y(x)$ are plotted in figure 2.4 in the case $x_f \gg 3$ with $\langle\sigma_{\mathrm{ann}}v\rangle = 3 \times 10^{-26}\,\mathrm{cm}^3/\mathrm{s}$. From this figure, it is clear that the thermal relics were once in equilibrium and at some point they froze out such that their comoving number densities Y flattened out.

Hot dark matter

In the case of HDM, the freeze-out occurs while the particles are still relativistic. In this case, $Y_{\mathrm{eq}} = n_X/s$ is constant. Thus, the limiting abundance at $t \to \infty$ is given by the equilibrium abundance at freeze-out, $Y_\infty \equiv Y(x \to \infty) = Y_{\mathrm{eq}}$. Dividing (2.27a) by (2.30) in the limit $x \ll 3$ yields

$$Y(x \to \infty) = Y_{\mathrm{eq}}(x_f) = 0.278\frac{g_{\mathrm{eff}}}{g_{*s}(x_f)}, \tag{2.35}$$

where g_{eff} is the effective number of degrees of freedom of the DM particles and the only temperature dependence is in g_{*s}. The entropy density in the present Universe, s_0 can

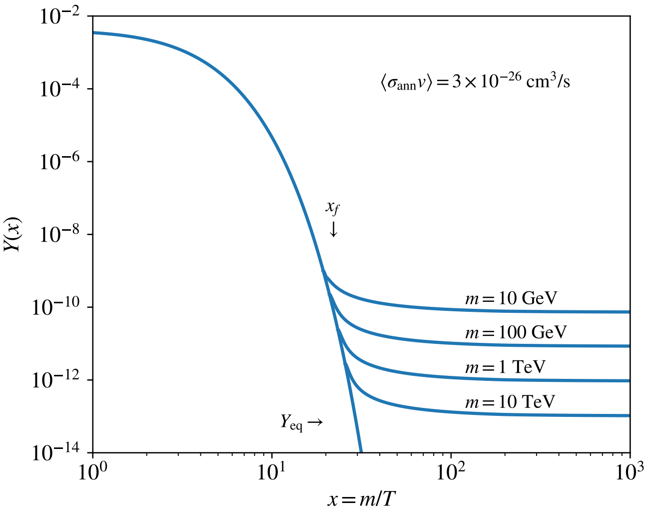

Figure 2.4: Illustration of the freeze-out process with $\langle\sigma_{\mathrm{ann}}v\rangle = 3\times10^{-26}\,\mathrm{cm}^3/\mathrm{s}$ and DM masses $m = \{10, 10^2, 10^3, 10^4\}$ GeV.

be estimated using equation (2.30) with the current temperature of the CMB photons, $T_0 \approx 2.73\,\mathrm{K}$, and the effective degrees of freedom of photons and neutrinos, $g_{*s,0} \approx 3.9$.[7] This leads to $s_0 \approx 2.9\times10^3\,\mathrm{cm}^{-3}$. Particles with masses $m \gg T_0 \sim 0.2\,\mathrm{meV}$ that were relativistic at freeze-out will be non-relativistic today. Their energy density is thus $\rho_0 = mn_0 = ms_0Y_\infty$ and their abundance becomes

$$\Omega h^2 = \frac{\rho_0}{\rho_{\mathrm{cr}}} = 7.6\times10^{-2}\frac{m}{\mathrm{eV}}\frac{g_{\mathrm{eff}}}{g_{*s}}. \tag{2.36}$$

Thus, the abundance of possible HDM particles with $m \lesssim 7\,\mathrm{eV}$ exceeds the observed pressureless matter density of the Universe, $\Omega_{\mathrm{m}}h^2 = \Omega_{\mathrm{c}}h^2 + \Omega_{\mathrm{b}}h^2 = 0.141$, assuming a spinless DM particle.

The lower bound on the sum of the neutrino masses is $\sum_\nu m_\nu > 0.06\,\mathrm{eV}$ and at least two of the neutrinos are non-relativistic today [14]. This makes the neutrinos suitable candidates for HDM. Assuming that all three neutrino species are non-relativistic, equation (2.36) gives the upper bound $\Omega_\nu h^2 \lesssim 0.006$ for the contribution from the neutrinos on the non-baryonic matter in the Universe. This indicates that most of the DM in the Universe are dynamically cold.

---

[7] The neutrinos froze out early while still relativistic, creating a neutrino background that still should be present. After the freeze-out of the electron and positron, the remaining pairs would translate their entropy to the photon species through the annihilation process $e^+ + e^- \to \gamma + \gamma$. This would increase the photon entropy as $s'_\gamma = (7/8 + 7/8 + 1) = 11/4s_\gamma$, where the factor 7/8 comes from the difference between fermions and bosons in equation (2.27). One can thus estimate the effective relativistic degree of freedom today as $g_{*s,0} \simeq 2 + 3\times\frac{7}{8}\times\frac{4}{11}\times2 \approx 3.9$, where the factor 2 comes from the degrees of freedom of a Dirac fermion and 3 is the number of neutrino flavours.

Cold dark matter

The freeze-out of CDM occurs while the particles are non-relativistic, implying that $Y_{\rm eq}$ decreases exponentially as equation (2.26). In this case, the main problem is to find the freeze-out time x_f. In the early radiation dominated era of the Universe, the two last terms of the Friedmann equation (2.14) can be neglected since $\rho \propto a^{-4}$ (eq. (2.28)), such that $H \simeq 1.66\sqrt{g_*}T^2/M_{\rm Pl}$, where $M_{\rm Pl}$ is the Planck mass. Assuming that $Y_\infty \approx Y(x_f)$ and that the annihilation cross section $\langle\sigma_{\rm ann}v\rangle = \sigma_0$ is constant, the Gamov criterion $H = \Gamma_{\rm ann,eq} = n_{\rm eq}\langle\sigma_{\rm ann}v\rangle$ yields

$$x_f^{-1/2}{\rm e}^{x_f} = 0.038\frac{g}{\sqrt{g_*}}M_{\rm Pl}m\sigma_0 \equiv C. \tag{2.37}$$

We will consider a Majorana fermion as DM candidate with $g = 2$. At large temperatures, most of the particle species are relativistic and $g_* \sim 10^2$.[8] Solving equation (2.37) numerically for $\langle\sigma_{\rm ann}v\rangle = 3\times10^{-26}\,{\rm cm^3/s}$ and $m = \{10, 10^2, 10^3\}\,{\rm GeV}$ yields $x_f \approx \{23, 26, 29\}$. In other words, the freeze-out temperature changes slowly for the relevant DM masses with a typical value $x_f = 30$. Using now equation (2.30) and the constant entropy, one finds

$$\frac{n(x_f)}{n_0} = \left(\frac{a(x_f)}{a_0}\right)^3 = \frac{g_{*s,0}T_0^3}{g_{*s,f}T_f^3}, \tag{2.38}$$

where a subscript ‘0’ refers to the quantities in the present Universe. In turn, with $g_{*s,0} \approx 3.9$, $g_{*s,f} \sim g_{*,f} \sim 100$ and $T_0 = 2.73\,{\rm K}$, we obtain

$$\Omega_c h^2 = \frac{mn_0}{\rho_{\rm cr}} \sim \frac{10^{-28}\,{\rm cm^3/s}}{\sigma_0}x_f. \tag{2.39}$$

Thus, in order to reproduce the observed relic density $\Omega_c h^2 \approx 0.1$ indicated by the CMB, one must choose $\sigma_0 \approx 3\times10^{-26}\,{\rm cm^3/s}$, which is the canonical value often cited in the literature. This cross section is typical for weakly interacting and massive particles. As such, these types of CDM particles are named WIMPs. The coincidence between $\langle\sigma_{\rm ann}v\rangle$ and a typical weak scale interaction cross section in the SM is known as the *WIMP miracle*. An upper limit $m \lesssim 100\,{\rm TeV}$ can be set using partial wave unitarity [26, 27].

Finally, we note that $\langle\sigma_{\rm ann}v\rangle$ is highly model dependent. In the above, we assumed that $\langle\sigma_{\rm ann}v\rangle = \sigma_{\rm ann}^{(s)} + \sigma_{\rm ann}^{(l)}\langle v\rangle^2 + ...$, including only the s-wave contribution. This is not always the case, and the cross section may in some circumstances vary orders of magnitude due to effects like Sommerfeld enhancement [28]. Furthermore, in the calculations above, we assumed that a single DM particle reproduced the entire relic density. However, it is in general possible to have more than one DM candidate. Other DM particles have in general different production mechanisms.

---

[8] However, the solution is to a good approximation logarithmic, $x_f \approx \ln C$, so the main conclusion remains unchanged for most choices.

2.4 Dark matter candidates

There are clearly strong evidences for the existence of DM, but it is currently unknown what it consists of. As seen in section 2.3.3, non-baryonic DM has a relic density $\Omega_c h^2 \approx 0.1$ that cannot be explained by the SM. In this section we will therefore discuss a few non-baryonic DM candidates, including the WIMPs already introduced.

Candidates for non-baryonic DM must satisfy three conditions. Firstly, they must be stable on cosmological time scales in order to not have decayed by now. Secondly, they must interact weakly with electromagnetic radiation in order to be considered as dark. Lastly, they must have the correct relic density. Possible candidates for non-baryonic DM includes axions, primordial black holes, sterile neutrinos and WIMPs. In addition, there exist some alternative theories which evades the introduction of DM in the first place. Each of these will now be discussed briefly.

Axions and the strong CP problem

Axions were first postulated as a solution to the strong CP problem in the SM. The following is based on the discussions in Refs. [14, 18, 22]. The quantum chromodynamics (QCD) Lagrangian includes a CP violating term $\mathcal{L}_\theta = -\bar{\theta}(\alpha_s/8\pi)\,\mathrm{tr}\Big\{F^{\mu\nu}\tilde{F}_{\mu\nu}\Big\}$, where $\bar{\theta} \in [0, 2\pi]$ is a free parameter and $F^{\mu\nu a}$ is the colour field strength tensor. Note that we have neglected this term in the discussion of QCD in section 3.1 as it is a four-divergence and does not contribute to perturbation theory. However, this term has non-perturbative effects associated with the instanton solution to the Yang-Mills equations and the axial anomaly in a Yang-Mills theory coupled to massive quarks. Remarkably, measured limits on the neutron electric dipole moment have limited the CP violation parameter to $|\bar{\theta}| \lesssim 10^{-10}$, even though it would be otherwise perfectly fine to have $|\bar{\theta}| = \mathcal{O}(1)$. This fine-tuning problem is known as the strong CP problem. One possible solution is to introduce the spontaneously broken Peccei-Quinn $U(1)_{\mathrm{PQ}}$ quasi-symmetry, which must be a symmetry at the classical level and broken by the non-perturbative effects associated with $\bar{\theta}$. The quasi-Goldstone boson associated with the spontaneously broken symmetry is the axion. Due to the arbitrariness of this field, the parameter $\bar{\theta}$ is allowed to relax to zero, thus solving the strong CP problem. The axions as DM candidates are generally very light ($\sim 0.1\,\mathrm{meV}$) but can still contribute to the CDM abundance as they are produced non-thermally.

Primordial black holes

There is currently little knowledge about DM beside its gravitational effects and that it is dynamically “cold”. It is thus possible that the DM abundance does not consist of ordinary elementary particles. In fact, it is conceivable, in some contrived cosmological models that the DM abundance consists of a large quantity of black holes that are too massive to have evaporated by now [29]. These are known as primordial black holes, and must have formed before the Big Bang nucleosynthesis when the baryons only constituted a small part of the total energy density, in order to contribute to the non-baryonic DM density. The interest for primordial black holes was revived after the recent detection of gravitational waves by LIGO in 2016 [30]. However, astrophysical observations constrain the possible masses of the black holes to, at best, a few narrow mass windows [31]. In any case, it is possible that primordial black holes constitute only a minor part of the DM abundance.

Sterile Neutrinos

In the SM, the neutrino masses were traditionally set to zero. Today, however, it an experimental fact that the neutrinos have small non-zero masses. The neutrinos can be given mass by adding a term from a higher dimensional operator suppressed by some unknown scale to the Lagrangian. However, this makes the Lagrangian non-renormalisable. Furthermore, under the SM gauge group $\mathrm{SU}(3)_\mathrm{c} \times \mathrm{SU}(2)_\mathrm{L} \times \mathrm{U}(1)_\mathrm{Y}$, there is a clear mismatch between the quark and lepton degrees of freedom: there exists only left-handed neutrinos. These properties may indicate new unseen particles and unobserved physics.

The fermion masses of the active neutrinos in the SM can be generated by introducing singlet Majorana fermions to the SM [18].[9] That is, we introduce new right handed neutrinos that only interact with the SM particles through a weak mixing with the SM neutrinos if the SM neutrinos are Dirac fermions. The number of new neutrinos cannot be deduced from symmetries, but is usually taken to be equal to the number of lepton and quark generations. These are known as sterile singlet neutrinos and is a possible DM candidate. Depending on the implementation of the sterile neutrinos, their masses can range from $M = 0$ to $M \lesssim 10^9\,\mathrm{GeV}$ [32]. However, due to the stability of the DM particles, small masses and mixing angles are favoured.

Weakly interacting massive particles

WIMPs are, as the name suggests, a class massive hypothetical particles that has a cross section around the weak scale. As was discussed in section 2.3.4, $\langle\sigma_\mathrm{ann} v\rangle \sim 3\times10^{-26}\,\mathrm{cm}^3/\mathrm{s}$ reproduces the correct relic density. Here we will discuss some possible WIMP candidates.

The SM of particle physics is by itself a complete quantum field theory that is able to explain a variety of phenomena spanning over many orders of magnitude. As we have seen, there are by now several experimental evidences that suggest the existence of physics beyond the SM. This includes the existence of DM and dark energy, the strong CP problem, “the hierarchy problem”, the non-zero neutrino masses and the baryon

---

[9] One may instead add no fermionic degrees of freedom, but this requires a Higgs triplet with weak hypercharge 2.

asymmetry. Thus, the SM should be viewed as an effective theory. Super symmetric extensions to the SM are attractive as models beyond the SM as they attempt to address the aforementioned observations, and at the same time addresses questions related to e.g. grand unified theories. Supersymmetry (SUSY) is a generalisation of the space-time symmetries of quantum field theory (QFT) and predicts that fermions may transform into bosons, and bosons into fermions [14]. In other words, all fermions have a bosonic counterpart, and vice versa. Many SUSY theories includes one or more charge neural and stable particles that interacts only weakly with ordinary matter, thereby providing a suitable DM candidate.

The lightest SUSY particle provides often a simple DM candidate [18]. For example, in the Minimal Supersymmetric Standard Model, the four fermions corresponding to the electroweak gauge bosons and the Higgs boson are known as neutralinos (see Refs. [14, 18] for a short introduction). In this model, a $B - L$ symmetry is imposed on the Lagrangian, which leads to what is known as R-parity invariance. A particle with spin s has $R = (-1)^{3(B-L)+2s}$. Thus, all SM particles have even R-parity, while their SUSY partners has an odd R-parity. This implies that the lightest SUSY particle is stable, and cosmological constraints indicates that it should be electrically and colour neutral. A neutralino as the lightest SUSY particle is the leading WIMP candidate. Due to the free parameters of the model, it is possible to generate particles within a large mass and interaction cross section ranges. This is why we in chapter 6 will assume that the DM candidate is a weakly interacting Majorana fermion with a given set of masses, without any references to specific models.

Alternative theories

Some alternative theories to DM exists, perhaps the most popular and simplest alternative is the so-called modified Newtonian dynamics (MOND) paradigm, postulated by Milgrom in 1983. Here we will review the basic assumptions and principles of the theory. More comprehensive reviews can be found in Refs. [18, 33].

All of the arguments we have considered that are related to the existence of DM relies on Newtonian or Einsteinian gravitation. It is thus important to ask if it is possible to evade the introduction of DM in the first place by modifying the laws of gravitation. The current laws of gravitation are well tested and describe well all observed systems up to the scale of globular clusters. However, problem arises when trying to describe the motion on galactic and intergalactic scales based on the observed matter. One natural solution is to assume that our current understanding of gravity is flawed in the weak field limit. The simplest solution is to assume that the acceleration $\boldsymbol{a}$ of a test particle due to a gravitational potential Φ_N is given by

$$\mu\left(\frac{|\boldsymbol{a}|}{a_0}\right)\boldsymbol{a} = -\nabla\Phi_\mathrm{N}, \tag{2.40}$$

where $\mu(x)$ is a suitable interpolating function and $a_0 \sim 10^{-8}\,\mathrm{cm/s^2}$ is a typical acceleration scale at which MOND becomes important. Milgrom postulated that $\mu(x \ll 1) = x$. Furthermore, one must require that $\mu(x \gg 1) = 1$ in order to obtain the standard Newtonian dynamics. One common choice is $\mu(x) = x/\sqrt{1+x^2}$.

As an example, consider the constant rotation curves discussed in section 2.1.1. As before, we start by noting that visible matter in a spiral galaxy follows approximately circular orbits with velocity $v(r)$, for which $|\boldsymbol{a}| = v^2(r)/r$. Thus, at sufficiently large r, $\mu(|\boldsymbol{a}|/a_0 \ll 1) = |\boldsymbol{a}|/a_0$. On the other hand, the gravitational force can be approximated as $|\nabla\Phi_\mathrm{N}| \approx GM/r^2$ at large r. Inserting everything into equation (2.40) yields

$$v = \sqrt[4]{GMa_0}. \tag{2.41}$$

That is, at large r the rotation curve stays constant.

Note that equation (2.40) can be interpreted as reflecting modified inertia. That is, it can be viewed as a modification of Newton's second law, $\boldsymbol{f} = m\boldsymbol{a}$. In this picture, however, MOND violates momentum conservation and should thus not be considered as exact.[10] Nevertheless, by choosing a suitable classical Lagrangian, momentum and energy can be conserved by construction.

The MOND theories describes well a large number of observations on galactic scales, but there are a few problems. First, the discussions above are non-relativistic and existing attempts at embedding the same considerations into a relativistic theory requires the introduction of additional degrees of freedom, such as additional fields. This introduces an increased arbitrariness to the model. Second, the description of large scale structure formations requires the existence of some additional matter in these theories as well. Third, instances like the Bullet Cluster discussed in section 2.2.2 are hard to explain using modified gravity where the gravitational lensing must follow the baryonic matter.

2.5 WIMP detection

Current evidences for DM all rely on its gravitational effect, but its nature is yet to be determined. Here we will discuss different detection methods for WIMPs, but they are in principle applicable to most particle DM. There are three different detection methods: indirect detection, direct detection and collider searches. Current constraints and detection principles are reviewed in Refs. [14, 18].

Direct detection

Assuming that the dark halo consists of WIMPs, there will at any given moment be a WIMP flux through Earth. From figure 2.1, one knows that the velocity of the

---

[10] In a two-body system with unequal masses m_1 and m_2, the quantity $m_1v_1 + m_2v_2$ does not vanish as required by momentum conservation since $\mu(a_2/a_0) \neq \mu(a_1/a_0)$.

Sun around the Galactic centre is about $v_\odot \sim 2 \times 10^5\,\mathrm{m/s}$. With a local DM density $\rho_\odot = 0.30\,\mathrm{GeV/cm^3}$, one finds that the flux through Earth is on the order of $10^5(100\,\mathrm{GeV}/m_\chi)\,\mathrm{cm^{-2}s^{-1}}$. Thus, there is a chance for a detectable elastic collision rate between the WIMPs and SM particles on Earth. This is the main principle utilised in direct detection experiments.

In direct DM detection methods one aims at detecting nuclear recoils caused by WIMPs. The differential interaction rate R between a WIMP with mass m_χ and a nucleus with mass m_N can be expressed as

$$\frac{\mathrm{d}R}{\mathrm{d}E_R} = \frac{\rho_\odot}{m_N m_\chi} \int_0^\infty v f(v) \frac{\mathrm{d}\sigma_{\chi N}}{\mathrm{d}E_R}\,\mathrm{d}v\,, \tag{2.42}$$

where E_R is the recoil energy, v is the speed of the WIMP in the detector frame, $f(v)$ is the WIMP speed distribution in the detector frame and $\mathrm{d}\sigma_{\chi N}(v, E_R)/\mathrm{d}E_R$ is the WIMP-nucleus differential cross section. The integration limits are usually taken to be between the detector limit, v_{min}, and the Galaxy escape velocity, v_{esc}. The speed distribution $f(v)$ is usually assumed to be Maxwellian, $f(\boldsymbol{v}) = \exp\{-v^2/(2\sigma^2\}/\sqrt{2\pi}\sigma$. All of the particle physics inputs are encoded into the differential cross section, and must be determined by the microphysics in a specific WIMP model. Note that the large uncertainty in $\rho_\odot$ directly translates to an uncertainty in the rate. In any case, the velocity of the Earth relative to the dark halo depends on the rotation of the Earth and the motion of the Earth about the Sun. This may yield a characteristic time dependence on the interaction rate that is independent of the uncertainties. The lack of detection of WIMPs has lead to strong constraints on the WIMP-nucleus cross section, but is not particularly constraining for the general WIMP class.

Indirect detection

The detection of secondary particles from DM annihilations or decays in the Galaxy may offer a potential means of identifying the nature of DM. The secondary particle spectra must have a distinct signature in order to be a suitable for indirect DM detection. Here we will mention three possibilities: neutrinos, photons and antimatter.

The main advantage of using photons and neutrinos in DM searches is that they propagate in straight lines, making it possible to retrace the source. DM may be captured in celestial bodies, such as the Sun and dwarf galaxies when they travel through the dark halo. This leads to an increased DM density with an increased annihilation rate. In particular, WIMP annihilations in the Sun produces neutrinos which may leave the Sun with minimal absorption. Recent developments in neutrino detectors, such as IceCube, have made these a promising detection channel.

As the DM particles cannot interact directly with photons, photons will mainly be produced in a continuum energy spectrum created by mesons in the quark fragmentation for

SM final states. Nevertheless, some higher order electroweak corrections may have some interesting and characteristic properties. In the case of gamma-radiation, the "smoking gun" process $\chi\bar{\chi} \to 2\gamma$ offers a potential method of determining the DM mass, since the two photons will be emitted back to back with an energy $E_\gamma = m_\chi$. Thus, one would measure a characteristic peak at these energies, broadened slightly by a small Doppler shift. The process $\chi\bar{\chi} \to \gamma Z$ can be used in the same manner. These processes occurs at one-loop and are thus typically suppressed by a factor $(\alpha/\pi)^2$, except in a few special cases such as Sommerfeld enhancement (See Ref. [28] for a short review and references). Another higher order effect is the possibility of internal Bremstrahlung photons for fermion final states, which is only suppressed by a factor α/π.[11]

One of the main difficulties in using neutrinos and photons in indirect DM searches is the enormous amount of both extragalactic and intergalactic background noise. The use of charged antiparticles, such as positrons, antiprotons and light antinuclei, avoids this problem due to the baryon asymmetry in the Universe. On the other hand, they are affected by turbulent magnetic fields in the Galaxy making the source untraceable. In chapter 6 we will study this for light antinuclei, and the process of deriving the expected flux on Earth is quite similar for the other antiparticle species.

Presently, the search for antiproton and antinuclei is performed by the AMS-02 experiment on board of the International Space Station, while the GAPS balloon experiment is expected to fly during the next solar minimum in late 2020 or 2021 [2, 3]. The AMS-02 experiment launched in 2011 and is expected to be in operation until 2024. Previously, the PAMELA experiment was collecting data for ten years from 2006 to 2016 [34]. The current best measurements on intergalactic antimatter flux comes from the PAMELA experiment and the AMS-02 experiment. No indubitable DM signals have yet been found, as the measured antiproton and positron data are well described by secondary sources. That is, they are produced by (mainly) proton and helium colliding with the helium and hydrogen in the interstellar matter (ISM). However, there was a significant excess detected around $T \sim 10$–$300\,\mathrm{GeV}$ in the PAMELA positron data that was later confirmed by AMS-02 [35]. This suggests a new astrophysical primary source, such as possible pulsars or supernova remnants, or unknown contributions to the secondary propagation. A more intriguing possibility is DM annihilations or decays. Unfortunately, this excess is not present in the antiproton data, putting strong constraints on the possible DM candidates responsible for the positron excess [36]. Recently, AMS-02 reported antiproton data that exhibits a small excess around $\sim 100\,\mathrm{GeV}$ [37]. This is consistent with a DM signal with a mass $\sim 80\,\mathrm{GeV}$ and an annihilation cross section near $\langle\sigma_{\mathrm{ann}}v\rangle \approx 3 \times 10^{-26}\,\mathrm{cm}^3/\mathrm{s}$ [38]. Interestingly, this is also compatible with a DM interpretation of a gamma-ray excess from the Galactic centre [38]. It should be noted that these processes includes large sources of uncertainties related to propagation, as will be discussed for light nuclei in chapter 6. The antimatter

---

[11] For example, a Majorana fermion annihilating into fermion final states suffers a helicity suppression for an s-wave ($L = 0$) annihilation, which is avoided when a photon is added to one internal leg.

data currently put constraints on DM masses $\lesssim 50\,\mathrm{GeV}$ [38, 39], such as the possible contributions to different annihilation channels.

Antideuteron and antihelium nuclei have been proposed as a detection channel for dark matter annihilations and decays in the Milky Way, due to the low expected astrophysical background. The dominant background source of antideuterons are cosmic ray protons interacting with the interstellar medium. The high threshold energy for this reaction channel ($\sim 17 m_p$) implies that the antideuterons produced by cosmic rays have relatively large kinetic energies. This makes them ideal as a detection channel at low energies. The suppression is even larger for helium-3 ($\sim 31 m_p$). Presently, no antideuteron events have been reported. However, AMS-02 has reported the detection of six possible antihelium-3 events in the momentum range $< 100\,\mathrm{GeV}$, and even two possible antihelium-4 events [4].[12] There have been a number of different attempts to explain this phenomenon, such as DM [40] or even antimatter dominated regions of space [41]. As will be shown in chapter 4, the production of helium-3 should be highly suppressed compared to antideuterons. Thus, they are hard to explain without the presence of antideuteron events. We will come back to this in chapter 6.

Collider searches

The DM particles can be detected in a collider experiment in two ways: directly via missing transverse momenta, or indirectly via virtual exchange of beyond the SM particles. The main method is through missing transverse momenta: once produced it will leave the detector without being detected.

Since the DM particle interacts only weakly with SM particles, the best hope may be to detect an unstable particle that is a part of a more comprehensive particle zoo including the DM particle. However, there is not yet any evidence for weak-scale SUSY from analysed data from the Large Hadron Collider (LHC) [14].

The main advantage in collider searches is that they do not suffer from astrophysical uncertainties. On the other hand, a collider can only hope to detect DM masses up to a given threshold determined by the collision energies. In addition, one cannot know whether the detected particle in fact constitutes the astrophysical DM.

---

[12] Note, however, that the AMS-02 collaboration has not yet any publications on the subject.

3 QCD and collider physics

The aim of this chapter is to describe processes like $e^+e^- \to \bar{q}q \to$ hadrons. These processes will ultimately be considered using pre-existing Monte Carlo (MC) event generators. Nevertheless, it is instructive and important to understand the basic principles utilised in order to, amongst other, discuss limitations and configure the programs correctly. The process can be split into three parts. The first part consist of using standard perturbation theory on the process $e^+e^- \to \bar{q}q$ known from perturbative QFT. The QCD Lagrangian and the corresponding Feynman rules are described in section 3.1. Next, a parton shower starts, in which a number of quarks and gluons are created in a QCD Bremsstrahlung process. This is described in sections 3.4.1 and 3.4.2. Finally, due to the properties of confinement and asymptotic freedom, discussed in 3.3, one must add a hadronisation scheme to describe the production of hadrons from the sea of partons. This is discussed in section 3.4.3. In addition, section 3.2 discusses approximate symmetries of light quarks which will turn out to be important in the next chapter. Most of the content of this chapter is obtained from Refs. [42, 43].

3.1 QCD Lagrangian

QCD is the theory that describes the strong interaction between quarks. It is described mathematically by a non-Abelian SU(3) theory of colour charge with a classical Lagrangian

$$\mathcal{L}_{\text{QCD}} = -\frac{1}{4}F^A_{\mu\nu}F^{A\mu\nu} + \sum_{\text{flavour}} \bar{q}_a(\mathrm{i}\gamma^\mu D_\mu - m)_{ab}q_b, \tag{3.1}$$

where the sum goes over the n_f different quark flavours and the spinor indices (i, j, k) of γ_μ and q_a have been suppressed. The field strength tensor and the covariant derivative are given by

$$F^A_{\mu\nu} = \partial_\mu A^A_\nu - \partial_\nu A^A_\mu - g_s f^{ABC} A^B_\mu A^C_\nu \quad \text{and} \quad D_{\mu ij} = \delta_{ij}\partial_\mu + \mathrm{i}g_s T^A_{ij} A^A_\mu, \tag{3.2}$$

respectively. Here A^A_μ are the gluon fields, g_s is the gauge coupling, and f^{ABC} is the structure constant of the SU(3) symmetry. The latter is defined through the commutator relation between the generators T^A as $[T^A, T^B] = \mathrm{i}f^{ABC}T^C$. The capital Latin indices run over the eight colour degrees of freedom, while the quarks are in the triplet representation of the colour charge $(a = 1, 2, 3)$. The indices can be interpreted as if the quarks carry one colour charge (‘red’, ‘green’ or ‘blue’) each and the antiquarks carry corresponding anticolour charge. Meanwhile, the gluons carry one colour and one anticolour, separated into a colour singlet and a colour octet. The colour octet corresponds to the eight generators of SU(3), while the singlet state gluon does not exist.[1] The quarks live in the fundamental representation of SU(3) with generators t^A. One choice of representation is to use $t^A = \lambda^A/2$, where λ^A are the Gell-Mann matrices. The gluons lives in the adjoint representation $(T^A)^{BC} = -if^{ABC}$.

The Lagrangian (3.1) is invariant under the SU(3) gauge symmetry

$$q \to q = \exp\Big\{ig\theta^A T^A\Big\}q \tag{3.3}$$

and leads to the vertices and propagators shown in figure 3.1. Note that quarks, as charged leptons, also couple to the photon and the Z boson in the SM. Moreover, the Higgs mechanism in the electroweak theory will give mass to the quarks. However, the Higgs effect only accounts for a small fraction of the total mass of the hadrons, but this will not be discussed here. The SU(3) symmetry implies that no colour are physically preferred.

By convention, the normalisation $\mathrm{tr}\Big\{t^A t^B\Big\} = T_R \delta^{AB}$ with $T_R = 1/2$, is used. Two important immediate consequences of an SU(N) symmetry and the chosen normalisation are

$$\sum_A t^A_{ab} t^A_{bc} = \frac{N^2-1}{2N}\delta_{ab} \equiv C_F \delta_{ik}, \tag{3.4a}$$

$$\mathrm{tr}\Big\{T^C T^D\Big\} = \sum_{A,B} f^{ABC} f^{ABD} = N C_A \delta^{CD} \equiv C_A \delta^{CD}, \tag{3.4b}$$

where t^A and T^A are the generators for the fundamental and adjoint representation, respectively. In the case of SU(3), we have $C_F = 4/3$ and $C_A = 3$.

3.2 Light quark symmetries

There are several symmetries associated with the QCD Lagrangian. This includes the imposed local gauge invariance that is responsible for renormalisability, as well as charge conjugation, parity and time reversal invariance in agreement with experiments. In addition there are some approximate symmetries, such as isospin, that are related to the quark generations and masses. These are important as they provide simple relations even when perturbation theory is not applicable.

The two lightest quarks, the up quark with mass $m_u \simeq 2.3\,\mathrm{MeV}$ and down quark with mass $m_d \simeq 4.8\,\mathrm{MeV}$, are much lighter than the charm ($m_c \simeq 1.3\,\mathrm{GeV}$), strange

---

[1] The colour-singlet would interact with colourless states, but no long-range gluon interactions with hadrons, which are colourless, have not been observed.

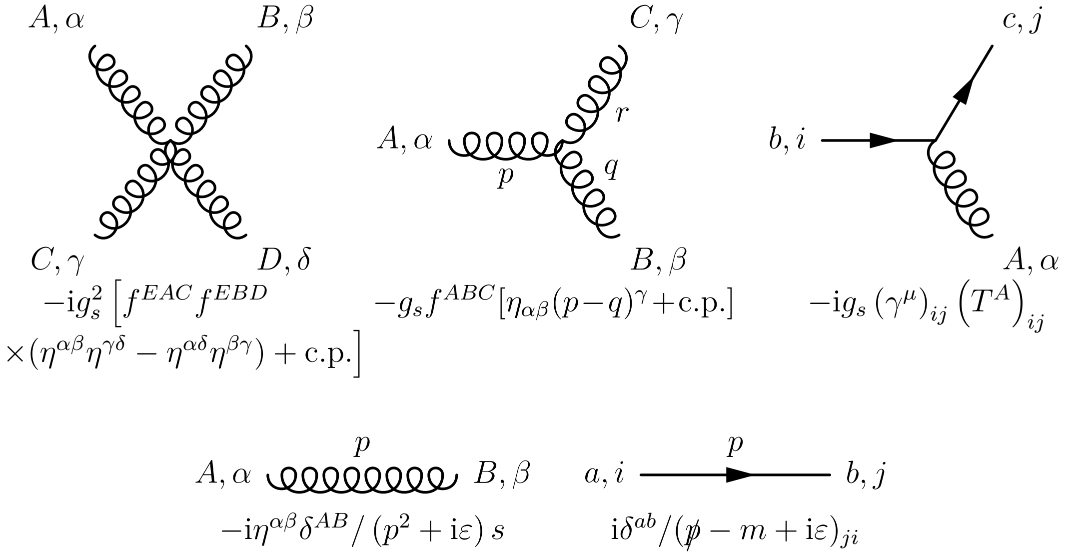

Figure 3.1: Feynman rules for QCD in the Feynman gauge for gluons (curly lines) and quarks (solid lines). The abbreviation c.p. refers to circular permutations of the indices of the external legs.

($m_s \simeq 95\,\mathrm{MeV}$), top ($m_t \simeq 173\,\mathrm{GeV}$) and bottom ($m_b \simeq 4.2\,\mathrm{GeV}$) quarks. As we will see shortly, this leads to an approximate invariance. In the limit of equal light quark masses, $m_u = m_d \equiv m_q$, the part of the Lagrangian (3.1) including the u and d fields can be written as

$$\mathcal{L}_q = \bar{q}(\mathrm{i}\gamma^\mu D_\mu + M)q, \tag{3.5}$$

where we introduced the notation $q = (u\ d)^\mathrm{T}$ for the quark fields and $M_{ij} = m_q\delta_{ij}$ is the mass matrix. This Lagrangian is invariant under $\mathrm{U}(2) = \mathrm{U}(1) \otimes \mathrm{SU}(2)$ symmetry, where $\mathrm{U}(1)_V$ is the quark number symmetry originally present, while the $\mathrm{SU}(2)_V$ symmetry is the isospin symmetry. In analogy to spin $\boldsymbol{S}$, the quarks can be assigned an isospin $\boldsymbol{I}$, which is a vector in an abstract isospin space. The up and down quarks are described as two isospin states of the same particle by the ket vectors $u = |1/2, 1/2\rangle$ and $d = |1/2, -1/2\rangle$. All other particles are assigned isospin zero for consistency.

The proton consists of two up-quarks and one down-quark, while the neutron consists of one up-quark and two down-quarks. Naturally, the approximate isospin symmetry implies that the proton and neutron can to a good approximation be regarded as two states of a single particle called the nucleon. Historically, this was proposed by Heisenberg after the discovery of the neutron in 1932 [44]. He observed that the neutron was nearly identical to the proton apart from the charge: the neutron mass $m_n = 939.57\,\mathrm{MeV}$ is astoundingly close to the proton mass $m_p = 938.27\,\mathrm{MeV}$. As before, the proton and neutron can be described by the ket vectors $|1/2, 1/2\rangle$ and $|1/2, -1/2\rangle$, respectively. Note again that isospin is, opposed to spin, by no means an exact symmetry, but it describes well that the neutron and proton are nearly indistinguishable by the strong force.

Approximate symmetries are the origin of many of the characteristics one observes in mesons and baryons. In the limit of massless up and down quarks, the approximate isospin symmetry becomes even larger: a chiral SU(2) symmetry. However, this symmetry is spontaneously broken into the $\mathrm{SU}(2)\times\mathrm{U}(1)_V$ symmetry discussed above. The associated Goldstone bosons are identified as the three pions $\pi^{\pm}$ and π^0. Since this is only an approximate symmetry, these are not massless as one would expect from a broken symmetry, but are in fact much lighter than the other hadrons. In the same manner, the approximate SU(3) symmetry of the up, down and strange quark leads to the octet and decuplet flavour classification of the mesons and baryons, respectively. As before, in the limit when these are massless, one obtains an SU(3) chiral symmetry that is spontaneously broken. The associated Goldstone bosons corresponds to the octet $\pi^{\pm}, \pi^0, K^{\pm}, K^0, \bar{K}^0$ and η, which incidentally are the lightest hadrons. For heavier quarks, there are other approximate symmetries that can be exploited, but this will not be discussed here.

3.3 Asymptotic freedom and the QCD scale

A quite distinct feature in QCD is known as asymptotic freedom. This describes how the strong coupling constant decreases as the four momentum transfer Q increases. Thus, quarks and gluons behaves as free particles at large energies, while they are confined as hadrons at low energies, meaning that for sufficiently large momentum transfers, one can perform ordinary perturbation theory. The running coupling is determined by the renormalisation group equation

$$\mu^2 \frac{\partial \alpha_s}{\partial \mu^2} = \beta(\alpha_S) = -b_0\alpha_s^2 - b_1\alpha_s^3 - b_2\alpha_s^4 + \cdots , \tag{3.6}$$

where $\alpha_s = g_S^2/4\pi$ is the strong coupling constant and μ is the renormalisation scale. It can be noted that the coefficients $b_2, b_3, ...$ are dependent on the renormalisation scheme. For simplicity, we will only consider the one-loop β-function coefficient given by $b_0 = (11C_A - 2n_f)/12\pi = (33 - 2n_f)/12\pi$, where n_f is the number of active quark flavours. In the SM, $n_f \leq 6$ meaning that $b_0 > 0$. Integrating equation (3.6) at one-loop from μ_0 to Q yields

$$\alpha_s(Q^2) = \frac{\alpha_s(\mu_0^2)}{1 + \alpha_s(\mu_0^2) b_0 \ln(Q^2/\mu_0^2)}. \tag{3.7}$$

Evidently, α_s decreases for increasing Q^2/μ_0^2.

In an alternative approach, a dimensionful parameter can be introduced directly into the definition of the coupling constant α_s. This parameter, denoted as Λ_{QCD}, is defined via the integral

$$\ln \frac{Q^2}{\Lambda_{\mathrm{QCD}}^2} = -\int_{\alpha_s(Q^2)}^{\infty} \frac{\mathrm{d}x}{\beta(x)}, \tag{3.8}$$

That is, it is defined such that the coupling constant becomes strong close to $Q^2 = \mathcal{O}(\Lambda^2_{\mathrm{QCD}})$. The QCD scale has a numerical value $\Lambda_{\mathrm{QCD}} \sim 200\,\mathrm{MeV} \sim R_p^{-1}$ (R_p being the proton size), but the exact number depends on the chosen renormalisation scheme and must be determined by experiments. For example, in the $\overline{\mathrm{MS}}$-scheme with three quark flavours it is $\Lambda^{(3)}_{\overline{\mathrm{MS}}} \sim (332 \pm 17)\,\mathrm{MeV}$ and with six $\Lambda^{(6)}_{\overline{\mathrm{MS}}} \sim (89 \pm 6)\,\mathrm{MeV}$ [14]. At one-loop (3.8) yields

$$\alpha_s(Q^2) = \frac{1}{b \ln\left(Q^2/\Lambda^2_{\mathrm{QCD}}\right)}. \tag{3.9}$$

Since perturbation theory rely on the assumption $\alpha_s \ll 1$, one must require that $Q^2 \gg \Lambda^2_{\mathrm{QCD}}$ in order to use it. As we will see soon, the QCD scale is often used to represent the scale at which hadronisation must occur.

3.4 Monte Carlo event generators

Even before the development of QCD, it was noticed that the hadrons behave at large momentum transfer as if they consist of a number of point-like massless particles. These were called *partons*, and are today associated with the gluons and quarks. Due to asymptotic freedom and confinement, we know that quarks cannot propagate freely on macroscopical time and distance scales. Thus, after a process such as $e^+e^- \to \bar{q}q$, these free quarks must produce other quarks and gluons in order to be able to hadronise. In this section, we will first compute the amplitude for a parton branching before describing the evolution of a parton shower and hadronisation.

3.4.1 Parton branching

Consider a time-like branching of a parton a into a pair bc as shown in figure 3.2. Let $k_i^\mu = (E_i, \boldsymbol{k}_i)$ be the four-momentum of parton i and $t \equiv k_a^\mu k_{a\mu} \gg \{k_b^\mu k_{b\mu}, k_c^\mu k_{c\mu}\} > 0$ in the small angle approximation $\theta = \theta_b + \theta_c \ll 1$. Note that t is a measure of the virtuality of the particle. In branching, the virtuality will decrease until one has to stop at $t \sim \Lambda^2_{\mathrm{QCD}}$, where non-perturbative effects become important. In a space-like branching, on the other hand, the virtuality decreases from $-t$ until it reaches a chosen cut-off scale $-Q^2$. Let $z \equiv E_b/E_a = 1 - E_c/E_a$ be the energy fraction taken by parton b. The virtuality can then be written as

$$t = 2E_bE_c(1 - \cos\theta) \approx z(1-z)E_a^2\theta^2, \tag{3.10}$$

and thus, using conservation of transverse momentum ($\theta_b E_b = \theta_c E_c$), the opening angle can be written as

$$\theta = \frac{1}{E_a}\sqrt{\frac{t}{z(1-z)}} = \frac{\theta_b}{1-z} = \frac{\theta_c}{z}. \tag{3.11}$$

In order to continue, one has to fix the vertex type. As an example, we will consider the three gluon vertex V_{ggg}. By using the vertices introduced previously in figure 3.1, one finds

$$V_{ggg} = \mathrm{i} g f^{ABC} \varepsilon_a^\alpha \varepsilon_b^\beta \varepsilon_c^\gamma \left[\eta_{\alpha\beta}(k_a - k_b)_\gamma + \eta_{\beta\gamma}(k_b - k_c)_\alpha + \eta_{\gamma\alpha}(k_c - k_a)_\beta\right]. \tag{3.12}$$

The polarisation vectors can be fixed by assuming that the three gluons are approximately on the mass shell, $k_i^\mu k_{i\mu} \approx 0$, in which case the polarisation vectors can be chosen transverse to the momenta, $k_i^\mu \epsilon_{i\mu} = 0$. It is convenient to split them into a part parallel to the plane of branching (in the plane of figure 3.2), $\varepsilon_i^{\text{in}}$, and a part transverse to the plane of branching, $\varepsilon_i^{\text{out}}$.

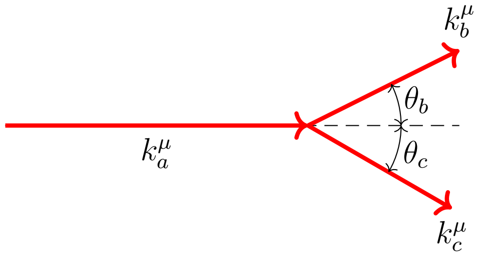

Figure 3.2: Setup for the branching of a parton in the plane of branching.

Assume that the amplitude after n splittings, $\mathcal{A}_n$, is known. The goal is to compute the amplitude after $n+1$ splittings. Using the gluon propagator $\propto 1/t$ between the graph contained in $\mathcal{A}_n$ and the $g \to gg$ branching, one finds

$$|\mathcal{A}_{n+1}|^2 = \left|\frac{V_{ggg}}{t}\mathcal{A}_n\right|^2 \approx \frac{4g^2}{t} C_A F(a,b,c;z)|\mathcal{A}_n|^2, \tag{3.13}$$

where $C_A = 3$ was defined in equation (3.4b) and the non-zero and allowed combinations of polarisation vectors in the function $F(\varepsilon_a, \varepsilon_b, \varepsilon_c; z)$ are

$$F(\varepsilon_a^{\text{in}}, \varepsilon_b^{\text{in}}, \varepsilon_c^{\text{in}}; z) = \frac{1-z}{z} + \frac{z}{1-z} + z(1-z) \tag{3.14a}$$

$$F(\varepsilon_a^{\text{in}}, \varepsilon_b^{\text{out}}, \varepsilon_c^{\text{out}}; z) = z(1-z) \tag{3.14b}$$

$$F(\varepsilon_a^{\text{in}}, \varepsilon_b^{\text{in}}, \varepsilon_c^{\text{out}}; z) = \frac{1-z}{z} \tag{3.14c}$$

$$F(\varepsilon_a^{\text{out}}, \varepsilon_b^{\text{out}}, \varepsilon_c^{\text{in}}; z) = \frac{z}{1-z}, \tag{3.14d}$$

where the θ-dependences have been written in terms of z using equation (3.11). Note that the contribution to the total amplitude near the poles at $z = 0$ (particle b is soft) and $z = 1$ (particle c is soft) is always associated with the emission of a gluon with a polarisation in the plane of branching. The amplitude will thus dependent on the angle ϕ between the polarisation ε_a and the plane. However, this contribution may be neglected as it is small and fades out after several splittings. Averaging $C_A F(z)$ over the polarisations yields the unpolarised splitting function

$$P_{gg}(z) = C_A \frac{1}{2} \sum_{\varepsilon_a} \sum_{\varepsilon_b, \varepsilon_c} F(\varepsilon_a, \varepsilon_b, \varepsilon_c; z) = C_A \left[\frac{1-z}{z} + \frac{z}{1-z} + z(1-z) \right] . \tag{3.15}$$

The unregularised splitting functions for the processes $g \to q\bar{q}$ and $g \to gq$ can be derived in the same manner as above. The results are

$$P_{qg}(z) = \left[z^2 + (1-z)^2 \right] \quad \text{and} \quad P_{gq}(z) = C_F \frac{1+z^2}{1-z} , \tag{3.16}$$

where $C_F = 4/3$ and $T_R = 1/2$.

The final-state with n partons has a phase space $\mathrm{d}\Phi_n \propto \mathrm{d}^3 k_a // ((2\pi)^3 2E_a)$ and should after the branching be replaced by the phase space $\mathrm{d}\Phi_{n+1} \propto \mathrm{d}^3 k_b / ((2\pi)^3 2E_b) \times \mathrm{d}^3 k_c // ((2\pi)^3 2E_c)$. Since $k_c = k_a - k_b$ and $\mathrm{d}^3 k_c = \mathrm{d}^3 k_a$ for fixed $\boldsymbol{k}_b$, we obtain in the small angle approximation, after the change of variables $\{E_c, \theta_c\} \to \{z, t\}$,

$$\mathrm{d}\Phi_{n+1} = \mathrm{d}\Phi_n \, \frac{1}{4(2\pi)^3} \, \mathrm{d}t \, \mathrm{d}z \, \mathrm{d}\phi \, . \tag{3.17}$$

The cross section is given by $\mathrm{d}\sigma_n \propto |\mathcal{A}_n|^2 \, \mathrm{d}\Phi_n$. Thus, performing the ϕ-integral yields

$$\frac{\mathrm{d}\sigma_{n+1}}{\mathrm{d}\sigma_n} = \frac{\mathrm{d}t}{t} \, \mathrm{d}z \, \frac{\alpha_s}{2\pi} P_{i \to j} . \tag{3.18}$$

This equation describes the probability density for an emission of an additional parton with virtuality t and fractional energy z. In the considerations above, it was assumed that the process was time-like, but the same results are obtained for a space-like process.

3.4.2 Evolution equation and Monte Carlo schemes

Consider now the effect of multiple branchings. The goal is to determine an equation that describes how the number density $f_i(x, t)$ of partons of type i with a given energy fraction x changes by the parton branching from t to $t + \delta t$. In a space-like process ($t_{n+1} > t_n$ and $x_{n+1} < x_n$), the quantity $f_i(x, t)$ represents the parton momentum distribution inside the hadron probed by, for example, a photon at a scale $q^2 = -Q^2$. In a time-like process ($t_{n+1} < t_n$ and $x_{n+1} > x_n$), $f_i(x, t)$ represents the momentum distribution of produced partons. The time-like process can, after the addition of a hadronisation model, be used to study a process like $e^+e^- \to$ hadrons, or even the production of hadrons from DM annihilations.

For concreteness, consider a space-like evolution of a single type of branching, such as multiple gluon emission from a space-like quark inside a hadron. At each branching, the quark emits a virtual gluon, which eventually decreases its virtuality from $-t_0$ to a chosen scale $-Q^2$. The change δf is given by the difference in the number of (x,t)-paths entering and leaving the element $(\delta x, \delta t)$ divided by δx, as indicated in figure 3.3. The number of paths entering the element is found by integrating the branching probability (3.18) multiplied by the parton density over all higher energy fractions $x' = x/z$. This yields

$$\delta f_{\mathrm{in}}(x,t) = \frac{\delta t}{t}\int_x^1 \mathrm{d}x'\,\mathrm{d}z\,\frac{\alpha_s}{2\pi}P(z)f(x',t)\delta(x-zx') = \frac{\delta t}{t}\int_0^1 \frac{\mathrm{d}z}{z}\frac{\alpha_s}{2\pi}P(z)f(x/z,t), \tag{3.19}$$

where the lower limit of the z integration could be extended from x to 0 since $f(x/z) = 0$ for $z < x$. The number leaving the element, δf_{out}, is found in the same manner by integrating instead over all lower energy fractions $x' = xz$. The net change is in turn

$$\delta f(x,t) = \delta f_{\mathrm{in}} - \delta f_{\mathrm{out}} = \frac{\delta t}{t}\int_0^1 \mathrm{d}z\,\frac{\alpha_s}{2\pi}P(z)\left[\frac{1}{z}f(x/z,t) - f(x,t)\right]. \tag{3.20}$$

The splitting functions (3.15) and (3.16) are known as unregularised splitting functions due to the poles at $z = 1$ (and $z = 0$). These IR divergences can be taken care of by introducing the “plus prescription”

$$\int_0^1 \mathrm{d}x\,\frac{g(x)}{x-1_+} \equiv \int_0^1 \mathrm{d}x\,\frac{g(x)-g(1)}{x-1} \tag{3.21}$$

at $x = 1$ and compute the regularised splitting functions as $\hat{P}(z) = P(z)_+$. The regularised splitting functions $\hat{P}(z)$ are thus equal to the unregularised splitting functions $P(z)$ everywhere except at $z = 1$. With this prescription, the evolution equation may be written as the differential equation

$$t\frac{\partial f(x,t)}{\partial t} = \frac{\alpha_s}{2\pi}\int_x^1 \frac{\mathrm{d}z}{z}\hat{P}(z)f(x/z,t), \tag{3.22}$$

known as the Dokshitzer-Gribov-Lipatov-Altarelli-Parisi (DGLAP) equation. The generalisation including several types of partons is found by including a sum over all different parton distributions. The initial values of f at $[x,1]$ and a scale t_0 must be fixed through experimental data. These depend on the probed hadron, but are process independent. For instance, one may determine $f_i^p(x,t)$ for a proton from a mixture of pp and e^-p collisions, and in turn apply this to neutrino-nucleon scattering. The DGLAP equation is the same in a time-like process, but the boundary conditions and evolution direction is changed. In this case, the virtuality decreases until it reaches a chosen cut-off $t_0 \sim \Lambda_{\mathrm{QCD}}$, at which non-perturbative effects becomes important.

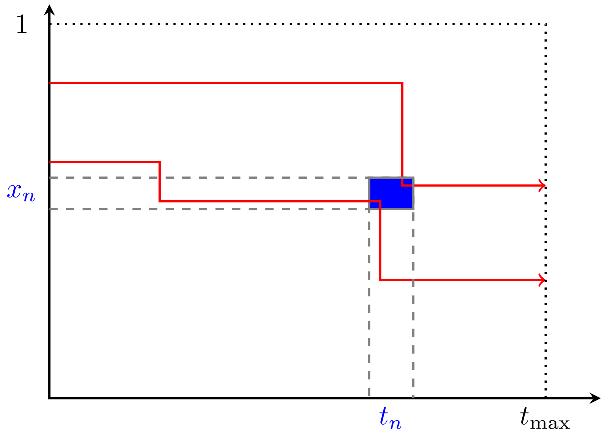

Figure 3.3: The evolution of two possible paths (x, t). Both paths are entering and leaving the element $(\delta x, \delta t)$.

The DGLAP equation has a probabilistic interpretation, and can thus be solved using a MC approach. This method is preferred since it is more flexible compared to a numerical integration and allows the addition of hadronisation models and experimental cuts. A MC scheme can be found by introducing the so-called Sudakov form factor,

$$\Delta(t) \equiv \exp\left\{-\int_{t_0}^{t} \frac{\mathrm{d}t'}{t'} \int \mathrm{d}z\, \frac{\alpha_s}{2\pi} P(z)\right\}, \tag{3.23}$$

to the evolution equation (3.20), which after integration can be written as

$$f(x,t) = \Delta(t) f(x,0) + \int_0^t \frac{\mathrm{d}t'}{t'} \frac{\Delta(t)}{\Delta(t')} \int \frac{\mathrm{d}z}{z} \frac{\alpha_s}{2\pi} P(z) f(x/z, t') \tag{3.24}$$

The first term is the contribution from (t, x)-paths that do not branch between 0 and t. The factor $\Delta(t)$ can thus be interpreted as the probability of evolving the system from 0 to t without branching. Likewise, the factor $\Delta(t)/\Delta(t')$ represents the probability for a parton to not branch. Due to the $1/t$ singularity, a cut-off t_0 must be introduced. This IR cut-off serves as a regulator to the splitting functions, $z_{\min} = \sqrt{t_0/t}$ and $z_{\min} = 1 - \sqrt{t_0/t}$, and boundary to the non-perturbative regime at $t_0 \gg \Lambda_{\mathrm{QCD}}$. Furthermore, the different branches can be taken into account by summing over all possible splitting functions, in which case the Sudakov form factor (3.23) becomes

$$\Delta_i(t) \equiv \exp\left\{-\sum_j \int_{t_0} \frac{\mathrm{d}t'}{t} \int_{z_{\min}}^{z_{\max}} \frac{\alpha_s}{2\pi} P_{ji}(z)\right\}. \tag{3.25}$$

Everything is now set to create a simple MC scheme. Consider a time-like cascade. For each step $(t_n, x_n) \to (t_{n+1}, x_{n+1})$, the equation

$$r = \frac{\Delta(t_n)}{\Delta(t_{n+1})} \tag{3.26}$$

is solved for t_{n+1}, where the quantity r is a random number chosen from an uniform distribution $r \in [0, 1]$. If t_{n+1} is smaller than the cut-off t_0 the cascade stops. Otherwise, the branching type and energy fraction $z = x_{n+1}/x_n$ must be determined according to the probability distribution $\alpha_s P_{ij}(z)$ (eqs. (3.16) and (3.15)). This process is continued until the cascade stops.

The discussions in this section have described the development of a simple MC scheme that computes a parton shower without any angular ordering. However, the angular distribution of the final product is often needed. This can be found by considering coherence effects, which effectively replaces the propagator factor $\mathrm{d}t\,/t$ by $\mathrm{d}\zeta\,/\zeta$, where $\zeta \approx 1 - \cos\theta$ is the new evolution variable. The azimuthal angle ϕ should in general take into account the polarisation corrections discussed earlier.

3.4.3 Hadronisation models

The result after a time-like parton shower is a set of partons with virtualities around the chosen cut-off t_0. At this point one reaches a long distance and low momentum transfer regime where non-perturbative effects becomes important. The most important effect is hadronisation, which at present cannot be deduced from first principles and a phenomenological model must thus be employed. Here, we will discuss the main assumptions and properties in some models.

Consider first a pure phenomenological model. Let a set of fragmentation functions $f_i^h(z, t_0)$ describe the probability that a that a parton i with an energy E creates a hadron h with an energy zE. The functions $f_i^h(z, t_0)$ can in principle be determined from experiments. Let $D_i(x, \sqrt{s}, t_0)$ denote the parton spectra obtained after a perturbative time-like parton shower from $t \sim \sqrt{s}$ to t_0. The hadron spectra, $D_h(x, \sqrt{s})$, can in this case be found by multiplying the parton spectra D_i by the fragmentation functions f_i^h under the constraint $x = x'/z$, analogous to (3.19). The result is

$$D_h(x, \sqrt{s}) = \sum_{i=q,g} \int_x^1 \frac{\mathrm{d}z}{z} D_i(x/z, \sqrt{s}, t_0) f_i^h(z, t_0). \tag{3.27}$$

This is a simple example of a so-called *independent hadronisation*. As an alternative, one can develop models that capture basic properties of QCD, such as asymptotic freedom and confinement. Two examples of such classes of models are *cluster hadronisation* and *string hadronisation*.

Cluster hadronisation is based on the idea of pre-confinement. That is, it is assumed that the parton spectra after the shower are distributed in colour-singlet clusters of partons. These clusters will in turn decay into observed hadrons. Note, however, that the state after the parton shower consists mostly of gluons. Perhaps the simplest method of creating such colour-singlet clusters is to force a splitting $g \to q\bar{q}$ as an intermediate step.

String hadronisation often refer to the Lund model, but is in truth a class of models with the same starting point. The potential between an oppositely coloured quark-antiquark pair is assumed to attractive. Lattice QCD calculations indicates that $V(r) \approx \kappa r$ at large distances. Thus, the force lines due to colour confinement are concentrated in narrow tubes that can be viewed as a string with a tension κ that pulls the pair together. The string models use this string to describe the hadronisation process. Consider as an example the simple process $e^+e^- \to q\bar{q}$. If other interactions are neglected, the distance between the quark-antiquark pair will oscillate harmonically. However, what occurs instead is that a new quark-antiquark pair is created such that two colour-singlet states $(q\bar{q})(q\bar{q})$ are formed.

Both the cluster and string hadronisation are theoretically well motivated, but includes a large number of assumptions and parameters needed to model the final momentum distributions of the produced mesons and baryons. The models must thus be calibrated to experimental data. At the end, it is difficult to determine which model is the best one.

3.4.4 Event generators

In this thesis we will be using an event generator to model the antiproton and antineutron spectra resulting from particle collisions. These nucleons will in turn be used to study the formation of antideuteron, antitritium and antihelium-3. This chapter has described the main principles utilised when estimating the particle production in a particle collision, and we are now ready to give a general overview of the calculations performed by the event generator. As an example, consider an e^-e^+ collision at the Z resonance with a hadronic decay. A simplistic overview of this process is shown in figure 3.4. The initial process $e^+e^- \to Z \to q\bar{q}$ is computed using perturbative QFT to a fixed order, and the relative cross sections for the possible output particles $q = \{u, d, c, s, b\}$ are computed.[2] In each event, the event generator picks out the output particles based on the relative cross sections in a MC fashion. The event generator performs next a time-like parton showering as described in section 3.4.2. Finally, a hadronisation scheme is performed on the final partons. At the end, one can add decay of short-lived particles.

There exists a vast number of MC event generator, each with its own special area of expertise. We will be using Pythia 8 [45, 46], which is specialised to lepton-lepton, hadron-hadron and hadron-lepton collisions at energies $10\,\text{GeV} \lesssim \sqrt{s} \lesssim 100\,\text{TeV}$. Pythia includes the branchings $q \to qg$, $g \to gg$, $g \to qq$, $q \to q\gamma$ and $l \to l\gamma$, where l is a lepton. Loop calculations are usually performed to leading order with higher order corrections provided by initial state showering. Hadrons, for example, can be viewed as a cloud of partons such that a hadron-hadron collision is influenced by multiple scatterings between the partons in the parton clouds. This hard process is described by a space-like showering. In turn, a time-like showering follows, as described above. Similarly, a lepton may be viewed as if it is surrounded by photons and partons. In any case, the process $e^+e^- \to Z/\gamma^* \to q\bar{q}$ is in Pythia also implemented with second order loop calculations including QCD matrix

---

[2] The top quark has a mass that is much larger than m_Z, and does not contribute.

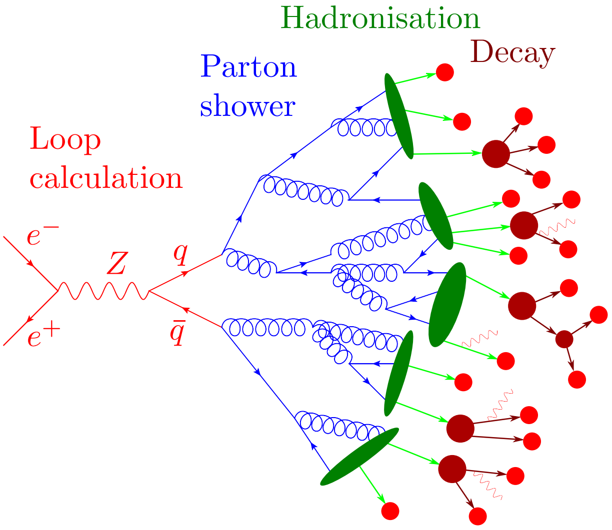

Figure 3.4: A simplistic overview of one event of the process $e^+e^- \to Z \to q\bar{q} \to$ hadrons in a MC event generator.

elements. Finally, the hadronisation scheme in Pythia is based on string fragmentation.

Note that there are three characteristic time and distance scales in the process $XY \to$ hadrons [47]. The annihilation during the hard process occurs on the time-scale $t_{\text{ann}} \sim 1/\sqrt{s}$. Thus, this time is suppressed at large energies $\sqrt{s} \gg \Lambda^2_{\text{QCD}}$. Thereafter the process proceeds with parton branchings with characteristic momentum transfers $|q^2| \gg \Lambda_{\text{QCD}}$ and stops when the virtuality is $t \sim \text{few} \times \Lambda_{\text{QCD}}$. Therefore, the longitudinal proper distance scales are smaller than $\Lambda^{-1}_{\text{QCD}}$. This means that the longest time and distance scales are related to the hadronisation process, which occurs on the order $L_{\text{had}} \sim R_{\text{had}}E_{\text{had}}/m_{\text{had}} = \gamma R_{\text{had}}$, where R_{had} is the hadronic size.

4 Coalescence

The standard (anti)nucleus formation model used when computing cosmic ray (anti)nuclei yields is the so-called *coalescence model*, first proposed by Schwarzschild and Zupančič in 1962 [5]. In the coalescence model, all nucleons within a sphere of radius p_0 in momentum space coalesce and form a nucleus. The nuclei are thus formed from a set of nucleons that have nearly completed their formation. Traditionally, the production of nuclei with mass number A and electronic charge Z is parametrised by

$$E_A \frac{\mathrm{d}^3 N_A}{\mathrm{d}P_A^3} = B_A \left(E_p \frac{\mathrm{d}^3 N_p}{\mathrm{d}P_p^3} \right)^Z \left(E_n \frac{\mathrm{d}^3 N_n}{\mathrm{d}P_n^3} \right)^{A-Z} \Bigg|_{P_p = P_n = P_A/A} , \tag{4.1}$$

where $E_i \, \mathrm{d}^3 N_i / \mathrm{d}P_i^3$ denotes the invariant yield and B_A is known as the coalescence parameter [5, 6]. The physical interpretation of B_A is debated. For example, in e^+e^- and DM annihilations, and pp collisions one typically imposes the coalescence condition in momentum space, requiring that the momentum difference between two nucleons in their centre-of-momentum (CoM) frame is less than a given value p_0, known as the coalescence momentum. It is assumed that all microphysics, such as spin and isospin, is contained in p_0. In the approximation of isotropic nucleon yields, the coalescence momentum is connected to B_A by

$$B_A = A \left(\frac{4\pi}{3} \frac{p_0^3}{m_N} \right)^{A-1} . \tag{4.2}$$

This will be called the *spectral model* in this text and will be discussed further in section 4.1.1. The coalescence scheme can be improved by including two-particle correlations provided by a MC event generator on an event-by-event basis. This will be called the *MC approach* and will be discussed in section 4.1.2. Due to the lack of a microphysical picture, the parameter p_0 is a free parameter that must be calibrated by experimental data, as will be done in section 4.2 with emphasis on the MC approach. Some alternatives to the coalescence model will be discussed in section 4.1.3.

Note that the discussions of the formation models in principle apply equally well to particles as to antiparticles, and the prescription ‘anti’ is thus dropped.

4.1 Existing coalescence models

4.1.1 Spectral model

Consider the coalescence of a proton and a neutron with four momenta k_p^μ and k_n^μ, respectively, into a deuteron with four momentum $k_d^\mu = k_p^\mu + k_n^\mu$. Due to the low binding energy of the deuteron, $E_b = 2.2\,\mathrm{MeV}$, the deuteron can be assumed to be at rest in the CoM frame of the nucleons, which we will call the *deuteron* (or nucleus) frame. The CoM frame of the incident particles in the particle beam will be called the *lab frame*. Furthermore, energy and momentum conservation is assumed, although there is in reality some excess energy due to the binding energy of the deuteron that is carried away by e.g. a photon. It is convenient to further assume that $m_d = 2m_p = 2m_n$. The spectral model in the context of cosmic ray antinuclei is discussed in e.g. Refs. [1, 7, 48, 49] and references therein.

In the coalescence model, the probability that a given proton and neutron pair coalesces is given by the probability that the neutron is within a distance p_0 of the proton in the deuteron frame. The parameter p_0 is generally small and the particles are thus assumed to be in the same Lorentz frame. However, the Lorentz transformation between the lab frame and the CoM frame cannot be neglected and will be treated later. Let $\mathrm{d}^3N_i/\mathrm{d}k^3$ be the non-relativistic number density of nucleon i in the deuteron frame. When assuming that the proton and neutron momenta are uncorrelated, the deuteron spectrum can be written as

$$\begin{aligned}\frac{\mathrm{d}^3N_d}{\mathrm{d}k_d^3} &= \frac{\mathrm{d}^3N_p}{\mathrm{d}k_p^3}\int \mathrm{d}^3k\,\frac{\mathrm{d}^3N_n}{\mathrm{d}k_n^3}\Theta\left(k^2 < p_0^2\right)\\ &= \frac{4\pi p_0^3}{3}\frac{\mathrm{d}^3N_p}{\mathrm{d}k_p^3}\frac{\mathrm{d}^3N_n}{\mathrm{d}k_n^3}.\end{aligned} \tag{4.3}$$

In the second step it was further assumed that the number density of the neutron around the proton is spherically symmetric and that it is approximately constant. The latter is true since p_0 in general is small.

In order to compare to experiments, the expression (4.3) must be transformed to the lab frame. This can be achieved by considering the Lorentz invariant quantity $\mathrm{d}^3k\,/E$. According to equation (A.12), one finds

$$\mathrm{d}^3k' = \frac{E}{E'}\,\mathrm{d}^3k = \gamma\left(1 + \frac{vk_x}{\sqrt{m_i^2 + k^2}}\right)\mathrm{d}k_x\,, \tag{4.4}$$

where $v < 1$ is the velocity of the deuteron in the lab frame. The second term in the parentheses can be neglected since only nucleons with a small momentum in the deuteron frame will coalesce.[1] The relation between the number densities in CoM and lab systems

---

[1] The term is always smaller than $p_0/\sqrt{p_0^2 + m_i^2} \sim 0.1$ since $k_x \leq p_0 \sim 0.1\,\mathrm{GeV} \ll m_p$.

becomes

$$\left(\frac{\mathrm{d}^3 N_i}{\mathrm{d}k_i^3}\right)_{\boldsymbol{k}=0} = \gamma_i \left(\frac{\mathrm{d}^3 N_i}{\mathrm{d}k_i'^3}\right)_{\boldsymbol{k}_i'}, \tag{4.5}$$

where γ_i is the Lorentz factor of the deuteron frame relative to the lab frame. Each of the three number densities in equation (4.3) will thus receive a factor γ. By dropping the primes, one arrives at the expression

$$\frac{\mathrm{d}^3 N_d}{\mathrm{d}k_d^3} = \frac{1}{8}\frac{4\pi p_0^3}{3}\gamma \left(\frac{\mathrm{d}^3 N_p}{\mathrm{d}k_p^3}\right)_{\boldsymbol{k}_p=\frac{\boldsymbol{k}_d}{2}} \left(\frac{\mathrm{d}^3 N_n}{\mathrm{d}k_n^3}\right)_{\boldsymbol{k}_n=\frac{\boldsymbol{k}_d}{2}}, \tag{4.6}$$

where the momenta $\boldsymbol{k}_i$ and the densities $\mathrm{d}^3 N_i/\mathrm{d}k_i^3$ are given in the lab frame. The extra factor $1/8$ is added so that p_0 is interpreted as the momentum difference of the nucleons. By comparing with equation (4.1) with $A = 2$ and $Z = 1$, one obtains the coalescence parameter (4.2). The generalisation to larger nuclei is straight forward.

It is often convenient to express the coalescence model in terms of an expression of the energy spectrum. This can be achieved by using the assumption that the spectra are isotropic,

$$\left(\frac{\mathrm{d}^3 N_i}{\mathrm{d}k_i^3}\right)_{\boldsymbol{k_i}} = \frac{1}{4\pi k_i^2}\left(\frac{\mathrm{d}N_i}{\mathrm{d}k_i}\right)_{k_i=|\boldsymbol{k}_i|}. \tag{4.7}$$

We will be expressing the energy spectrum in terms of the kinetic energy $T = E - m$. The previously used approximations $m_p = m_n = 2m_d$ and $\boldsymbol{k}_{\bar{p}} = \boldsymbol{k}_{\bar{n}} = \boldsymbol{k}_{\bar{d}}/2$ imply $T_n = T_p = T_d/2$. By expressing the Lorentz factor γ by the kinetic energy T, equation (4.6) can be written as

$$\frac{\mathrm{d}N_d}{\mathrm{d}T_d} = \frac{p_0^3}{4m_d}\frac{1}{\sqrt{T_d^2 + 2m_d T_d}}\left(\frac{\mathrm{d}N_n}{\mathrm{d}T_p}\right)_{T_p=\frac{T_d}{2}}\left(\frac{\mathrm{d}N_n}{\mathrm{d}T_n}\right)_{T_n=\frac{T_d}{2}}, \tag{4.8}$$

which is the final expression for the deuteron energy spectrum.

The spectral model is expected to be inaccurate and qualitatively wrong for several reasons [7]. Consider for example the $\mathrm{W}^+\mathrm{W}^-$ annihilation channel of a DM particle χ. If the mass of the DM particle m_χ increases, the boost of the $\mathrm{W}^\pm$, and thereby the antideuterons, will increase. The final particles will thus be concentrated in two jets in opposite directions, making the final energy spectrum highly non-spherical. The isotropy approximation is therefore expected to be invalid. Moreover, the particles will be concentrated in QCD jets, increasing the probability that a given pair coalesce. The approximation of uncorrelated nucleons may also over-estimate the deuteron production by neglecting the anti-correlation between the protons and neutrons. For example, a proton that originates from W^+ and a neutron from W^- may coalesce in the spectral model, but this process should be highly suppressed. Lastly, one can note that that deuterons should only form if there are at least one proton and one neutron in the final state. At low beam energies, this leads to a reduced available phase space volume that can be taken into account by introducing an energy dependent correlation factor R_n [50]. In this text, we will only consider experiments with $\sqrt{s} \gtrsim 70\,\mathrm{GeV}$ and R_n can thus be neglected. In order to take the aforementioned effects into account, coalescence should be checked per-event within the MC.

4.1.2 Monte Carlo approach

In the MC coalescence approach, first used by Kadastik et al. in 2010 [7], the coalescence condition is checked per-event within the MC. As before, we start by considering the coalescence of deuterons. In this approach, a proton and neutron merge if their relative momentum difference is less than p_0 in the deuteron frame.[2] All pairs fulfilling this condition will thus form a deuteron with energy $E_d = E_p + E_n$ and momentum $\boldsymbol{k}_d = \boldsymbol{k}_n + \boldsymbol{k}_n$. Let from now on the subscript 'd' indicate that the quantity is evaluated in the deuteron frame. This frame is characterised by $\boldsymbol{k}_{p,\mathrm{d}} = -\boldsymbol{k}_{n,\mathrm{d}}$, which implies that the coalescence condition can be expressed as

$$\Delta k = 2|k_{p,\mathrm{d}}| = 2\sqrt{E_{p,\mathrm{d}}^2 - m_p^2} < p_0. \tag{4.9}$$

In the event generator Pythia 8, all output quantities are given in the lab frame, and in order to evaluate the coalescence condition (4.9), the quantities must be transformed to the deuteron frame. One method to achieve this is to re-express the coalescence condition in terms of a Lorentz invariant quantity. We will be using the Mandelstam variable $s = (E_p + E_n)^2 - (\boldsymbol{p}_p + \boldsymbol{p}_n)^2$ defined in equation (A.10). The energy of the proton in the deuteron frame can thus be expressed in terms of s as (see equation (A.11))

$$E_{p,\mathrm{d}} = \frac{s + m_p^2 - m_n^2}{2\sqrt{s}}. \tag{4.10}$$

In essence, the coalescence condition can be evaluated by computing s in the lab frame and then using equation (4.10) and (4.9). In each event there is a chance that there is more than one proton-neutron pair that fulfils the coalescence criteria. However, this can in most cases be neglected.

There are three main problems with the MC approach: it is phenomenological, classical and includes only the separation of the nucleons in momentum space. Most event generators, such as Pythia 8 used here, do not model the space-time structure resulting from the showering and hadronisation. Nonetheless, in 2013 Ibarra and Wild [51] noted that the spatial separation should also be taken into account: the nuclear forces and interactions that are responsible for the binding of the deuteron have a range in the

---

[2] Alternatively, one may require that the invariant momentum difference is less than p_0. These methods is equivalent in the limit of equal nucleon masses $m_p = m_n$.

order of a few femtometre, while weakly decaying particles may have microscopic decay lengths. The nucleons produced from weakly decaying particles will therefore be too far from the primary interaction to be able to coalesce with nucleons produced in the hadronisation process or from other weak decays. They therefore excluded decaying particles with proper lifetimes $\tau < 1\,\mathrm{mm}$, which in consequence neglected the contribution from antinucleons produced in weak decays such as from $\bar{\Lambda}^+$ and $\bar{\Sigma}^\pm$. Fornengo et al. [52] implemented as an alternative the condition that only nucleons produced within a spatial region $\Delta r < 2\,\mathrm{fm}$ of the primary interaction would be able to coalesce, which in principle is a more physically correct approach.[3] However, the difference between the two models is small [8]. In Pythia 8 the treatment by Ibarra and Wild is nearly equivalent to excluding nucleons from decays with a non-zero decay length as only non-zero lifetimes that are relevant for displaced vertices in collider experiments are stored in the event table. In other words, there is only a small difference in requiring $\tau = 0\,\mathrm{mm}$ instead of $\tau < 1\,\mathrm{mm}$ in Pythia 8. This treatment will be adopted in the computations in this thesis.

There are two obvious methods to generalise the per-event coalescence model to helium-3 and tritium. One can require that each of the relative momenta lie within a sphere with radius p_0 in momentum space, or require that the absolute momentum difference between each particle pair is less than p_0 [53, 54]. The latter will be used here.

4.1.3 Alternative models

In heavy ion collisions the coalescence parameter B_A in equation (4.1) is usually defined in terms of the emission region V of hadrons from the expanding clouds of partons, giving $B_A \propto V^{A-1}$. Reference [55] developed a model which describes the coalescence parameter in terms of a dynamical interaction volume parametrisation that can be fixed using the same hadronic emission volume which is probed by Bose-Einstein two-particle correlation spectrometry.[4] This treatment has recently been used to study cosmic ray antideuterons in order to obtain a process dependent coalescence parameter in pp collisions [56]. As will be seen in the next section, the coalescence momentum p_0 (and thus also B_A) still depends on amongst other the hadronisation model and beam energy $\sqrt{s}$, implying that this model still should be tuned for each analysis. Recently, p_0 has been fitted to data on antideuteron production from proton-nucleus collisions using an empirically energy dependent parametrisation in order to reproduce the large differences in p_0 [57]. One can note that this has not been discussed for e^+e^- annihilations, which one expects to be more similar to DM annihilations.

Few per-event alternatives to the coalescence model exist. Dal and Raklev [58] proposed a model where a deuteron is produced by a nucleon pair $\bar{N}_1\bar{N}_2$ with an invariant

---

[3] This condition can be implemented by neglecting the decay of particles with a momentum large enough that it would travel a distance of 2 fm before decaying.

[4] The model is based on a quantum mechanical density matrix approach with the same starting point as we use when developing a new per-event coalescence model in the next chapter.

momentum difference Δk in a stochastic process $\bar{N}_1\bar{N}_2 \to \bar{d}X$. The probability that a process occurs is assumed to be proportional to the normalised cross section of the process, $P(\bar{N}_1\bar{N}_2) = \sigma_{\bar{N}_1\bar{N}_2\to\bar{d}X}(\Delta k)/\sigma_0$, where σ_0 is set as a free parameter. At low Δk the relevant process is the radiative capture $\bar{p}\bar{n} \to \bar{d}\gamma$, which is approximately the same as the slow nucleon capture process $\bar{p}\bar{n} \to \bar{d}^*$ considered in the coalescence model. In this alternative model, however, the antideuterons are mainly produced in resonant processes around the delta-resonance at $\Delta k \sim 1\,\mathrm{GeV}$. The authors noticed amongst other a significantly improved fit to the pp collision data from the ALICE experiment [9] discussed in section 4.2.2.

4.2 Calibration of the coalescence momentum

In order to get consistent results and check the consistency of different models, we calibrate p_0 to existing experiments for Pythia 8 rather than quoting an existing result. This will also help in the comparison with the development of a new model, which is the main focus of this thesis.

The coalescence model has one free parameter, the coalescence momentum p_0, which needs to be calibrated to existing experimental data due to the lack of a microscopic understanding of the model. In order for the coalescence model to be predictive, p_0 should be independent of the reaction type and CoM energy $\sqrt{s}$. However, different data sets give different values for p_0. A value between 133 to 236 MeV is often quoted in the literature for Pythia [8, 51]. Moreover, different event generators, such as Herwig++, Pythia 6 and Pythia 8, gives different results [59, 60]. Here we will also show that different versions of Pythia 8 may yield different results.

The coalescence parameter should be the same for nuclei and antinuclei. In fact, data from the ALICE collaboration indicates that the deuteron and antideuteron data yields consistent calibration [58]. Thus, existing and new data on deuteron production can be used to calibrate the coalescence models. Nevertheless, we will only consider the production of antinuclei, which removes possible background noise and secondary remnants. Furthermore, we will only consider e^+e^- annihilations and pp collisions, which are the two most important astrophysical processes related to cosmic ray antideuteron and antihelium. The former is expected to be similar to DM annihilations, while the latter gives the main contributions to the secondary antiparticle fluxes. This will be discussed in chapter 6.

4.2.1 Electron-positron annihilation

The ALEPH experiment at the Large Electron-Positron Collider measured the deuteron and antideuteron production in e^+e^- collisions at the Z resonance. The production rate of antideuterons was measured to be $(5.9 \pm 1.8 \pm 0.5) \times 10^{-6}$ per hadronic Z decay in the

Table 4.1: The calibrated values of p_0 to the ALEPH experiment for the spectral model and the Monte Carlo approach with and without the spatial cut-off $\Delta\tau = 0$. The statistical and systematic errors in the experimental data were added in quadrature.

Model / p_0 [MeV]	Pythia 8.186	Pythia 8.230
MC	164^{+16}_{-19}	177^{+17}_{-22}
$\mathrm{MC}_{\Delta\tau}$	196^{+19}_{-24}	214^{+21}_{-26}
Spectral	127^{+15}_{-12}	132^{+16}_{-13}

Table 4.2: Calibration comparison to other authors using Pythia.

Reference (Pythia version)	MC	$\mathrm{MC}_{\Delta\tau}$	Spectral
Delahaye and Grefe [49] (6.4)	173^{+18}_{-19} MeV	203^{+20}_{-25} MeV	141^{+14}_{-16} MeV
Fornengo et al. [49, 52] (6.4)	180 ± 18 MeV	195 ± 22 MeV	143 MeV
Kadastik et al. [7] (8.1)	162 ± 17 MeV	-	-
Ibarra and Wild [51] (8.1)	-	192 ± 30	-

antideuteron momentum range from 0.62 to 1.03 GeV and a production angle θ satisfying $|\cos\theta| < 0.95$ [10]. The first uncertainty is the statistical and the second is the systematic, which we add in quadrature.

In order to calibrate p_0 to this experiment, the e^+e^- collisions at Z resonance with hadronic decay was reproduced in Pythia 8.230 and Pythia 8.186. About 10^7 events were used in the spectral model, while 10^9 events were used in the MC approach. The final results for p_0 are listed in table 4.1 with and without the spatial cut-off $\Delta\tau = 0$. A short list of the p_0 values from other papers are shown in table 4.2 for comparison, which in all cases are different from the result obtained here. However, note that there are no values for exactly the same version of Pythia and "spatial cut-off" which may explain the discrepancy. Note also that there is a significant difference in p_0 between Pythia 8.230 and 8.186 which is likely due to calibration and updated experimental values in the event generator. From now on, only the MC approach will be used.

In a similar experiment performed by the OPAL collaboration [11] at the Large Electron-Positron Collider, no antideuteron events were detected. Reference [58] notes that this has previously been neglected in the calibration, but should also be considered. The measurements was performed in the antideuteron momentum range 0.35 to 1.1 GeV with an estimated detection efficiency $\epsilon = 0.234$, which includes the angular acceptance.

The expected number of detected events is

$$N_{\bar{d}} = \epsilon N_{\rm ev} n_{\bar{d},\rm MC}, \tag{4.11}$$

where $N_{\rm ev} = 1.64 \times 10^6$ is the number of events accepted by the OPAL analysis and $n_{\bar{d},\rm MC}$ is the MC prediction on the number of antideuterons per event. We now follow Ref. [58] and assume a Poissonian uncertainty $\sigma = \sqrt{N_{\bar{d}}}$ for the expected number of events. The χ^2 is in this case given by

$$\chi^2_{\rm OPAL} = \frac{(N_{\rm obs} - N_{\bar{d}})^2}{\sigma^2} = N_{\bar{d}}. \tag{4.12}$$

By performing a combined χ^2 analysis, we obtain $p_0 = 201\,\mathrm{MeV}$ and $\chi^2/(N-1) = 3.16$ with Pythia 8.230, and $p_0 = 184\,\mathrm{MeV}$ and $\chi^2/(N-1) = 3.20$ with Pythia 8.186. The latter is consistent with the result in Ref. [58]. From now on, only Pythia 8.230 and the MC approach will be used.

4.2.2 Proton-proton collision

The ALICE collaboration at LHC measured the invariant differential yields of deuterons and antideuterons in inelastic proton-proton collisions at centre of mass energies $\sqrt{s} = 0.9$, 2.76 and 7 TeV in the transverse momentum range $0.8 < p_T < 3\,\mathrm{GeV}$ and rapidity $|y| < 0.5$ [9].[5] Furthermore, the antihelium-3 yield was given for $\sqrt{s} = 7\,\mathrm{TeV}$. The results were represented as the invariant differential yield

$$E\frac{\mathrm{d}^3 n}{\mathrm{d}p^3} = \frac{1}{N_{\rm inel}}\frac{1}{2\pi p_T}\frac{\mathrm{d}^2 N}{\mathrm{d}p_T\,\mathrm{d}y}, \tag{4.13}$$

where E is the energy of the (anti)nucleus, $N_{\rm inel}$ is the number of inelastic events, N is the number of (anti)nucleus events and $n \equiv N/N_{\rm inel}$. The experiment included a trigger (V0) consisting of two hodoscopes of 32 scintillators that covered the pseudo-rapidity ranges $2.8 < \eta < 5.1$ and $-3.7 < \eta < -1.7$ used to select non-diffractive (ND) inelastic events. An event was triggered by requiring a hit (charged particle) on either side of the V0 trigger.

Pythia 8 can generate inelastic events consisting of single-diffractive, double-diffractive (DD) and ND events. The minimum bias events selected by the V0 trigger will in practice also include events that Pythia considers as single-diffractive and DD events. The corresponding trigger efficiencies for the V0 trigger are summarised in table 4.3 with and without the lifetime cut-off $\Delta\tau = 0$, from which one can deduce that the ND events generate more than one order of magnitude more triggered events than the DD and ND events.

---

[5] Note that a pseudo-rapidity cut $|\eta| < 0.8$ was required in the data selection to avoid edge effects, but the data outside $|\eta| < 0.8$ and inside $|y| < 0.5$ were extrapolated using a MC simulation.

Table 4.3: Estimated trigger efficiency of the trigger V0 for all types of inelastic events produced by Pythia 8.230. The values were estimated using eight runs of 10^7 inelastic events for each $\tau_{\max}$ and $\sqrt{s}$ setting. The uncertainties are given as the standard deviations resulting from these runs. The last three rows states the fractions of the different types of inelastic events that occur when inelastic events are produced (relative cross sections).

	$\sqrt{s}$ / %	ND	DD	SD	inel.
$\tau_{\max} = 0$	0.9 TeV	97.2 ± 0.0	35.6 ± 0.1	22.9 ± 0.1	75.2 ± 0.0
	2.76 TeV	98.3 ± 0.0	34.8 ± 0.0	29.2 ± 0.0	78.1 ± 0.0
	7 TeV	98.8 ± 0.0	36.0 ± 0.1	33.4 ± 0.0	80.3 ± 0.0
No $\tau_{\max}$ limit	0.9 TeV	97.8 ± 0.0	36.9 ± 0.0	23.5 ± 0.0	75.8 ± 0.0
	2.76 TeV	98.7 ± 0.0	35.9 ± 0.0	29.7 ± 0.0	78.6 ± 0.0
	7 TeV	99.0 ± 0.0	37.0 ± 0.0	33.8 ± 0.0	80.7 ± 0.0
Relative cross sections	0.9 TeV	68.5 ± 0.0	11.1 ± 0.0	20.4 ± 0.0	100
	2.76 TeV	69.8 ± 0.0	11.4 ± 0.0	18.8 ± 0.0	100
	7 TeV	71.3 ± 0.0	11.4 ± 0.0	17.3 ± 0.0	100

One may thus assume that the deuteron spectrum is governed by the deuterons produced in ND events, produce pure ND events and then scale the result according to the trigger efficiencies. This was done by Ref. [58]. From table 4.3, one finds that the final scaling factors for $\sqrt{s} = 0.9$, 2.76 and 7 TeV are 0.877, 0.879 and 0.885, respectively.[6] However, in order to minimise the uncertainty and reproduce possible phase space distributions related to the trigger, we will generate inelastic events and check the trigger conditions per event.[7]

The result of a χ^2-fit of the coalescence model with the MC approach to the ALICE experiment is listed in table 4.4. In each run, $\mathcal{O}(10^8)$ events where used and all proton-neutron pairs that fulfilled the coalescence condition were stored. Double counting was only a concern in 0.61%, 0.94% and 1.36% of the events with a produced deuteron for $\sqrt{s} = 0.9, 2.76$ and 7 TeV, respectively, and can thus be neglected. The fits to the antideuteron data are shown in figure 4.1. The helium-3 spectrum is plotted in the next chapter.

The p_0 value is consistent between the different energies, but the fits to the experimental data are not very good. There may be two reasons for this. Firstly, the coalescence model

---

[6] Note that this differs from the given factors in Ref. [58], since there the trigger efficiencies for Pythia 6 and PHOJET from Ref. [61] are used to estimate the trigger efficiencies for Pythia 8.

[7] We performed the simulations using the scaling method as well. Using this method $p_0 = 185, 179$ and 178 MeV for $\sqrt{s} = 0.9$, 2.76 and 7 TeV, respectively.

Table 4.4: Results for the p_0 calibration to the ALICE experiment.

Experiment	p_0 [MeV]	$\chi^2/(N-1)$
$\bar{d}$; $\sqrt{s} = 0.9\,\text{TeV}$	181	7.26/2
$\bar{d}$; $\sqrt{s} = 2.76\,\text{TeV}$	174	45.0/6
$\bar{d}$; $\sqrt{s} = 7\,\text{TeV}$	176	177/19
$\bar{d}$; combined	176	229/29
${}^3\overline{\text{He}}$; $\sqrt{s} = 7\,\text{TeV}$	179	1.2/2

may be inaccurate. In the next chapter we will develop a new coalescence model that may improve this. Secondly, this discrepancy may be due to the event generator. In particular, one cannot expect that the fit to the nucleus data is better than the corresponding fit to the nucleon data. In figure 4.2 the combined proton and antiproton yield from pp collisions at $\sqrt{s} = 7\,\text{TeV}$ estimated by Pythia 8 is compared with the measured spectrum by ALICE [62]. As can be seen from the plot, there is a large discrepancy at small and large p_T, but fits quite good in the relevant region $1\,\text{GeV} \lesssim p_T \lesssim 3\,\text{GeV}$. Finally, we note that the value of p_0 for antihelium-3 is likely close to the value for antideuteron by accident, because it depends on how the coalescence model is generalised to larger nuclei, there are large experimental uncertainties and the model is phenomenological.

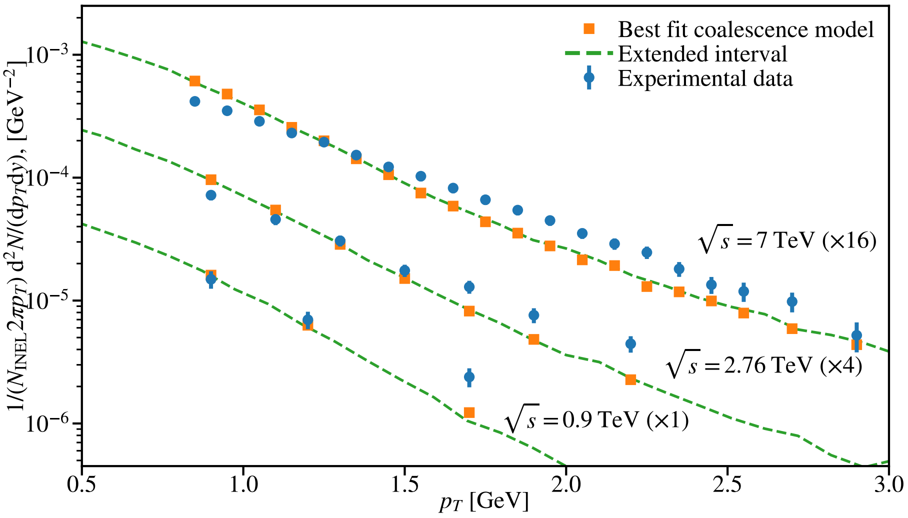

Figure 4.1: Antideuteron spectra from the ALICE experiment and best fit for the coalescence model. The experimental error-bars states the systematic and statistical added in quadrature. The data is multiplied by a constant factor in order to make the figure clearer.

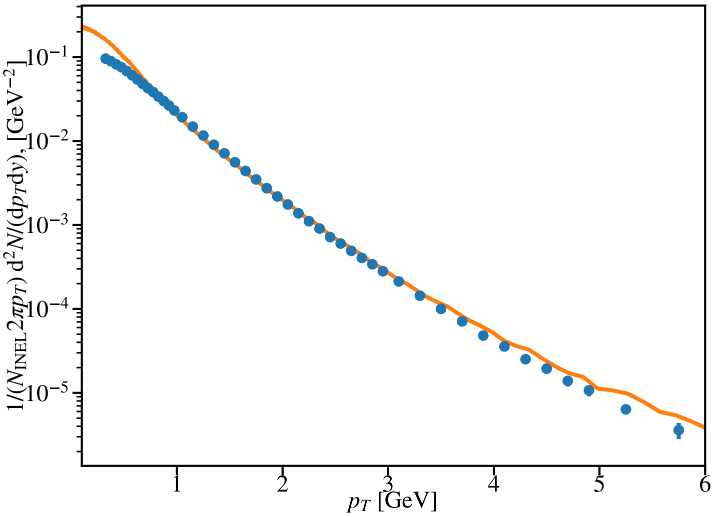

Figure 4.2: Combined antiproton and proton production spectrum from pp collisions as measured by the ALICE experiment (blue dots) and as estimated by Pythia 8.230 (orange line).

5 Developing a new coalescence model

The main focus of this thesis is to study the coalescence of antiprotons and antineutrons into antideuteron, antitritium and antihelium-3 in the context of indirect DM searches. The current state-of-the-art MC approach of the coalescence model, described in the previous chapter, is a classical and phenomenological model that only includes constraints on the momentum variables. In contrast, in nuclear collisions one often includes constraints on the spatial emission volume of the event instead. It is therefore desirable to derive a quantum mechanical formation model with a clear microphysical picture that includes constraints on both momentum and space variables.

Here we develop a new coalescence model based on the Wigner function representations of the produced antinuclei states, which allows us to include both the size of the formation region and momentum correlations in a semi-classical picture.[1] The formation region is process dependent, while the momentum correlations can be obtained from the MC event generator. The final model contains one free parameter that will be estimated using a microphysical picture for different processes, and calibrated by the experimental data considered in the previous chapter. In the following *lab frame* refers to the CoM frame of the original particle beam, while *deuteron (nucleus) frame* refers to the frame in which the final deuteron (nucleus) is at rest.

The main results of this chapter have been published in Ref. [63].

5.1 Wigner function based deuteron formation model

First we develop the new Wigner function based model for the case of deuteron production. The generalisation to helium-3 and tritium is straight forward, and is discussed in the next section. The derivation of the model rely on the fact that the binding energy of the nuclei is small ($B \approx 2.2\,\mathrm{MeV}$ for deuteron), such that a nucleus is formed through the nucleon capture process $n_1 + ... + n_n \to N^*$ with $k^\mu_{n_1} + ... + k^\mu_{n_n} = k^\mu_N$, and that the excitation energy is later released by the emission of a photon.[2]

---

[1] A short introduction to Wigner functions with the conventions for the normalisation used here is given in appendix B.

[2] One way of checking that this is a valid approximation is to use a different form of the four-momentum of the deuterons such as $p^\mu_d = \left(\sqrt{m_d^2 + [\boldsymbol{p}_p + \boldsymbol{p}_n]^2}, \boldsymbol{p}_p + \boldsymbol{p}_n\right)$. Both this and letting the excess energy be carried away by a photon has a minute effect on the final results.

5.1.1 Derivation

The derivation between equations (5.2) and (5.5) is inspired by the discussions by Scheibl and Heinz [55] on the analytical treatment of the coalescence of two and three nucleon clusters in heavy ion collisions. One main difference is that we here use the two-particle Wigner functions, such that two-particle correlations are considered. From there we make an ansatz on the Wigner function of the nucleons, enabling the derivation of a per-event coalescence model. Due to the low binding energy of the deuteron, only nucleon pairs with a low relative momentum will coalesce. The relative motion of the two nucleons and the coalescence into deuteron can therefore be treated non-relativistically. However, Lorentz transformation between the deuteron frame and the lab frame should in general be taken into account, but this issue is postponed until section 5.1.3.

Consider a system of particles consisting of N_p protons and N_n neutrons. The number of deuterons with momentum $\boldsymbol{P}_d$ can be found by projecting the deuteron density matrix ρ_d onto the two-nucleon density matrix ρ_{nucl},

$$\frac{\mathrm{d}^3 N_d}{\mathrm{d}P_d^3} = \mathrm{tr}\{\rho_d \rho_{\text{nucl}}\}. \tag{5.1}$$

As will be discussed in section 5.1.2, the deuteron is only manifested in nature as an isospin singlet, and its density matrix therefore has to describe a pure state, $\rho_d = |\phi_d\rangle\langle\phi_d|$. The Wigner functions of the nucleons will be assumed to not contain any dynamical correlations with respect to isospin and spin, and the coalescence into all possible spin and isospin states will be considered by adding a statistical factor S. This will be discussed in section 5.1.2. Thus, the two-nucleon state can be written as the pure state $\rho_{\text{nucl}} = |\psi_p\psi_n\rangle\langle\psi_p\psi_n|$ with the normalisation $\langle\psi_n\psi_p|\psi_p\psi_n\rangle = N_p N_n$. For the moment, we neglect possible double counting, but will later be included in section 5.1.5.

The trace in equation (5.1) can be evaluated in the position representation $|\boldsymbol{x}_1'\boldsymbol{x}_2'\rangle$, where the two indices refer to the two nucleons in the initial state. Let for example x_1 refer to the proton and x_2 refer to the neutron. By choosing to evaluate the trace in this representation and inserting the unity operator $\mathbb{1} = \int \mathrm{d}^3x\,|x\rangle\langle x|$ in equation (5.1), we obtain[3]

$$\begin{aligned}\frac{\mathrm{d}^3 N_d}{\mathrm{d}P_d^3} =& S\int \mathrm{d}^3x_1\,\mathrm{d}^3x_2\,\mathrm{d}^3x_1'\,\mathrm{d}^3x_2'\,\langle\boldsymbol{x}_1',\boldsymbol{x}_2'|\phi_d\rangle \\ &\times \langle\phi_d|\boldsymbol{x}_1\boldsymbol{x}_2\rangle\langle\boldsymbol{x}_1\boldsymbol{x}_2|\psi_p\psi_n\rangle\langle\psi_p\psi_n|\boldsymbol{x}_1\boldsymbol{x}_2\rangle \\ \equiv& S\int \mathrm{d}^3x_1\,\mathrm{d}^3x_2\,\mathrm{d}^3x_1'\,\mathrm{d}^3x_2'\,\phi_d^*(\boldsymbol{x}_1,\boldsymbol{x}_2)\phi_d(\boldsymbol{x}_1',\boldsymbol{x}_2') \\ &\times \left\langle \psi_n^\dagger(\boldsymbol{x}_2')\psi_p^\dagger(\boldsymbol{x}_1')\psi_p(\boldsymbol{x}_1)\psi_n(\boldsymbol{x}_2)\right\rangle,\end{aligned} \tag{5.2}$$

---

[3] Scheibl and Heinz [55] has an extra combinatoric factor 1/2! which comes from the fermion many particle wave function since they consider the proton and neutron as indistinguishable. The result will be the same when adding the statistical factor S.

where $\phi_d(\boldsymbol{x}_1, \boldsymbol{x}_2)$ and $\psi_i(\boldsymbol{x})$ are the wave functions of the deuteron and nucleon i, respectively.

The deuteron is observed by the detector as a free momentum eigenstate, and the deuteron wave function can thus be written as

$$\phi_d(\boldsymbol{x}_1, \boldsymbol{x}_2) = (2\pi)^{-3/2} \exp\left\{ \mathrm{i}\boldsymbol{P}_d \cdot \frac{\boldsymbol{x}_1 + \boldsymbol{x}_2}{2} \right\} \varphi_d(\boldsymbol{x}_1 - \boldsymbol{x}_2), \tag{5.3}$$

where the plane wave accounts for the CoM motion and $\varphi_d(\boldsymbol{x}_1 - \boldsymbol{x}_2)$ is the internal wave function. The two-nucleon density matrix can be written as

$$\begin{aligned} \left\langle \psi^\dagger(\boldsymbol{x}_2')\psi^\dagger(\boldsymbol{x}_1')\psi(\boldsymbol{x}_1)\psi(\boldsymbol{x}_2) \right\rangle = \int \frac{\mathrm{d}^3 p_p}{(2\pi)^3} \frac{\mathrm{d}^3 p_n}{(2\pi)^3} W_{np} \left(\boldsymbol{p}_p, \boldsymbol{p}_n, \frac{\boldsymbol{x}_1 + \boldsymbol{x}_1'}{2}, \frac{\boldsymbol{x}_2 + \boldsymbol{x}_2'}{2} \right) \\ \times \exp\{\mathrm{i}\boldsymbol{p}_n \cdot (\boldsymbol{x}_2 - \boldsymbol{x}_2')\} \exp\{\mathrm{i}\boldsymbol{p}_n \cdot (\boldsymbol{x}_1 - \boldsymbol{x}_1')\}, \end{aligned} \tag{5.4}$$

where p_p and p_n are the momentum of the proton and neutron, respectively.

The integral in equation (5.2) can now be simplified by introducing the coordinates $\boldsymbol{r}_p = (\boldsymbol{x}_1 + \boldsymbol{x}_1')/2$, $\boldsymbol{r}_n = (\boldsymbol{x}_2 + \boldsymbol{x}_2')/2$, $\boldsymbol{\xi} = \boldsymbol{x}_1 - \boldsymbol{x}_1' - (\boldsymbol{x}_2 - \boldsymbol{x}_2')$ and $\boldsymbol{\rho} = (\boldsymbol{x}_1 - \boldsymbol{x}_1' + \boldsymbol{x}_2 - \boldsymbol{x}_2')/2$, $\boldsymbol{q} = (\boldsymbol{p}_p - \boldsymbol{p}_n)/2$. The position vectors $\boldsymbol{r}_i$ are the classical positions of the proton ($i = p$) and neutron ($i = n$) and will in turn be expressed by the relative position $\boldsymbol{r} = \boldsymbol{r}_p - \boldsymbol{r}_n$ and the deuteron position $\boldsymbol{r}_d = (\boldsymbol{r}_p + \boldsymbol{r}_n)/2$. The momentum vector $\boldsymbol{q}$ is the momentum of the nucleons in the deuteron frame. The corresponding Jacobian determinant is unity and the change of basis is thus trivial: $\mathrm{d}^3 x_1\, \mathrm{d}^3 x_2\, \mathrm{d}^3 x_1'\, \mathrm{d}^3 x_2' = \mathrm{d}^3 r_p\, \mathrm{d}^3 r_n\, \mathrm{d}^3 \xi\, \mathrm{d}^3 \rho = \mathrm{d}^3 r\, \mathrm{d}^3 r_d\, \mathrm{d}^3 \xi\, \mathrm{d}^3 \rho$. The ρ integral leads to a δ-function accounting for the momentum conservation $\boldsymbol{P}_d = \boldsymbol{p}_1 + \boldsymbol{p}_2$. With these new coordinates, equation (5.2) becomes

$$\frac{\mathrm{d}^3 N_d}{\mathrm{d}P_d^3} = \frac{S}{(2\pi)^3} \int \mathrm{d}^3 r_d \int \frac{\mathrm{d}^3 q\, \mathrm{d}^3 r}{(2\pi)^3} \mathcal{D}(\boldsymbol{r}, \boldsymbol{q}) W_{np} \left(\boldsymbol{p}_p, \boldsymbol{p}_n, \boldsymbol{r}_p, \boldsymbol{r}_n \right) \tag{5.5}$$

where

$$\mathcal{D}(\boldsymbol{r}, \boldsymbol{q}) = \int \mathrm{d}^3 \xi\, \mathrm{e}^{-\boldsymbol{q} \cdot \boldsymbol{\xi}} \varphi_d(\boldsymbol{r} + \boldsymbol{\xi}/2) \varphi_d^*(\boldsymbol{r} - \boldsymbol{\xi}/2) \tag{5.6}$$

is the Wigner function of the internal deuteron wave function.

The next task is to choose ansatz for the Wigner function, W_{np}, and the internal deuteron wave function, φ_d, such that equation (5.5) can be evaluated within the MC. Using a Gaussian ansatz for the deuteron wave function,

$$\varphi_d(\boldsymbol{r}) = \left(\pi d^2 \right)^{-3/4} \exp\left\{ -\frac{r^2}{2d^2} \right\}, \tag{5.7}$$

the deuteron Wigner function (5.6) becomes

$$\mathcal{D}(\boldsymbol{r}, \boldsymbol{q}) = 8\mathrm{e}^{-r^2/d^2} \mathrm{e}^{-q^2 d^2}. \tag{5.8}$$

The momentum distribution $G_{np}(\boldsymbol{p}_p, \boldsymbol{p}_n)$, which also includes relevant momentum correlations, can be obtained from the MC simulations. On the other hand, it can also be obtained from the two-particle Wigner function as

$$\int \mathrm{d}^3 r_p \, \mathrm{d}^3 r_n \, f^W_{np}(\boldsymbol{p}_n, \boldsymbol{p}_p, \boldsymbol{r}_n, \boldsymbol{r}_p) = N_p N_n |\psi_{np}(\boldsymbol{p}_n, \boldsymbol{p}_p)|^2 \equiv G_{np}(\boldsymbol{p}_n, \boldsymbol{p}_p), \tag{5.9}$$

where $\psi_{pn}(\boldsymbol{p}_n, \boldsymbol{p}_p)$ is the two-nucleon wave function in momentum space. Thus, it is convenient to assume a factorised form of the momentum and coordinate dependencies,

$$W_{np}(\boldsymbol{p}_n, \boldsymbol{p}_p, \boldsymbol{r}_n, \boldsymbol{r}_p) = H_{np}(\boldsymbol{r}_n, \boldsymbol{r}_p) G_{np}(\boldsymbol{p}_n, \boldsymbol{p}_p). \tag{5.10}$$

Note that this implies a transition from a full quantum mechanical treatment to a semi-classical picture. In turn, we neglect the spatial correlations between the nucleons, $H_{np}(\boldsymbol{r}_n, \boldsymbol{r}_p) = h(\boldsymbol{r}_n) h(\boldsymbol{r}_p)$, and choose a Gaussian ansatz for $h(\boldsymbol{r})$,

$$h(\boldsymbol{r}) = \left(2\pi\sigma^2\right)^{-3/2} \exp\left\{-\frac{r^2}{2\sigma^2}\right\}. \tag{5.11}$$

The interpretation of ansatz (5.7) is that the deuteron wave function is approximated as a Gaussian. This choice will be improved in section 5.1.6. The internal deuteron wave function reproduces the measured rms charge radius of $r_{\mathrm{rms}} = 1.89\,\mathrm{fm}$ [64] with $d = 3.2\,\mathrm{fm}$.[4] The interpretation of the spatial part of the nucleon Wigner functions (eq. (5.11)) includes the spatial distribution of the original particle reaction. This will be discussed in section 5.1.4.

If equations (5.8), (5.10) and (5.11) are inserted into equation (5.5), and the resulting Gaussian integrals are evaluated, the result becomes

$$\frac{\mathrm{d}^3 N_d}{\mathrm{d}P_d^3} = 8S \frac{\zeta}{(2\pi)^3} \int \frac{\mathrm{d}^3 q}{(2\pi)^3} \mathrm{e}^{-q^2 d^2} G_{np}(\boldsymbol{P}_d + \boldsymbol{q}, \boldsymbol{P}_d - \boldsymbol{q}), \tag{5.12}$$

where

$$\zeta \equiv \left(\frac{d^2}{d^2 + 4\sigma^2}\right)^{3/2} \leq 1 \tag{5.13}$$

is a factor that depends on the spatial spread of the nucleons and on the spatial extension of the deuteron wave function. Thus, we see that the coalescence probability is suppressed by both the spatial distribution through ζ and in momentum space by a Gaussian for large $q^2 d^2$.

---

[4] Note that the parameter r in the deuteron wave function describes the diameter and not the radius, such that $r_{\mathrm{rms}} = \int \mathrm{d}^3 r (r/2)^2 |\varphi(r)|^2$.

5.1.2 Spin and isospin factor

The proton and neutron form experimentally only one bound state: the deuteron. In this section, the statistical factor S will be derived. The nucleons are fermions and carries a total spin $s = 1/2$ and the spin in z-direction s_z can either be 'up' $(1/2)$ or 'down' $(-1/2)$. The spin basis of the nucleons can thus be expressed as the ket vectors $|1/2, 1/2\rangle$ and $|1/2, -1/2\rangle$. By using quantum mechanical addition of angular momentum one can show that the deuteron can be in four different spin states: one of the three spin triplet states[5]

$$|1\ 1\rangle = \left|\tfrac{1}{2}\ \tfrac{1}{2}\right\rangle \left|\tfrac{1}{2}\ \tfrac{1}{2}\right\rangle, \tag{5.14a}$$

$$|1\ 0\rangle = \frac{1}{\sqrt{2}} \left(\left|\tfrac{1}{2}\ \tfrac{1}{2}\right\rangle \left|\tfrac{1}{2}\ -\tfrac{1}{2}\right\rangle + \left|\tfrac{1}{2}\ -\tfrac{1}{2}\right\rangle \left|\tfrac{1}{2}\ \tfrac{1}{2}\right\rangle \right) \tag{5.14b}$$

$$|1\ -1\rangle = \left|\tfrac{1}{2}\ -\tfrac{1}{2}\right\rangle \left|\tfrac{1}{2}\ -\tfrac{1}{2}\right\rangle \tag{5.14c}$$

or the isosinglet state

$$|0\ 0\rangle = \frac{1}{\sqrt{2}} \left(\left|\tfrac{1}{2}\ \tfrac{1}{2}\right\rangle \left|\tfrac{1}{2}\ -\tfrac{1}{2}\right\rangle - \left|\tfrac{1}{2}\ -\tfrac{1}{2}\right\rangle \left|\tfrac{1}{2}\ \tfrac{1}{2}\right\rangle \right). \tag{5.14d}$$

The spin formalism can also be applied to the isospin quantum number discussed in section 3.2. The deuteron can thus be in four isospin states given by equation (5.14).

We can now compute the statistical isospin and spin factor by assuming that isospin is conserved. The Wigner-functions of the deuteron and nucleons used in last section did not contain any dynamical correlations regarding spin and isospin. We will follow Ref. [65] and use the statistical assumption that all deuteron states that are allowed from the Pauli exclusion principle have an equal weight. Moreover, it is assumed that the coalescence probability of the nucleons into a state of given total isospin is equal. Note, however, that there is no bound state of two protons or two neutrons [44]. Due to the SU(2) symmetry of the isospin, the last isotriplet (5.14b) cannot occur either. Thus, the deuteron has to be an isosinglet. This isosinglet state has four possible spin states. However, when regarding the proton and neutron as different states of the nucleon, the wave function has to be antisymmetric in the exchange of the particles. The symmetric spin singlet is thus expected to be suppressed. In total, the deuteron has in our statistical approximation $N_\mathrm{S} = 3$ possible spin and isospin states. The initial state on the other hand consists of one proton and one neutron, each of which has 2 possible spin states.[6] In addition, the statistical approximation assigns equal weight to the isospin singlet and

---

[5] A discussion of this can be found in most introductory text books on quantum mechanics or particle physics, such as Ref. [44].

[6] In the MC we distinguish between protons and neutrons. We therefore only consider initial states which contain one proton and one neutron.

the second isospin triplet, where only the singlet can occur. The final statistical factor thus becomes

$$S(d) = N_{\mathrm{S}}(d) \times \frac{1}{2^2} \times \frac{1}{2} = \frac{3}{8}. \tag{5.15}$$

5.1.3 Lorentz transformation

In the derivation of equation (5.12) all quantities and wave functions were evaluated in the rest frame of the deuteron. However, since current MC event generators do not model the space-time structure of the cascade, we want the spatial factor ζ to capture the hadronisation size $\Lambda_{\mathrm{QCD}} \sim 200\,\mathrm{MeV}$. One can achieve this by defining the Wigner functions of the nucleons (5.11) in the lab frame. It is thus natural that the size parameter σ is defined relative to the beam. In this section, the same derivation as before will be performed including the Lorentz transformation between the lab frame and the deuteron frame.[7] The important difference lies in which frame the different quantities are defined in equation (5.5). The right hand side of the equation can be evaluated in the deuteron frame. In this case, the integrations are performed in the deuteron frame. The Wigner function of the deuteron is defined in the deuteron frame, while the nucleon Wigner functions is defined in the lab frame. In summary, the evaluation of $\mathcal{D}(\boldsymbol{r}, \boldsymbol{q})$ remains unchanged and the arguments of H_{np} must be given in the lab frame. The momentum distribution $G_{np}(\boldsymbol{p}_n, \boldsymbol{p}_p)$ is simply evaluated in the deuteron frame by performing a Lorentz transformation of q within the MC and then normalising in the deuteron frame. Two different cases will be considered. In the first case, we consider σ as being independent of the beam direction, while in the second we split σ into a part parallel, $\sigma_{\parallel}$, and a part perpendicular, $\sigma_{\perp}$, to the original particle beam.

Parameter independent of beam direction

Assume first that σ is independent of the beam. Let $r_d^\mu = (t_d, \boldsymbol{r}_d)$, $r^\nu = (0, \boldsymbol{r})$ and $p_i^\mu = ([m^2 + \boldsymbol{q_i}^2]^{1/2}, \boldsymbol{q}_i)$ (with $\boldsymbol{q}_p = \boldsymbol{q}$, $\boldsymbol{q}_n = -\boldsymbol{q}$) be the space-time coordinate of the deuteron, the relative space-time coordinate of the nucleons and the four-momentum of nucleon i in the deuteron frame, respectively. Furthermore, let $r_d^{\mu\prime}$, $r^{\nu\prime}$ and $p_i^{\mu\prime}$ be the corresponding coordinates in the lab-frame. Only the components parallel to the direction of the deuteron momentum in the lab frame $\boldsymbol{P}_d$ will be influenced by the change of frame, and the spatial coordinates are thus split into a component parallel to $\boldsymbol{P}_d$, $x^{\boldsymbol{P}_d\parallel}$, and two components perpendicular to $\boldsymbol{P}_d$, $\boldsymbol{x}^{\boldsymbol{P}_d\perp}$. The multiplication of the h-functions gives a factor in the exponent on the form $r_p^2 + r_n^2 = (4r_d^2 + r^2)/2$. The relevant Lorentz

---

[7] A list of useful formula from special relativity used in this chapter can be found in appendix A.

transformations are thus

$$r'^{\mu} = \left(v\gamma r^{\boldsymbol{P}_d\parallel}, \gamma r^{\boldsymbol{P}_d\parallel}, \boldsymbol{r}^{\boldsymbol{P}_d\perp}\right), \tag{5.16a}$$

$$r'^{\mu}_d = \left(\gamma\left(t_\mathrm{f} + v r_d^{\boldsymbol{P}_d\parallel}\right), \gamma\left(r_d^{\boldsymbol{P}_d\parallel} + v t_\mathrm{f}\right), \boldsymbol{r}_d^{\boldsymbol{P}_d\perp}\right), \tag{5.16b}$$

where t_f is the deuteron freeze-out time. This leads to

$$r'^2 = r^{\boldsymbol{P}_d\perp 2} + \gamma^2 r^{\boldsymbol{P}_d\parallel 2}, \tag{5.17a}$$

$$r'^2_d = r_d^{\boldsymbol{P}_d\perp 2} + \gamma^2\left(r_d^{\boldsymbol{P}_d\parallel} + v t_d\right)^2. \tag{5.17b}$$

Equation (5.5) with the ansatz' (5.7) to (5.11) and the coordinate transformation (5.17) gives

$$\begin{aligned}\frac{\mathrm{d}^3 N_d}{\mathrm{d}P_d^3} &= 8S|\mathcal{N}|^2 \int \frac{\mathrm{d}^3 r_d\,\mathrm{d}^3 r\,\mathrm{d}^3 q}{(2\pi)^6} G_{np}(\boldsymbol{p}_n, \boldsymbol{p}_p) \\ &\times \exp\left\{-\frac{r^2}{d^2} - q^2 d^2 - \frac{r_d^{\boldsymbol{P}_d\perp 2} + \gamma^2\left(r_d^{\boldsymbol{P}_d\parallel} + v t_d\right)^2}{\sigma^2} - \frac{r^{\boldsymbol{P}_d\perp 2} + \gamma^2 r^{\boldsymbol{P}_d\parallel 2}}{4\sigma^2}\right\},\end{aligned} \tag{5.18}$$

where $|\mathcal{N}|^2$ is fixed by the normalisation condition of the Wigner function.

The Wigner function must be normalised such that $G_{np}(\boldsymbol{p}_n, \boldsymbol{p}_p)$ can be interpreted as the probability distribution in momentum space in the deuteron frame. In other words, we require that

$$\begin{aligned}G_{np}(\boldsymbol{p}_n, \boldsymbol{p}_p) &= |\mathcal{N}|^2 \int \mathrm{d}^3 r_p\,\mathrm{d}^3 r_n\, W_{np}(\boldsymbol{p}_n, \boldsymbol{p}_p, \boldsymbol{r}'_n, \boldsymbol{r}'_p) \\ &= |\mathcal{N}|^2 \int \mathrm{d}^3 r\,\mathrm{d}^3 r_d\, G_{np}(\boldsymbol{p}_n, \boldsymbol{p}_p) \exp\left\{-\frac{r_d^{\boldsymbol{P}_d\perp 2} + \gamma^2\left(r_d^{\boldsymbol{P}_d\parallel} + v t_d\right)^2}{\sigma^2} - \frac{r^{\boldsymbol{P}_d\perp 2} + \gamma^2 r^{\boldsymbol{P}_d\parallel 2}}{4\sigma^2}\right\},\end{aligned} \tag{5.19}$$

where $\boldsymbol{r}'_i$ is the position of the nucleons in the lab frame. The r_d integral in (5.18) is cancelled by $|\mathcal{N}|^2$ and the only thing left to consider is therefore the r-integrals. The differential is split as $\mathrm{d}^3 r = \mathrm{d}r^{\boldsymbol{P}_d\parallel}\,\mathrm{d}^2 r^{\boldsymbol{P}_d\perp}$, and the corresponding integrands are Gaussians and thus trivial to evaluate. The final result can be written on the same form as equation (5.12) with

$$\zeta = \frac{d^2}{d^2 + 4\sigma^2}\sqrt{\frac{d^2}{d^2 + 4\sigma^2/\gamma^2}}. \tag{5.20}$$

One can thus see that the effect of the Lorentz transformation in this case is the same as a Lorentz contraction of the size parameter σ in the direction parallel to the deuteron momentum. Equation (5.20) reduces to (5.13) in the limit of low deuteron velocities. This is expected to be a good approximation at low transverse momenta to the more complicated case discussed next.

Parameter dependent on beam direction

Consider now the case where the size parameter σ is split as $\sigma_\perp \neq \sigma_\parallel$. The general procedure is similar as in the previous case, but is more technically difficult since $\sigma_\perp$ and $\sigma_\parallel$ are defined relative to the original particle beam, as shown in figure 5.1. The ansatz for $h(\boldsymbol{r})$ should therefore in this case be

$$h(\boldsymbol{r}) \propto \exp\left(-\frac{r_\parallel^2}{2\sigma_\parallel^2} - \frac{r_\perp^2}{2\sigma_\perp^2}\right), \tag{5.21}$$

where the subscripts indicates whether the quantity is defined perpendicular or parallel to the particle beam. Furthermore, the components of $\boldsymbol{r}_{i\perp}$ and $\boldsymbol{r}_{i\parallel}$ parallel to the deuteron momentum will be affected by the transformation between the Lorentz frames, while the components perpendicular to the deuteron momentum will not. This means that we also have to split both $\boldsymbol{r}_{i\perp}$ and $\boldsymbol{r}_{i\parallel}$ into components parallel and perpendicular to $\boldsymbol{P}_d$.

The product of the two h-functions will now contain terms proportional to $r_{p\parallel}^2 + r_{n\parallel}^2$ and $r_{p\perp}^2 + r_{n\perp}^2$ in the exponent. The parallel term can be written as $r_{p\parallel}^2 + r_{n\parallel}^2 = (4r_{d\parallel}^2 + r_\parallel^2)/2$ and similar for the perpendicular term. As in the previous case, the r_d-integral will be cancelled by the r_d-integral in the normalisation of the Wigner function and can therefore be disregarded. Inserting equation (5.21) into equation (5.2) and disregarding the r_d-integral yields

$$\frac{\mathrm{d}^3 N_d}{\mathrm{d}P_d^3} = 3S|\mathcal{N}|^2 \int \frac{\mathrm{d}^3 r\, \mathrm{d}^3 q}{(2\pi)^6} G_{np}(\boldsymbol{p}_n, \boldsymbol{p}_p) \exp\left\{-\frac{r^2}{d^2} - q^2 d^2 - \frac{1}{4\sigma_\parallel^2} {r'_\parallel}^2 - \frac{1}{4\sigma_\perp^2} {r'_\perp}^2\right\}, \tag{5.22}$$

where $|\mathcal{N}|^2$ is fixed by the normalisation condition

$$G_{np}(\boldsymbol{p}_n, \boldsymbol{p}_p) = |\mathcal{N}|^2 \int \mathrm{d}^3 r\, G_{np}(\boldsymbol{p}_n, \boldsymbol{p}_p) \exp\left\{-\frac{r^{\boldsymbol{P}_d\perp\prime 2} + \gamma^2 r^{\boldsymbol{P}_d\parallel\prime 2}}{4\sigma^2}\right\}, \tag{5.23}$$

and the primed coordinates are defined in the lab frame. By considering the setup in figure 5.1 and using the transformation (5.16b) one obtains

$$r_\perp^{\boldsymbol{P}_d\perp\prime} = r'_\perp \cos(\theta) = r_\perp^{\boldsymbol{P}_d\perp}, \tag{5.24a}$$

$$r_\perp^{\boldsymbol{P}_d\parallel\prime} = r'_\perp \sin(\theta) = \gamma r_\perp^{\boldsymbol{P}_d\parallel}, \tag{5.24b}$$

$$r_\parallel^{\boldsymbol{P}_d\perp\prime} = r'_\parallel \sin(\theta) = r_\parallel^{\boldsymbol{P}_d\perp}, \tag{5.24c}$$

$$r_\parallel^{\boldsymbol{P}_d\parallel\prime} = r'_\parallel \cos(\theta) = \gamma r_\parallel^{\boldsymbol{P}_d\parallel}, \tag{5.24d}$$

where θ and the primed quantities are defined in the lab-frame. This leads in turn to

$${r'_\perp}^2 = {r_\perp^{\boldsymbol{P}_d\perp}}^2 + \gamma^2 {r_\perp^{\boldsymbol{P}_d\parallel}}^2, \tag{5.25a}$$

$${r'_\parallel}^2 = {r_\parallel^{\boldsymbol{P}_d\perp}}^2 + \gamma^2 {r_\parallel^{\boldsymbol{P}_d\parallel}}^2. \tag{5.25b}$$

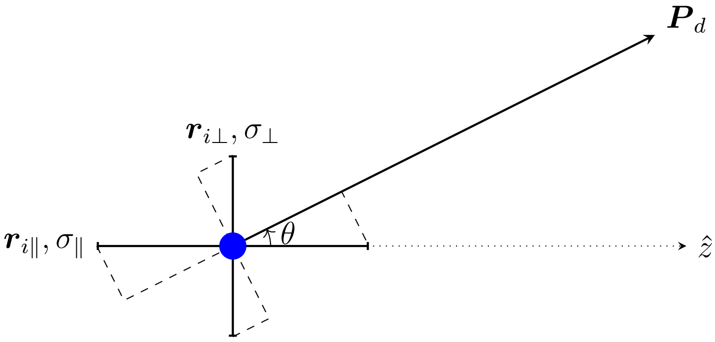

Figure 5.1: The size parameter σ is split into a part parallel to the beam (z-axis), $\sigma_\parallel$, and a part perpendicular to the beam, $\sigma_\perp$. Only the components of $\boldsymbol{r}_\perp$ and $\boldsymbol{r}_\parallel$ parallel to the deuteron momentum $\boldsymbol{P}_d$ is affected by the Lorentz transformation. This transformation will lead to different effective transformation of $\sigma_\parallel$ and $\sigma_\perp$ that depends on the angle θ between the beam and $\boldsymbol{P}_d$.

As before, the differential for the r-integral can be split as $\mathrm{d}^3 r = \mathrm{d}r^{\boldsymbol{P}_d \parallel}\, \mathrm{d}^2 r^{\boldsymbol{P}_d \perp}$, and when the transformations (5.24) and (5.25) are inserted, the integrands becomes Gaussians. The final result can again be written as equation (5.12), but this time with the spatial factor

$$\zeta = \frac{d^2}{d^2 + 4\tilde{\sigma}_\perp^2} \sqrt{\frac{d^2}{d^2 + 4\tilde{\sigma}_\parallel^2}}, \tag{5.26}$$

where the effective transformation of the size parameters, $\tilde{\sigma}_\perp$ and $\tilde{\sigma}_\parallel$, are given by

$$\tilde{\sigma}_\parallel = \frac{\sigma_\parallel}{\sqrt{\sin^2\theta + \gamma^2 \cos^2\theta}}, \tag{5.27a}$$

$$\tilde{\sigma}_\perp = \frac{\sigma_\perp}{\sqrt{\cos^2\theta + \gamma^2 \sin^2\theta}}. \tag{5.27b}$$

This reduces to (5.20) in the limit $\theta \to 0$, which is the same limit as a small transverse momentum, and corresponds to a case where only $\sigma_\parallel$ is affected by the Lorentz transformation.

Lorentz transformation back to the lab frame

The right hand side of equation (5.5) in the discussions above was evaluated in deuteron frame. The only things left to consider is the transformation back to the lab frame. After evaluation, the only variable left that is not Lorentz invariant is $\boldsymbol{P}_d$ on the left hand side. Consider a coordinate system in which the x-axis points along $\boldsymbol{P}_d$. Only the x-component of the momentum is affected. From the Lorentz invariant quantity $\mathrm{d}P_d^x/E$ we obtain

$$\mathrm{d}P_d^x = \mathrm{d}P_d^{x\prime}\,\frac{E'}{E} = \frac{1}{\gamma}\,\mathrm{d}P_d^{x\prime} \tag{5.28}$$

where the primed quantities are in the lab frame. In conclusion, the right hand of side equation (5.12) must thus be multiplied by a factor $1/\gamma$.

5.1.4 Parameter estimation and interpretation

The $\sigma_\perp$ and $\sigma_\parallel$ parameters can have two different interpretation: in the CoM frame they describe the nucleon radius, while in the lab frame they describe the characteristic spread of the hadronisation. In this subsection, we will use these interpretations to estimate the parameters $\sigma_\parallel$ and $\sigma_\perp$ in different scattering processes. Due to the simplifications used in the derivation of the model, uncertainties in the event generator and the simplifications used in this section, the final model has some degree of freedom that must be tuned to experimental data. Nevertheless, we can get an estimate the expected parameters for different processes.

Consider first the case of e^+e^- annihilation into nucleons in the CoM frame of the collision. Let the z-axis be directed along the direction of the outgoing quark and anti-quark from the hard process $e^+e^- \to \bar{q}q$ and consider first the spread in the longitudinal direction. The coalescence process will involve nucleons that have nearly completed their formation, and the process will thus proceed on distance scales comparable to the hadronisation length $L_{\text{had}} \sim \gamma R_{\text{had}}$ from non-perturbative QCD, as discussed in section 3.4.4. For protons and neutrons $R_{\text{had}} = R_p \sim 1\,\text{fm}$. Boosting to the rest-frame of the deuteron should compensate the gamma factor. Thus, one will expect that $\sigma_\parallel \sim R_{\text{had}} \sim 1\,\text{fm} \approx 5\,\text{GeV}^{-1}$. On the other hand, the characteristic spread of the nucleon in the transverse direction is related to Λ_{QCD} via the uncertainty relation. That is, the spread in the transverse direction is due to the random walk behaviour of previous generations of parton branchings that each contributes by the inverse of the transverse momentum of the parton, $\Delta b_i \sim 1/p_\perp$. As in the longitudinal case, the main contribution is from non-perturbative physics with $p_\perp \sim \Lambda_{\text{QCD}}$. This yields $\sigma_\perp \sim \Lambda_{\text{QCD}}$, which is on the same order of magnitude as $\sigma_\parallel$. We therefore let $\sigma_\perp = \sigma_\parallel \equiv \sigma$ to minimise the number of free parameters. Since the bulk of produced deuterons has a relatively small transverse momentum, one may expect that the Lorentz transformation to the deuteron frame has only a small effect on $\sigma_\perp$. A setup taking this boost into account will improve the fit to experimental data at large p_T, and be discussed below.

Now we turn to hadron-hadron collisions. In this case, the scattering process is influenced strongly by multiple scatterings. That is, the nucleons involved in the coalescence process can in general originate from different non-perturbative parton-parton interactions. This induces an additional geometrical contribution from the parton clouds to the spread that will lower the probability of coalescence. Starting with the longitudinal spread, it is important to include the effect of different Lorentz contractions of the parton clouds for fast and slow partons. The partons in for example the projectile hadron in the lab frame are distributed over the longitudinal distance $L \sim R_p/\gamma \approx R_p e^{-y}$, where y is the rapidity of the beam in the lab frame. This Lorentz contraction is again compensated by the transformation to the deuteron frame.[8] Hence, the resulting geometrical contribution from the extension of the parton cloud to $\sigma_\parallel$ is $\sigma_{\parallel(\text{geom})} \sim R_p \sim 1\,\text{fm}$ for proton proton collisions. The final spread in the longitudinal direction is obtained by summing the contributions in quadrature,

$$\sigma_\parallel^2 = \sigma_{\parallel(e^\pm)}^2 + \sigma_{\parallel(\text{geom})}^2. \tag{5.29}$$

Finally, we must the geometrical contribution to $\sigma_\perp$, which will be done using the simple geometrical picture in figure 5.2. Naively, one would expect that the final contribution depends on the impact parameter, but as we will see, this is fortunately not the case. The geometrical contribution will be defined as the spread of the overlapping region (O) of the parton clouds,

$$\sigma_{\perp(\text{geom})}^2 = \langle r_1^2 \rangle_O - \langle \boldsymbol{r}_1 \rangle_O^2. \tag{5.30}$$

The expectation value $\langle A \rangle_O$ will be defined as

$$\langle A \rangle = \frac{\int \mathrm{d}^2 r_1\, \mathrm{d}^2 r_2\, A \rho_1(r_1) \rho_2(r_2) w_\text{int}(|\boldsymbol{b} - \boldsymbol{r}_1 - \boldsymbol{r}_2|)}{\int \mathrm{d}^2 r_1\, \mathrm{d}^2 r_2\, \rho_1(r_1) \rho_2(r_2) w_\text{int}(|\boldsymbol{b} - \boldsymbol{r}_1 - \boldsymbol{r}_2|)}, \tag{5.31}$$

where $\boldsymbol{b}$ is the impact parameter of the collision, $\rho_i(r_i)$ is the parton density distribution of hadron i in the transverse direction, and w_int is the probability for a parton-parton interaction. For simplicity, the radius of the parton-parton interactions is neglected such that

$$w_\text{int}(|\boldsymbol{b} - \boldsymbol{r}_1 - \boldsymbol{r}_2|) = \delta^{(2)}(\boldsymbol{b} - \boldsymbol{r}_1 - \boldsymbol{r}_2). \tag{5.32}$$

Moreover, the density distributions are approximated as the Gaussians

$$\rho_i = 1/(2\pi\sigma_\perp^2) \exp\left\{-r^2/2R_i^2\right\}, \tag{5.33}$$

where R_i is the transverse radius of hadron i, and must be chosen such that it reproduces the correct rms radius. With the chosen simplifications and geometrical picture, one obtains

$$\sigma_{\perp(\text{geom})}^2 = \frac{2R_1^2 R_2^2}{R_1^2 + R_2^2}. \tag{5.34}$$

Notice that the dependence on the impact parameter has vanished. In the particular case of *pp* collisions, equation (5.34) becomes $\sigma_{\perp(\text{geom})} \sim R_p$. Again, the contributions can be added in quadrature.

---

[8] This argument is a bit superficial, but remember it's only an estimate of the parameters. The gamma-factor in the Lorentz contraction of the parton cloud is not the same as for the boost to the deuteron frame, but one can think of the geometrical spread as the spread in the partons that at the end will constitute the nucleons and the deuteron.

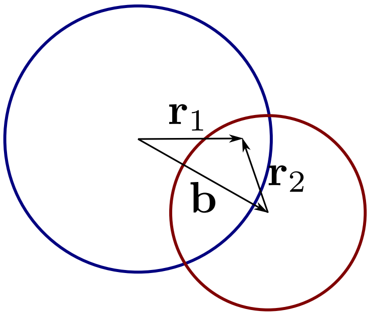

Figure 5.2: Schematics of the parton clouds of two interacting hadrons.

In conclusion, we have shown that $\sigma_\parallel \sim \sigma_\perp$ and

$$\sigma^2 = \sigma^2_{(e^\pm)} + \sigma^2_{(\text{geom})} \approx 2\sigma^2_{(e^\pm)} \sim 2(5\,\text{GeV}^{-1})^2. \tag{5.35}$$

This describes both a relationship between the coalescence probability in e^+e^- annihilations and pp collisions, as well as the expected numerical value of the parameters.

Finally, in an alternative setup we define the parameter $\sigma_\perp$ in the lab frame in order to improve the fit to experimental data at large p_T, as discussed above. From equation (5.26) it is clear that we obtain

$$\zeta = \frac{d^2}{d^2 + 4\tilde{\sigma}_\perp^2}\sqrt{\frac{d^2}{d^2 + 4\sigma_\parallel}}, \tag{5.36}$$

where $\tilde{\sigma}_\perp$ is given by equation (5.27b). In other words, the nucleon Wigner function is defined in the lab frame, but the resulting Lorentz transformation in the direction parallel to the particle beam is approximately cancelled by the transformation of the hadronisation size.

For completeness, consider now the geometrical contribution in hadron-nucleus collisions. The geometrical contribution in the longitudinal direction is $\sigma_{\parallel(\text{geom})} \sim R_{\text{Pb}}$. The parton distribution in the nuclear target N is dominated by the nuclear wave function. For a sufficiently heavy nucleus, such as lead, the density may be approximated as constant for $b < R_N$. This heavy nucleus approximation yields $\sigma^2_{\perp(\text{geom})} \simeq =2R_h^2$. Thus, the universality of equation (5.35) is lost.

5.1.5 Model and numerical procedure

Everything is now set to write down a new coalescence model that is evaluated per-event within the MC. The final result from the previous sections, including the statistical factor $S = 3/8$, is that the deuteron yield in the lab frame can be written as

$$\frac{\mathrm{d}^3 N_d}{\mathrm{d}P_d^3} = \frac{1}{\gamma}\frac{3\zeta}{(2\pi)^3}\int \frac{\mathrm{d}^3 q}{(2\pi)^3}\mathrm{e}^{-q^2 d^2} G_{np}(\boldsymbol{q}, -\boldsymbol{q}), \tag{5.37}$$

where $d = 3.2\,\mathrm{fm}$. The integral must be evaluated in the deuteron frame and the momentum distributions $G_{np}(\boldsymbol{q}, -\boldsymbol{q})$ is obtained from the event generator. Several different spatial distribution factors ζ have been considered: a simple constant (eq. (5.13)), one including boost in the direction of the deuteron momentum (eq. (5.20)), one including a general boost (eq. (5.26)), and finally one including a general boost and account for the boost of the hadronisation size (eq. (5.36)).

The physical interpretation of the quantity q is the momentum of the nucleons in the deuteron frame. In the coalescence model discussed in section 4.1.2 all proton-neutron pairs with $2q < p_0$ forms a deuteron. The new model is, opposed to the old model, probabilistic. The probability that a given proton and neutron coalesce is proportional to $\exp(-q^2 d^2)$. This can be taken into account by adding weights to the binning procedure when computing the energy spectrum. In this case, all of the information that can be extracted from each event is used. The weights become apparent when (5.37) is written on the discrete form

$$\frac{\Delta N_d}{\Delta P_d^x \Delta P_d^y \Delta P_d^z} = \frac{3\zeta}{\gamma} \sum_{\boldsymbol{q}} \mathrm{e}^{-q^2 d^2} \Delta N_p(\boldsymbol{q}) \Delta N_n(\boldsymbol{q}). \tag{5.38}$$

Thus, the weight from a proton-neutron pair,

$$w = 3\zeta e^{-q^2 d^2}, \tag{5.39}$$

must be used as weight in the binning procedure when computing the deuteron yield. Note that the gamma-factor is not needed since we perform the binning in the lab frame, but q is still defined in the deuteron frame.

At this point, one must take some care about potential multiple counting, since there is a possibility of having more than one proton-neutron pair being able to coalesce. In this case, one should in principle use the projection of the deuteron density matrix onto an n-nucleon state as starting point (see e.g. Ref. [65]). However, it should be sufficient to only consider one pair at a time and set the weights accordingly. Assume that for a given event the final state contains N_p protons and N_n neutrons. Denoting the coalescence probability, equation (5.39), of a given proton-neutron pair ij as w_{ij}, the average number of deuterons produced can be written as

$$\begin{aligned} N_d &= \sum_{i=1}^{N_p} \sum_{j=1}^{N_n} w_{ij} - \frac{1}{2} \sum_{i=1}^{N_p} \sum_{k\neq i}^{N_p} \sum_{j=1}^{N_n} w_{ij}\, w_{kj} - \frac{1}{2} \sum_{i=1}^{N_p} \sum_{j=1}^{N_n} \sum_{l\neq j}^{N_n} w_{ij}\, w_{il} - \dots \\ &\simeq \sum_{i=1}^{N_p} \sum_{j=1}^{N_n} w_{ij} \left[1 - \frac{1}{2} \sum_{k\neq i}^{N_p} w_{kj} - \frac{1}{2} \sum_{l\neq j}^{N_n} w_{il} \right], \end{aligned} \tag{5.40}$$

where in the second line triple and higher counts could be neglected due to the smallness of the coalescence probabilities. Thus, a proton-neutron pair ij should contribute with a weight

$$\Omega_{ij} = w_{ij}\left[1-\frac{1}{2}\sum_{k\neq i}^{N_p} w_{kj} - \frac{1}{2}\sum_{l\neq j}^{N_n} w_{il}\right], \tag{5.41}$$

where ω_{ij} is given by equation (5.39).[9]

5.1.6 Improving the deuteron wave function

In the above treatment a Gaussian with the correct r_{rms}-value was used as an ansatz for the deuteron wave function. However, it would be favourable to instead use a wave function that gives physically a better picture of the deuteron. One possibility is to use the Hulthen wave function,

$$\phi_d(\boldsymbol{r}) = \sqrt{\frac{\alpha\beta(\alpha+\beta)}{2\pi(\alpha-\beta)^2}}\,\frac{\mathrm{e}^{-\alpha r}-\mathrm{e}^{-\beta r}}{r}, \tag{5.42}$$

with $\alpha = 0.23\,\mathrm{fm}^{-1}$ and $\beta = 1.61\,\mathrm{fm}^{-1}$, which gives a good description of the deuteron ground state [55, 64]. Unfortunately, this requires a more complicated numerical treatment.

To obtain a better description of the deuteron, and at the same time keep the problem analytical solvable, one can use the sum of two Gaussians as the deuteron probability distribution,

$$|\varphi_d(\boldsymbol{r})|^2 = \pi^{-3/2}\left[\frac{\Delta}{d_1^3}\mathrm{e}^{-r^2/d_1^2} + \frac{1-\Delta}{d_2^3}\mathrm{e}^{-r^2/d_2^2}\right], \tag{5.43}$$

which must be fitted to the Hulthen wave function (5.42) in order to fix Δ, d_1 and d_2. The probability distribution (5.43) can be obtained from the wave function

$$\varphi_d(\boldsymbol{r}) = \pi^{-3/4}\left(\mathrm{i}\sqrt{\frac{\Delta}{d_1^3}}\mathrm{e}^{-r^2/2d_1^2} + \sqrt{\frac{1-\Delta}{d_2^3}}\mathrm{e}^{-r^2/2d_2^2}\right). \tag{5.44}$$

Inserting this into the definition of the deuteron Wigner function (5.7) yields

$$\mathcal{D}(\boldsymbol{r},\boldsymbol{q}) = 8\left[\Delta\mathrm{e}^{-r^2/d_1^2}\mathrm{e}^{-q^2d_1^2} + (1-\Delta)\mathrm{e}^{-r^2/d_2^2}\mathrm{e}^{-q^2d_2^2}\right] - A(\boldsymbol{r},\boldsymbol{q}), \tag{5.45}$$

where

$$A(\boldsymbol{r},\boldsymbol{q}) = 16\sqrt{\frac{\Delta(1-\Delta)}{d_2^3d_1^3}}\exp\left\{\left(-a+\frac{b^2}{a}\right)r^2 - \frac{q^2}{a}\right\}\sin\left(\frac{2b}{a}\boldsymbol{r}\cdot\boldsymbol{q}\right), \tag{5.46}$$

---

[9] We have performed the fits both with and without the double counting, and it turns out that double counting can be neglected in all cases due to the Gaussian suppression of large q. The largest contribution to the double counting occurs with the two-Gaussian φ_0-fit deuteron wave function discussed in the next subsection.

with $a = 1/2d_1^2 + 1/2d_2^2$ and $b = 1/2d_1^2 - 1/2d_2^2$.[10] Since the nucleon Wigner functions are symmetric, the cross term do not contribute when performing the r-integration in equation (5.5). The weights in the binning procedure in the two-Gaussian case are thus

$$w = 3\left(\zeta_1 \Delta e^{-q^2 d_1^2} + \zeta_2 [1-\Delta] e^{-q^2 d_2^2}\right), \tag{5.47}$$

where ζ_i is given by equation (5.13).

Two possible methods are to fit to either $|\varphi_d(0)|^2$, $\langle r \rangle$ and $\langle r^2 \rangle$, or $\langle r \rangle$, $\langle r^2 \rangle$ and $\langle r^3 \rangle$. The first method will be called φ_0-fit and the second r^3-fit. The φ_0-fit yields $\Delta = 0.581$ $d_1 = 3.979\,\text{fm}$ and $d_2 = 0.890\,\text{fm}$, while the r^3-fit yields $\Delta = 0.247$, $d_1 = 5.343\,\text{fm}$ and $d_2 = 1.810\,\text{fm}$. These are plotted in figure 5.3 together with the probability distributions from the one-Gaussian (5.7) and Hulthen (5.42) wave functions. From the plot, one can see that the two-Gaussian case reproduces the Hulthen probability distribution better than the one-Gaussian case. In particular, the Hulthen wave function is more peaked around $r = 0$ than the Gaussian wave function. The φ_0-fit reproduces visually the behaviour around $r = 0$ best and may therefore be expected to give the best fit to experiments later on. The average of the two probability distributions will give even better visual fit to the Hulthen wave function, and will also be considered.

The weighted q^2 distribution with the one-Gaussian weight and two-Gaussian weights resulting from pp collisions at $\sqrt{s} = 7\,\text{TeV}$ is shown in figure 5.4. The distribution resulting from the old coalescence model is plotted for comparison. From the plot, one can see that the effect of adding a Gaussian that describes the peak at $r = 0$ in the probability distribution leads to an increased contribution from large q.

Note that the original approximation that the two nucleons and deuteron are in the same Lorentz frame does not hold for large q. In these cases, a relativistic derivation is needed. However, one can treat problem by adding a cut-off as done here. In the simulations that will be performed in section 5.3, all pairs with $q < 0.25\,\text{GeV}$ is stored for the one-Gaussian case and $q < 0.5\,\text{GeV}$ for the two-Gaussian cases.

5.2 Coalescence of helium-3 and tritium

5.2.1 Derivation

The case of the helium-3 nucleus and tritium are similar to the case of deuteron, but the derivation is more cumbersome. The Coulomb interaction between the two protons in the helium nucleus is neglected such that the model for helium-3 and tritium becomes the same. This assumption is supported by ALICE experiment, which found a comparable

---

[10] If one does not include the imaginary unit for one of the Gaussians in (5.44), the cross term becomes symmetric. Reference [65] discusses this for the sum of 15 Gaussians. This is the reason why we only include two Gaussians.

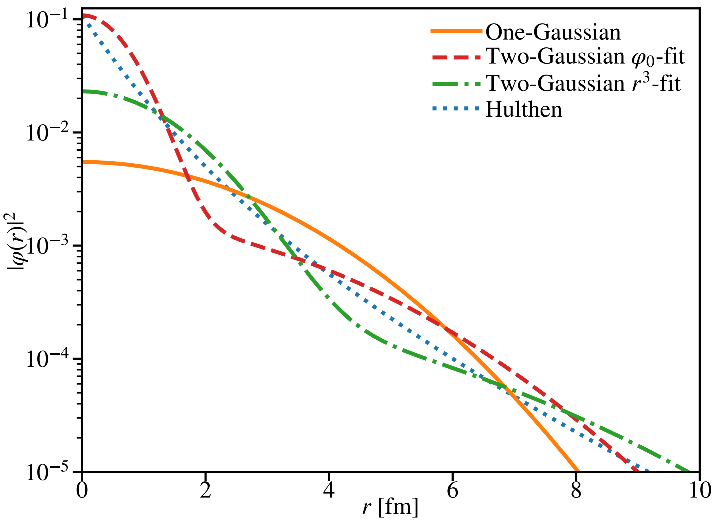

Figure 5.3: Comparison between the different ansatz used on the deuteron wave function.

yield of helium-3 and tritium nuclei in pp collisions. The binding energies of the two nuclei are still considered low ($\sim 8\,\mathrm{MeV}$), and the same approximations as in the deuteron case still apply.

The number of helium nuclei with momentum $\boldsymbol{P}_{\mathrm{He}}$ is found by projecting the helium state onto the tree-nucleon state, which gives an expression identical to equation (5.1). As in the deuteron case, the nucleus wave function is factorised into a plane wave describing the CoM motion with momentum $\boldsymbol{P}_{\mathrm{He}}$ and an internal wave function:

$$\phi_{\mathrm{He}}(\boldsymbol{x}_1, \boldsymbol{x}_2, \boldsymbol{x}_3) = (2\pi)^{-3/2} \exp\left[\mathrm{i}\boldsymbol{P}_{\mathrm{He}} \cdot (\boldsymbol{x}_1 + \boldsymbol{x}_2 + \boldsymbol{x}_3)/3\right] \varphi(\boldsymbol{x}_1, \boldsymbol{x}_2, \boldsymbol{x}_3). \tag{5.48}$$

It is convenient to introduce the CoM coordinates[11]

$$\boldsymbol{\lambda} = (\boldsymbol{x}_1 + \boldsymbol{x}_2 - 2\boldsymbol{x}_3)/\sqrt{6}, \tag{5.49a}$$

$$\boldsymbol{\rho} = (\boldsymbol{x}_1 - \boldsymbol{x}_2)/\sqrt{2}, \tag{5.49b}$$

$$\boldsymbol{R} = (\boldsymbol{x}_1 + \boldsymbol{x}_2 + \boldsymbol{x}_3)/3, \tag{5.49c}$$

with $\boldsymbol{x}_1^2 + \boldsymbol{x}_2^2 + \boldsymbol{x}_3^2 = 3\boldsymbol{R}^2 + \boldsymbol{\rho}^2 + \boldsymbol{\lambda}^2$, $\boldsymbol{\rho}^2 + \boldsymbol{\lambda}^2 = (\boldsymbol{x}_1 - \boldsymbol{x}_2)^2 + (\boldsymbol{x}_1 - \boldsymbol{x}_3)^2 + (\boldsymbol{x}_3 - \boldsymbol{x}_2)^2$ and $\mathrm{d}^3 r_1\, \mathrm{d}^3 r_2\, \mathrm{d}^3 r_3 = 3^{3/2}\, \mathrm{d}^3 R\, \mathrm{d}^3 \rho\, \mathrm{d}^3 \lambda$ with $r_i \equiv (x_i + x_i')/2$. The internal wave function is as before approximated by a Gaussian in the relative coordinates as

$$\varphi(\boldsymbol{x}_1, \boldsymbol{x}_2, \boldsymbol{x}_3) = (3\pi^2 d^4)^{-3/4} \exp\left(-\frac{\boldsymbol{\rho}^2 + \boldsymbol{\lambda}^2}{2b^2}\right), \tag{5.50}$$

---

[11] This choice was motivated by discussions in [55] regarding a the coalescence of helium-3 in heavy ion collisions.

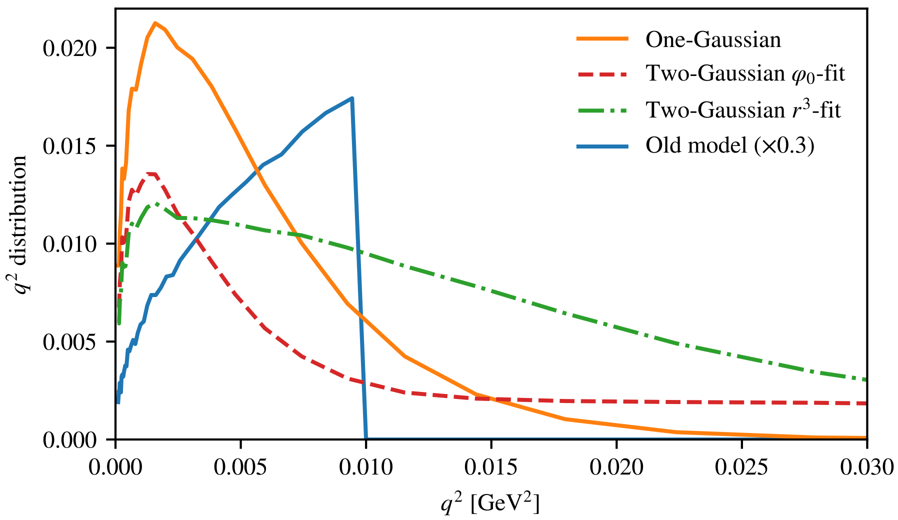

Figure 5.4: Weighted q distribution for the considered models. The simulation is run with the $\sqrt{s} = 7\,\text{TeV}$ ALICE setup with the parameter $\sigma = 7\,\text{GeV}^{-1}$ and a constant ζ. For the old model, $p_0 = 0.2\,\text{GeV}$ is used. The distribution from the old model is multiplied by a factor 0.3 to make the figure clearer.

with b being the size parameter of the nucleus, which incidentally is identical to the rms radius of the nucleus,

$$r_{\text{rms}} = \int 3^{3/2} \mathrm{d}^3\rho\, \mathrm{d}^3\lambda\, \frac{\rho^2 + \lambda^2}{3} |\varphi(\boldsymbol{x}_1, \boldsymbol{x}_2, \boldsymbol{x}_3)|^2 = b^2. \tag{5.51}$$

The ^{3}He and ^{3}H nuclei have rms radii 1.96 fm and 1.76 fm, respectively [66].

Performing the same steps as in equations (5.2) and (5.4), the momentum spectrum of the produced nuclei spectrum can be written as

$$\begin{aligned}\frac{\mathrm{d}^3 N_{\text{He}}}{\mathrm{d}P_{\text{He}}^3} = {} & \frac{S}{(2\pi)^3} \int 3^3 \mathrm{d}^3R \mathrm{d}^3\rho \mathrm{d}^3\lambda\, \mathrm{d}^3R'\, \mathrm{d}^3\rho'\, \mathrm{d}^3\lambda'\, (2\pi)^{-3}\, \mathrm{e}^{-\mathrm{i}\boldsymbol{P}_{\text{He}}\cdot(\boldsymbol{R}-\boldsymbol{R}')}\, \varphi_{\text{He}}(\boldsymbol{\rho}, \boldsymbol{\lambda})^*\, \varphi_{\text{He}}(\boldsymbol{\rho}', \boldsymbol{\lambda}') \\ & \times \int \frac{\mathrm{d}^3p_1}{(2\pi)^3} \frac{\mathrm{d}^3p_2}{(2\pi)^3} \frac{\mathrm{d}^3p_3}{(2\pi)^3}\, \mathrm{e}^{\mathrm{i}\boldsymbol{p}_1\cdot(\boldsymbol{x}_1-\boldsymbol{x}_1')+\mathrm{i}\boldsymbol{p}_2\cdot(\boldsymbol{x}_2-\boldsymbol{x}_2')+\mathrm{i}\boldsymbol{p}_3\cdot(\boldsymbol{x}_3-\boldsymbol{x}_3')} \\ & \times W_{N_1N_1N_3}\left(\boldsymbol{p}_1, \boldsymbol{p}_2, \boldsymbol{p}_3, \frac{\boldsymbol{x}_1+\boldsymbol{x}_1'}{2}, \frac{\boldsymbol{x}_2+\boldsymbol{x}_2'}{2}, \frac{\boldsymbol{x}_3+\boldsymbol{x}_3'}{2}\right),\end{aligned} \tag{5.52}$$

where S is the statistical factor accounting for different isospin and spin state, p_i is the momentum of nucleon i and $W_{N_1N_1N_3}$ is the Wigner function of the three nucleon state. Once again, we approximate $W_{N_1N_1N_3}$ by the product of the momentum and coordinate distributions of the nucleons, and neglect the correlations between the coordinate distributions which we approximate as Gaussians. That is,

$$W_{N_1N_2N_3}(\boldsymbol{p}_1,\boldsymbol{p}_2,\boldsymbol{p}_3,\boldsymbol{r}_1,\boldsymbol{r}_2,\boldsymbol{r}_3)=G_{N_1N_2N_3}(\boldsymbol{p}_1,\boldsymbol{p}_2,\boldsymbol{p}_3)\prod_{i=1}^{3}h(\boldsymbol{r}_i), \tag{5.53}$$

where $h(\boldsymbol{r})$ is given by equation (5.11).

The integral in equation (5.52) is cumbersome, but can be evaluated straight forwardly using the coordinates (5.49). The CoM coordinates in the exponent due to the three h-functions are completely decoupled.[12] The integrals over R and R' then lead to a factor $8^{-1}(2\pi)^3(8\pi\sigma^2/3)^{3/2}$ and a δ-function which takes care of momentum conservation. The p_1-integral then becomes trivial and the rest of the integrals can be evaluated as Gaussians. At the end, $\boldsymbol{P}_{\mathrm{He}}$ is set to zero as the expression is to be evaluated in the nucleus frame. The result is

$$\frac{\mathrm{d}^3N_{\mathrm{He}}}{\mathrm{d}P^3_{\mathrm{He}}}=\frac{64s\zeta}{(2\pi)^3}\int\frac{\mathrm{d}^3p_1}{(2\pi)^3}\frac{\mathrm{d}^3p_2}{(2\pi)^3}G_{N_1N_2N_3}(\boldsymbol{p}_1,\boldsymbol{p}_2,\boldsymbol{p}_3)\mathrm{e}^{-b^2P^2}, \tag{5.54}$$

where

$$\zeta=\left(\frac{2b^2}{2b^2+4\sigma^2}\right)^3 \tag{5.55}$$

is a spatial factor and

$$P^2=\frac{1}{3}\left[(\boldsymbol{p}_1-\boldsymbol{p}_2)^2+(\boldsymbol{p}_2-\boldsymbol{p}_3)^2+(\boldsymbol{p}_2-\boldsymbol{p}_3)^2\right]=\frac{2}{3}\left[\boldsymbol{p}_2^2+\boldsymbol{p}_3^2+\boldsymbol{p}_1\cdot\boldsymbol{p}_2\right] \tag{5.56}$$

is a measure of the momentum difference of the nucleons. The generalisation to a two-Gaussian wave function can in principle be achieved using the same procedure as in the deuteron case, but a “Hulthen wave function” for Helium-3 does not exist.

5.2.2 Spin and isospin factor

Consider first the general case of a system of A nucleons and charge Z coalescing into a nucleus with the same charge. The initial state has 2^A possible spin states and the final nucleus has $\binom{A}{Z}$ different isospin multiplets. Each possible isospin multiplet for the nucleus contains only one state with the correct number of protons and neutrons. Thus, in our statistical approximation, the weight to each multiplet is equal. The final statistical factor becomes

$$S=\frac{N_{\mathrm{S}}}{\binom{A}{Z}2^A}, \tag{5.57}$$

where N_{S} is the total number of possible stable spin and isospin states of the nucleus.

---

[12] The exponent becomes $((\boldsymbol{\lambda}+\boldsymbol{\lambda}')^2+(\boldsymbol{\rho}+\boldsymbol{\rho}')^2+3(\boldsymbol{R}+\boldsymbol{R}')^2)/8\sigma^2$.

The nucleus consisting of three nucleons (tritium or ^{3}He) has 6 possible spin states separated into the symmetric quadruplet

$$\left|\tfrac{3}{2}\;\tfrac{3}{2}\right\rangle = \uparrow\uparrow\uparrow, \tag{5.58a}$$

$$\left|\tfrac{3}{2}\;\tfrac{1}{2}\right\rangle = \tfrac{1}{\sqrt{3}}\left(\uparrow\uparrow\downarrow + \uparrow\downarrow\uparrow + \downarrow\uparrow\uparrow\right), \tag{5.58b}$$

$$\left|\tfrac{3}{2}\;-\tfrac{1}{2}\right\rangle = \tfrac{1}{\sqrt{3}}\left(\uparrow\downarrow\downarrow + \downarrow\uparrow\downarrow + \downarrow\downarrow\uparrow\right), \tag{5.58c}$$

$$\left|\tfrac{3}{2}\;-\tfrac{3}{2}\right\rangle = \downarrow\downarrow\downarrow, \tag{5.58d}$$

and the doublet

$$\left|\tfrac{1}{2}\;\tfrac{1}{2}\right\rangle = \sqrt{\tfrac{2}{3}}\,\uparrow\uparrow\downarrow - \sqrt{\tfrac{1}{6}}\left(\uparrow\downarrow\uparrow + \downarrow\uparrow\uparrow\right), \tag{5.58e}$$

$$\left|\tfrac{1}{2}\;-\tfrac{1}{2}\right\rangle = \tfrac{1}{\sqrt{6}}\left(\uparrow\downarrow\downarrow + \downarrow\uparrow\downarrow\right) - \sqrt{\tfrac{2}{3}}\,\downarrow\downarrow\uparrow, \tag{5.58f}$$

$$\tag{5.58g}$$

where $\uparrow \equiv |1/2\;1/2\rangle$ and $\downarrow \equiv |1/2\;-1/2\rangle$. The states consisting of only protons and neutrons are not stable and located in the quadruplet. There are thus only two isospin states in the final three-nucleon state, one for helium-3 and one for tritium. The total wave function must be antisymmetric in the exchange of two particles, and the spin state must thus be in the doublet,[13] leading to $N_\mathrm{S} = 2$. The final statistical factor becomes

$$S(\mathrm{t}) = S(^3\mathrm{He}) = \frac{1}{12}. \tag{5.59}$$

5.2.3 Lorentz transformation

The procedure for finding the correct Lorentz transformation is similar to the deuteron case. Here we will only summarise the main steps and then state the result. The nucleon Wigner function is chosen to be evaluated in the lab frame such that the spatial distribution represents the hadronisation size. In the most general case, $\sigma_\perp \neq \sigma_\parallel$, the Lorentz transformation can be written as

$$X_\perp^{\boldsymbol{P}_d\perp\prime} = X'_\perp \cos(\theta) = X_\perp^{\boldsymbol{P}_d\perp}, \tag{5.60a}$$

$$X_\perp^{\boldsymbol{P}_d\parallel\prime} = X'_\perp \sin(\theta) = \gamma\left(X_\perp^{\boldsymbol{P}_d\parallel} + vt_\mathrm{f}\right), \tag{5.60b}$$

$$X_\parallel^{\boldsymbol{P}_d\perp\prime} = X'_\parallel \sin(\theta) = X_\parallel^{\boldsymbol{P}_d\perp}, \tag{5.60c}$$

$$X_\parallel^{\boldsymbol{P}_d\parallel\prime} = X'_\parallel \cos(\theta) = \gamma\left(X_\parallel^{\boldsymbol{P}_d\parallel} + vt_\mathrm{f}\right), \tag{5.60d}$$

---

[13] Consider the tritium. The isodoublet is antisymmetric in the exchange of a proton and a neutron and symmetric in the exchange of the neutrons. The spin of the two neutrons has to be different, while the spin of the proton is equal to one of the neutrons. Thus, the spin state is antisymmetric in the exchange of two neutrons.

for a parameter X, in the same manner as in section 5.1.3. The size parameters are ultimately changed to (5.26) and the freeze-out time t_f drops out. There are all together six perpendicular and three parallel Gaussian integrals that must be evaluated. The result can be written on the same form as equation (5.54), but with

$$\zeta = \left(\frac{b^2}{b^2 + 2\tilde{\sigma}_\perp^2}\right)^2 \frac{b^2}{b^2 + 2\tilde{\sigma}_\parallel^2}, \tag{5.61}$$

where $\tilde{\sigma}_\perp$ and $\tilde{\sigma}_\parallel$ are defined in the same way as in the deuteron case (eq. (5.27) in the most general case). This implies that $\zeta(b) = \zeta_d(d = 2b)^2$, where ζ_d is the spatial distribution factor obtained for deuteron. The transformation back to the lab frame is identical to the deuteron case in section 5.1.3.

5.2.4 Model and numerical procedure

The final coalescence model for tritium and helium-3 can be written as

$$\frac{\mathrm{d}^3 N_\mathrm{He}}{\mathrm{d}P_\mathrm{He}^3} = \frac{1}{\gamma}\frac{64}{12}\zeta \int \frac{\mathrm{d}^3p_1\,\mathrm{d}^3p_2}{(2\pi)^9} G_{N_1N_2N_3}(\boldsymbol{p}_1, \boldsymbol{p}_2, \boldsymbol{p}_3)\mathrm{e}^{-b^2P^2}, \tag{5.62}$$

where P^2 is given by (5.56), the spatial factor ζ is given by (5.61). The numerical procedure is identical to that in section 5.1.5 with the only change that the weight is slightly different. In addition, P^2 is now defined in the CoM frame of a three particle state. Hence, one must use the general Lorentz transformation (A.4) to compute it. One may argue that it is sufficient to calculate the momentum differences between nucleons in P^2 in the rest frames of the corresponding nucleon pairs since those practically coincide with the rest frame of the nucleus.[14] The latter method will be used in the simulations in this thesis.

5.3 Comparison with experimental data

We will now compare the model to the experimental data from the ALICE [9], ALEPH [10] and OPAL [11] experiments considered in section 4.2. For concreteness, we restrict the considered spatial distribution factors ζ to the simplest case (eq. (5.13)), most physically favoured case (eq. (5.36)), and something in between (eq. (5.20)). These will be called *constant*, *beam independent* and *beam dependent*, respectively.

A χ^2-fit of the considered models has been performed on the experimental data. The best-fit values, their 1σ errors and the reduced χ^2 of the various fits are listed in table

---

[14] Remember that we have previously used the assumption the the nucleons and nucleus are the same Lorentz frame due to the low binding energy of the nucleus. These methods are equivalent within this approximation.

5.1. Note that the χ^2 for ALEPH is not defined since the experiment only consists of one data point, and that the yield in the one-Gaussian case was too low to be able to recreate the ALEPH and OPAL experiments. At the best fit $\sigma = 0$, the yield was 0.53 standard deviations off. Furthermore, only the one-Gaussian case is defined for helium-3.

The best combined fits to the ALICE antideuteron data are plotted in figure 5.5 for the constant and beam dependent ζ, and the one-Gaussian and two-Gaussian φ_0-fit wave functions. Only the constant and beam dependent ζ-factor, and the one-Gaussian and two-Gaussian ϕ_0-fit wave functions are included. The difference between the two-Gaussian wave functions (ϕ_0-fit, r^3-fit and average) is small. The result for the old coalescence model is also plotted for comparison. One can note that the constant models and the one-Gaussian models are visually quite similar to the old model, while the two-Gaussian beam dependent model has a significantly improved fit.

The χ^2 values obtained when the combined best fit to the antideuteron data are used on the helium-3 and e^+e^- data are listed in table 5.2. Since the goodness-of-fit parameter is small for the e^+e^- data, one can conclude that a single universe parameter σ can consistently describe the two data sets. The large χ^2 value for helium-3 can be explained by the choice of wave functions, but it will be interesting to check it by future antihelium data with smaller uncertainties. The fit to the antihelium-3 data is plotted in figure 5.6 for its best fit parameters, as well as the best fit parameters from the combined ALICE antideuteron data with the two-Gaussian φ_0-fit.

Due to the number of bins and small uncertainties, the ALICE antideuteron data will now be used to give a set of suggested parameters. As clear from table 5.1 and figure 5.5, the two-Gaussian probability distributions give notably better fits than the one-Gaussian probability distribution. The beam independent ζ leads in turn to a significantly better fit. Furthermore, the goodness-of-fit parameter χ^2 is acceptable when these parameters are used on the other data sets, as indicated in table 5.2. Of the two-Gaussian wave functions, the φ_0-fit is the simplest and has the best fit. We will thus use this when discussing the antideuteron flux in the next chapter. In summary, one should use the model with the two-Gaussian φ_0-fit wave function and beam independent ζ with $\sigma_{(pp)} = 7.6\,\mathrm{GeV}^{-1}$ for pp collisions and $\sigma_{(e^+e^-)}\sigma_{(pp)}/\sqrt{2} = 5.4\,\mathrm{GeV}^{-1}$ for e^+e^- collisions for Pythia 8.230.

The parameters should in principle be the same for helium-3 and tritium if an exact wave function was chosen. Thus, one may either use the parameters from the two-Gaussian φ_0-fit or rely on the single experiment and use $\sigma = 4.5\,\mathrm{GeV}^{-1}$ for pp collisions and $3.2\,\mathrm{GeV}^{-1}$ for e^+e^- collisions. As seen from table 5.1, the fit to the antihelium data is somewhere in between the two-Gaussian and one-Gaussian fits, as one may expect by the choice of wave functions.

Table 5.1: Fit results of all ζ-factors and antideuteron probability distributions to the ALICE experiment at $\sqrt{s} = 0.9, 2.76$ and 7 TeV, the combined ALICE antideuteron data, the ALICE helium-3 data, the ALEPH experiment and the combined ALEPH and OPAL experiments.

Experiment	one-Gaussian		two-G., φ_0-fit		two-G., r^3-fit		two-G., avg.	
	$\sigma\ [\frac{1}{\text{GeV}}]$	$\frac{\chi^2}{N-1}$	$\sigma\ [\frac{1}{\text{GeV}}]$	$\frac{\chi^2}{N-1}$	$\sigma\ [\frac{1}{\text{GeV}}]$	$\frac{\chi^2}{N-1}$	$\sigma\ [\frac{1}{\text{GeV}}]$	$\frac{\chi^2}{N-1}$
Constant ζ								
0.9 TeV	3.5 ± 0.7	7.5/2	6.2 ± 0.3	6.0/2	6.6 ± 0.3	7.1/2	6.4 ± 0.3	6.6/2
2.76 TeV	4.3 ± 0.3	44/6	6.6 ± 0.1	32/6	7.0 ± 0.2	40/6	6.8 ± 0.4	36/6
7 TeV	4.1 ± 0.2	182/19	6.6 ± 0.1	133/19	6.8 ± 0.1	168/19	6.7 ± 0.1	151/19
combined	4.1 ± 0.1	235/29	6.6 ± 0.1	172/29	6.9 ± 0.1	216/29	6.7 ± 0.1	194/29
helium-3	4.5 ± 0.9	1.7/2	-	-	-	-	-	-
ALEPH	$0^{+2.3}_{-0}$	-	$5.0^{+0.9}_{-0.6}$	-	$5.0^{+1.2}_{-0.9}$	-	$5.0^{+1.1}_{-0.7}$	-
+OPAL	$0^{+4.4}_{-0}$	3.2/1	$5.5^{+1.3}_{-1.1}$	3.2/1	$5.6^{+1.6}_{-1.5}$	3.2/1	$5.5^{+1.5}_{-1.2}$	3.2/1
Beam independent ζ								
0.9 TeV	3.7 ± 0.8	7.2/2	6.6 ± 0.3	4.3/2	7.0 ± 0.4	5.6/2	6.8 ± 0.3	5.0/2
2.76 TeV	4.7 ± 0.3	40/6	7.1 ± 0.1	19/6	7.5 ± 0.2	28/6	7.3 ± 0.3	24/6
7 TeV	4.4 ± 0.2	165/19	7.1 ± 0.1	69/19	7.4 ± 0.1	107/19	7.3 ± 0.1	87/19
combined	4.4 ± 0.1	213/29	7.1 ± 0.1	94/29	7.4 ± 0.1	142/29	7.2 ± 0.1	118/29
helium-3	4.8 ± 0.9	1.4/2	-	-	-	-	-	-
ALEPH	$0^{+2.4}_{-0}$	-	$5.2^{+1.0}_{-0.6}$	-	$5.2^{+1.3}_{-0.9}$	-	$5.2^{+1.1}_{-0.7}$	-
+OPAL	$0^{+4.5}_{-0}$	3.2/1	$5.7^{+1.4}_{-1.1}$	3.2/1	$5.8^{+1.7}_{-1.5}$	3.2/1	$5.7^{+1.5}_{-1.3}$	3.2/1
Beam dependent ζ								
0.9 TeV	3.9 ± 0.8	6.7/2	6.9 ± 0.3	2.6/2	7.2 ± 0.5	3.7/2	7.0 ± 0.3	3.3/2
2.76 TeV	4.9 ± 0.3	35/6	7.5 ± 0.1	8.6/6	7.8 ± 0.3	16/6	7.7 ± 0.2	12/6
7 TeV	4.7 ± 0.2	143/19	7.6 ± 0.1	29/19	7.8 ± 0.1	55/19	7.7 ± 0.1	40/19
combined	4.7 ± 0.4	186/29	7.6 ± 0.1	45/29	7.8 ± 0.1	78/29	7.7 ± 0.1	59/29
helium-3	5.2 ± 1.0	1.1/2	-	-	-	-	-	-
ALEPH	$0^{+2.4}_{-0}$	-	$5.3^{+1.0}_{-0.6}$	-	$5.2^{+1.3}_{-0.9}$	-	$5.3^{+1.1}_{-0.7}$	-
+OPAL	$0^{+4.6}_{-0}$	3.2/1	$5.8^{+1.4}_{-1.1}$	3.2/1	$5.9^{+1.7}_{-1.5}$	3.2/1	$5.8^{+1.6}_{-1.3}$	3.2/1

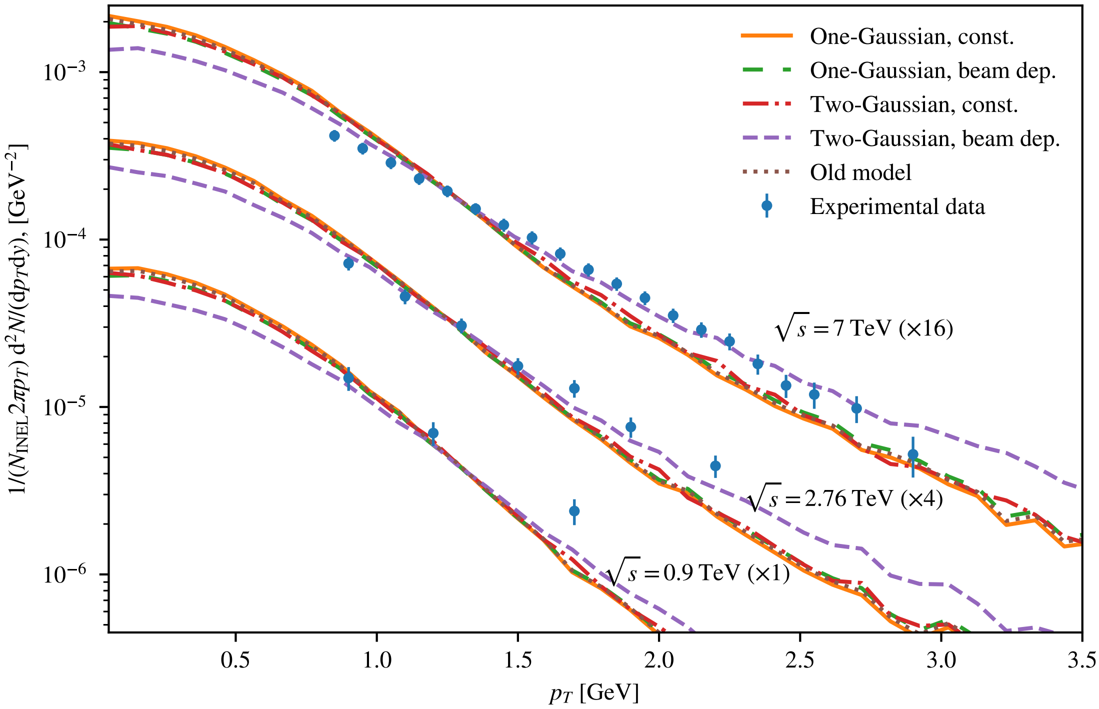

Figure 5.5: Best combined fits to the ALICE antideuteron data for the considered models. The data and fits are multiplied by a constant factor to make the figure clearer.

Table 5.2: Goodness-of-fit parameter χ^2 obtained when the best combined fit parameters from the ALICE antideuteron data are used on the helium-3, ALEPH and OPAL data.

ζ	experiment / χ^2	one-G.	two-G. ϕ_0-fit	two-G. r^3-fit	two-G. avg.
Const.	Helium-3	1.9	5.7	6.4	6.0
	ALEPH	1.3	0.36	0.093	0.12
	ALEPH + OPAL	3.5	4.5	3.9	4.0
Beam indep.	Helium-3	1.6	5.8	6.4	6.1
	ALEPH	1.4	0.078	0.009	0.008
	ALEPH + OPAL	3.6	3.9	3.587	3.6
Beam dep.	Helium-3	1.3	6.0	6.4	6.2
	ALEPH	1.5	0.018	0.014	0.026
	ALEPH + OPAL	3.6	3.3	3.4	3.3

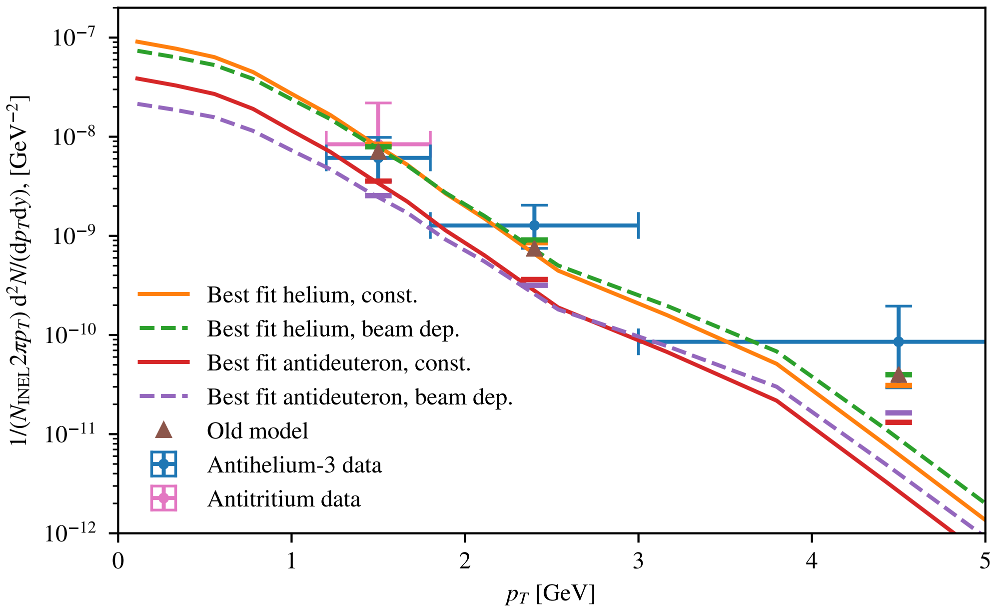

Figure 5.6: Best fits to the ALICE antihelium data for the one-Gaussian models. The best fits using the parameters obtained from the best combined fit to the ALICE antideuteron data is also plotted.

6 Computing the antideuteron and antihelium spectra

Antideuteron and antihelium-3 may be created in DM annihilations or decays in the Galaxy. In this chapter, we will compute the antideuteron and antihelium-3 source spectra from DM annihilations for some benchmark cases and use the two-zone propagation model to estimate the resulting flux on Earth. The background of secondary nuclei will also be estimated. The uncertainties due to the different DM distributions and propagation models have been extensively detailed in the literature (see e.g. Refs. [48, 49, 52, 60]). We will thus focus on the the detection prospects and uncertainties related to the new model developed in the previous chapter, as well as the difference between the old and new per-event coalescence models.

WIMP annihilations are similar to the e^+e^- annihilation process. For the old coalescence model we therefore use the calibration to the ALEPH data to describe the antideuteron formation in WIMP annihilations. However, due to the lack of a microphysical understanding of p_0, we must use the value obtained in the fit to the ALICE helium-3 data to describe the formation of helium-3 and tritium. For the new models, we use instead the best fit to the ALICE pp data rescaled by a factor $1/\sqrt{2}$. The background is mainly dominated by the production from collisions of cosmic ray protons hitting the protons (hydrogen) in the Galactic disk. Thus, when computing the secondary flux we use the best fit to the ALICE data in all cases.

6.1 Source spectra

6.1.1 Primaries

The DM annihilations will lead to injection spectra $\mathrm{d}N_{\bar{N}}/\mathrm{d}T$ of antideuteron, antihelium-3 and antitritium. It is common to consider a set of benchmark channels and masses. A specific DM model can then be considered by weighting the different channels according to the theoretical branching ratios of the model. We will consider a fermionic Majorana particle with mass m_χ annihilating into the colour neutral state $\bar{b}b$ and the state W^+W^-. These annihilation channels serve as benchmarks for other heavy quarks and bosons, respectively. The annihilation process is modelled in Pythia 8.230 by creating a “blob” of energy with $\sqrt{s} = 2m_\chi$ and only one possible decay channel at a time. The masses $m_\chi =$

$\{100, 1000\}$ GeV will be considered. About 10^9 events will be used in the antideuteron production and 10^{10} in the antihelium production.

It was previously common to assume that the Coulomb repulsion of the antiprotons suppresses the antitritium production [8]. However, as seen the two previous chapters, the ALICE experiment found comparable antihelium-3 and antitritium yields. As the antitritiums produced in the DM annihilations have a short lifetime (~ 12.5 years) compared to the proper propagation time (~ 1 Myr), it will decay to antihelium-3 before reaching Earth. Thus, we will consider the combined antitritium and antihelium-3 source spectra as the source of antihelium-3.

The injection spectra for the considered benchmark cases and the different considered coalescence models are shown in figure 6.1 for antideuteron and in figure 6.2 for antihelium-3. Consider first the antideuteron injection spectra. The source spectra using the old model are in accordance to the results in existing works, such as Refs. [51, 52]. We note that the new models with constant ζ and the old model yields similar spectra that differ only by a small factor that may be explained by the difference in the calibration procedure. In particular, the one-Gaussian model has a similar shape as the old model, but with a smaller flux. The reason is, as noted in the previous chapter, that the model does not yield a flux that is large enough to reproduce the ALEPH data which the old model is calibrated by. Furthermore, the spectra obtained using the two-Gaussian beam dependent ζ differ significantly from the old model: there is a larger flux at large energies ($T \gtrsim 0.1\,\mathrm{GeV}/2$) and a smaller flux at small energies ($T \lesssim 0.1\,\mathrm{GeV}/2$). Lastly, we note that even the cases with constant ζ lead to a lower energy spectra at low energies $T \lesssim 0.1\,\mathrm{GeV}/n$, n being the number of nucleons in the nuclei ($n = 2$ for antideuteron). From now on, we will only consider the two-Gaussian wave function when discussing the antideuteron production.

The same characteristics as in the antideuteron case can be seen in the antihelium-3 injection spectra as well, but the results are not as clear due to the small amount of statistics. Here another advantage of the new model is apparent: it require less statistics. In the helium-3 injection spectra, the new and old models are used on the same data set, yet the new models yield smoother spectra. One can further note that the flux using the old model is smaller than the new models. This is due to the calibration of the models: both the old and new models were calibrated to the antihelium-3 data from ALICE, but the free parameter in the new model, σ, was rescaled by $1/\sqrt{2}$ as expected from its microphysical picture.

The primary source can in turn be written as [67]

$$Q(\boldsymbol{r}, T) = \frac{1}{2}\frac{\rho^2(\boldsymbol{r})}{m_\chi^2}\sum_i \langle\sigma v\rangle_i \frac{\mathrm{d}N_{\bar{N}}^i}{\mathrm{d}T_{\bar{N}}}, \tag{6.1}$$

where the sum goes over the possible annihilation channels, ρ is the DM distribution discussed in section 2.1.2 and $\langle\sigma v\rangle_i$ is the thermally averaged annihilation cross section for the given channel. We will consider a single annihilation channel at a time and assume $\langle\sigma v\rangle = 3 \times 10^{-26}\,\mathrm{cm}^3/\mathrm{s}$ as motivated by the discussions in section 2.3.4.

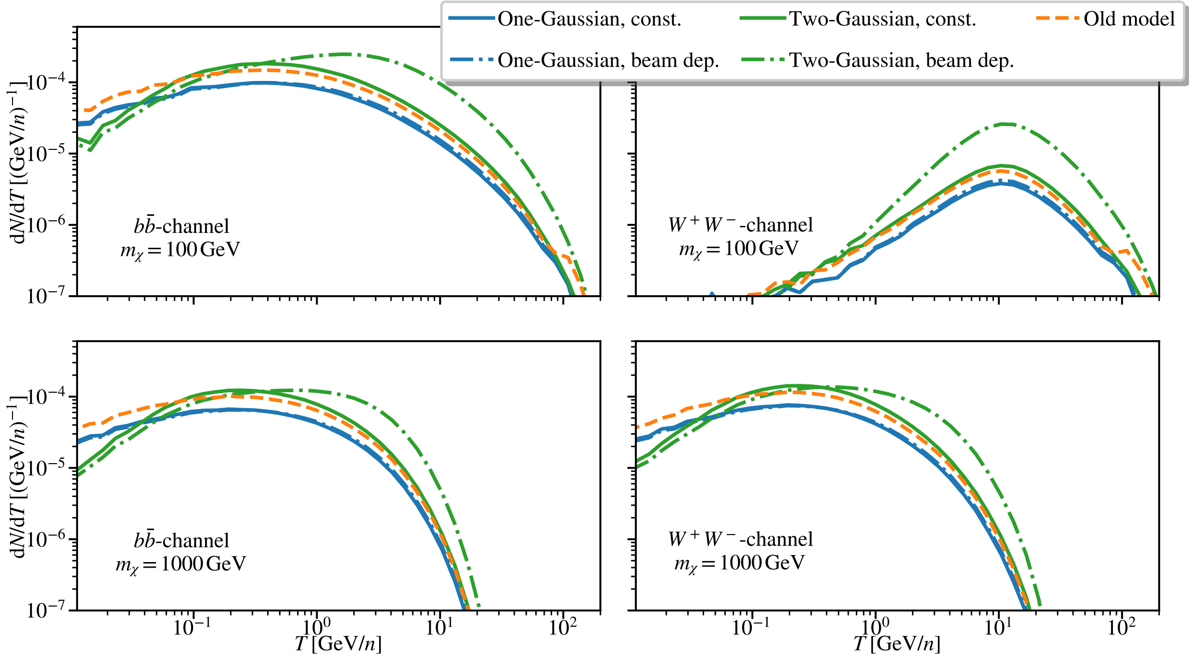

Figure 6.1: The injection spectra for the benchmark channels $\chi\chi \to W^+W^-$ and $\chi\chi \to \bar{b}b$ and the DM masses $m_\chi = \{100, 1000\}$ GeV for the considered models.

6.1.2 Secondaries

There will be some astrophysical background of antideuteron and antihelium-3 resulting from mainly cosmic ray proton and helium colliding with mainly the hydrogen and helium in the Galactic disk. This is known as secondary production. The source term of secondary antinuclei can be written as [50]

$$Q^{\mathrm{sec}}(T_{\bar{N}}, \boldsymbol{r}) = \sum_{i\in\{p,\mathrm{He},\bar{p}\}} \sum_{j\in\{p,\mathrm{He}\}} 4\pi n_j(\boldsymbol{r}) \int_{T_{\mathrm{min}}^{(i,j)}}^{\infty} \mathrm{d}T_i \, \frac{\mathrm{d}\sigma_{i,j}(T_i, T_{\bar{N}})}{\mathrm{d}T_{\bar{N}}} \Phi_i(T_i, \boldsymbol{r}), \tag{6.2}$$

where $n_j(\boldsymbol{r})$ is the density of particle j in the Galactic disk, T_{min} is the threshold energy for the production of the antinucleus, $\mathrm{d}\sigma_{i,j}(T_i, T_{\bar{N}})/\mathrm{d}T_{\bar{N}}$ is the differential cross section for the process $ij \to \bar{N}X$ when $\bar{N}$ has the kinetic energy $T_{\bar{N}}$, and $\Phi_i(T_i, \boldsymbol{r})$ is the primary flux of the incident particle.

Secondary antideuterons have been extensively detailed in Refs. [50, 68] for the spectral model and in Ref. [69] for the MC approach. The source spectrum is dominated by the process $pp \to \bar{N}X$, except from a small part of the low energy tail which is governed by incident antiprotons due to the reduced threshold energy for antideuteron production. Reactions involving helium tribute on average $\sim 30\,\%$. Thus, since the main focus of this chapter is the difference in the detection prospects of the different coalescence models, we

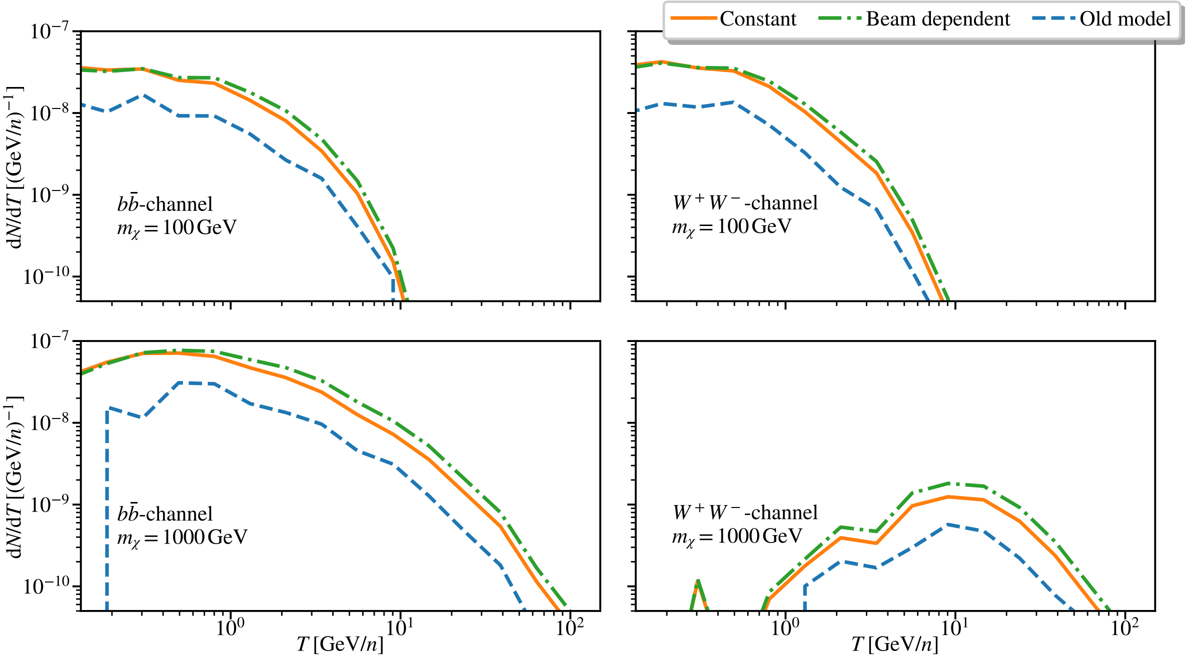

Figure 6.2: The injection spectra for the benchmark channels $\chi\chi \to W^+W^-$ and $\chi\chi \to \bar{b}b$ and the DM masses $m_\chi = \{100, 1000\}$ GeV for the considered models.

approximate the secondary source spectrum by the pp contribution,

$$Q^{\text{sec}}(T, \boldsymbol{r}) = 4\pi n_p(\boldsymbol{r}) \int_{T_{\min}}^{\infty} \mathrm{d}T' \, \frac{\mathrm{d}\sigma_{pp\to\bar{N}X}(T', T_{\bar{N}})}{\mathrm{d}T_{\bar{N}}} \Phi_p(T'). \tag{6.3}$$

The secondary antideuteron and antihelium-3 spectra will be computed by producing fixed target inelastic pp collisions in Pythia 8.230. The differential cross section will be approximated as

$$\frac{\mathrm{d}\sigma_{pp}(T_p, T_{\bar{N}})}{\mathrm{d}T_{\bar{N}}} = \sigma_{pp,\text{inel}} \frac{\mathrm{d}N_{\bar{N}}(T_p, T_{\bar{N}})}{\mathrm{d}T_{\bar{N}}}, \tag{6.4}$$

where $\sigma_{pp,\text{inel}}(T_p)$ is the inelastic pp cross section estimated by Pythia 8. The primary proton flux can be parametrised by [70]

$$\Phi_p(T) = \left(\frac{T}{T+b}\right)^c \left(A_1 T^{-\gamma_1} + A_2 T^{-\gamma_2}\right), \tag{6.5}$$

with $A_1 = 53488\,(\mathrm{m}^2\mathrm{s}\,\mathrm{sr}\,\mathrm{GeV}/n)^{-1}, A_2 = 3294\,(\mathrm{m}^2\mathrm{s}\,\mathrm{sr}\,\mathrm{GeV}/n)^{-1}, b = 2.40\,\mathrm{GeV}/n, c = 2.588, \gamma_1 = 3.168$ and $\gamma_2 = 2.576$, which is found by fitting the parametrisation to the newest cosmic ray proton data from AMS-02.[1] The parametrisation holds for $T > 10\,\mathrm{GeV}$ where the effect from Solar modulation is small. Furthermore, we assume that $n_p(\boldsymbol{r}) = 1\,\mathrm{cm}^{-3}$ in the disk (which we will later assume to have a half-height $h = 100\,\mathrm{pc}$). We follow Ref. [69] and compute $\mathrm{d}\sigma_{pp}/\mathrm{d}T$ with incident kinetic energy T_p in 53 logarithmic bins from 25 to 10^4 GeV.[2] The resulting secondary antideuteron and antihelium-3 spectra for the different considered coalescence models are shown in figure 6.3. The result for antideuteron is in accordance with the results by Ref. [69] for the old coalescence model.

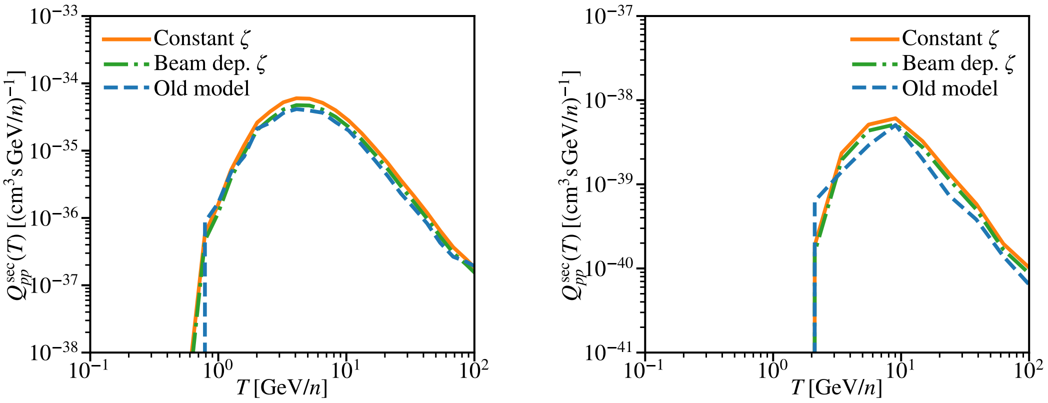

Figure 6.3: Secondary source spectrum of antideuteron (left) and antihelium-3 (right) from incident protons colliding with the hydrogen in the ISM.

6.1.3 Tertiaries

In addition to the secondary and primary source, there will be a contribution from primaries and secondaries colliding inelastically with the ISM. This is known as a tertiary source and will lead to a redistribution of the energy that replenishes the low energy part of the spectra. For the primary antideuterons and antihelium-3, this can be neglected [51, 53]. For the secondary species, this effect is notable but small [50]. We will therefore neglect the tertiary contribution in the current analysis.

---

[1] It was previously common to use a single exponential $\Phi \propto E^{-\gamma}$ with $\gamma \simeq 2.7$, but the PAMELA experiment observed a stiffening of the proton flux around $\sim 200\,\mathrm{GeV}$ which was later confirmed by AMS-02.

[2] The integral is solved using the Simpson method with variable step length, and the trapezoid method is in turn used to check that the error related to the integration is small.

6.2 Propagation through the Galaxy

6.2.1 Two-zone propagation model

Charged particles propagating through the Milky Way are affected by magnetic fields which ultimately leads to a random walk behaviour that can be described by a diffusion equation. The two zone propagation model is a standard tool to approximate the propagation of a charged particle in the Galaxy and has been discussed in more detail in e.g. Refs. [1, 52, 68]. Here we will only highlight the main features of the model. In order to improve the results, one may instead use a more sophisticated complete numerical treatment using for example the GALPROP code [71].

In the two-zone propagation model, the Galaxy is divided into two zones: a cylinder of radius R and a large thin disk. The cylinder has a half-height L out of the Galactic disk on either side, while the disk has a half-height $h \ll L$. Therefore one can assume that the ISM is concentrated at $z = 0$, where z denotes the vertical distance from the Galactic plane. The two parameters R and h are set to $R = 20\,\mathrm{kpc}$ and $h = 100\,\mathrm{pc}$. The propagation of the charged particles is assumed to be confined to the cylinder, and the disk is the place the cosmic ray interacts with the ISM. In this model, the diffusion equation can be written in cylindrical coordinates as

$$\begin{aligned} -\nabla\left[K(r,z,E)\nabla n_{\bar{N}}(r,z,E)\right] + \frac{\partial}{\partial z}\left[\mathrm{sign}(z) V_c n_{\bar{N}}(r,z,E)\right] \\ +2h\delta(z)\Gamma^{\bar{N}}_{\mathrm{ann}} n_{\bar{N}}(r,z,E) = q_{\bar{N}}(r,z,E), \end{aligned} \tag{6.6}$$

where $n_{\bar{N}}$ is the antinucleus number density at energy E, $q_{\bar{N}}$ is the source term, K is the diffusion coefficient, V_c is the convection velocity, $\Gamma^{\bar{N}}_{\mathrm{ann}}$ is the annihilation rate with interstellar gas, and r denotes the distance from the Galactic centre along the Galactic plane. In equation (6.6), both re-acceleration and energy losses have been neglected, as they have been show to have little impact on the final primary spectrum [67]. Note, however, that energy loss yields a non-negligible contribution to the low-energy tail ($\lesssim$ few GeV) on the background spectra (secondary and tertiary). Since this is already detailed in Ref. [69] and since the main focus of this chapter is on the difference between the old and new coalescence models, we will neglect energy losses even for the secondary flux. The annihilation rate of an antinucleus $\bar{N}$ can be approximated by

$$\Gamma^{\bar{N}}_{\mathrm{ann}} = (n_{\mathrm{H}} + 4^{3/2} n_{\mathrm{He}}) v_{\bar{N}} \sigma^{\mathrm{ann}}_{\bar{N}p}, \tag{6.7}$$

where $n_{\mathrm{H}} = 1\,\mathrm{cm}^{-3}$ and $n_{\mathrm{He}} = 0.07 n_{\mathrm{H}}$ is the interstellar densities of hydrogen and helium in the Galactic disk, $4^{3/2}$ is a geometrical factor accounting for cross section difference between helium and hydrogen, $v_{\bar{N}}$ is the antinucleus velocity and $\sigma^{\mathrm{ann}}_{\bar{N}p}$ is the annihilation cross section of the $p\bar{N}$ collision. We estimate the annihilation cross section as $\sigma^{\mathrm{ann}}_{\bar{N}p}(T) = \sigma^{\mathrm{tot}}_{\bar{N}p}(T) - \sigma^{\mathrm{el}}_{\bar{N}p}(T) - \sigma^{\mathrm{non\text{-}ann}}_{\bar{N}p}(T)$. The different terms and the parametrisations used are described in appendix C.

Table 6.1: Benchmark parameters for the two-zone propagation model.

Model	L [kpc]	δ	K_0 [kpc^2/Myr]	V_c [km/s]
max	15	0.46	0.0765	5
med	4	0.7	0.0112	12
min	1	0.85	0.0016	13.5

Diffusion arises due to interaction between the charged particles and the highly turbulent magnetic field. The diffusion coefficient is poorly known, and it is therefore common to assume the standard rigidity dependent form

$$K(E) = \beta K_0 \mathcal{R}^{\delta}, \tag{6.8}$$

where K_0 and δ are free parameters of the model and are assumed to be the same in the entire Galaxy. The convective wind is assumed to be constant and directed away from the Galactic plane.

The final model only depends on four parameters:[3] L, K_0, δ and V_c. These parameters have been constrained using a cosmic ray boron-to-carbon ratio study [72, 73], in which many sets of parameters were accepted. In table 6.1 the three benchmark parameter sets 'min', 'med' and 'max' are listed. These corresponds to the minimum flux compatible with the data, the best fit to the data and the maximum flux compatible with the data, respectively. However, note that the three parameter sets do not represent the entire uncertainty range [49], and that additional multichannel analyses have constrained the parameters further. For example, an analysis of cosmic ray electron and positron spectra and of the diffuse synchrotron emission of the Galaxy added the constraint $L \gtrsim 2\,\mathrm{kpc}$ [74]. Furthermore, measurements from AMS-02 on the boron-to-carbon ratio indicate that $\delta \approx 1/3$ [75], which in turn suggests that 'min' and 'med' parameters are physically unfavoured, although it is important to keep in mind that the exact value is model dependent. In any case, the given parameters serve as benchmarks that can be used to compare with existing works.

The diffusion equation (6.6) can be solved semi-analytically using the aforementioned assumptions and approximations using cylindrical coordinates and an expansion in Bessel functions [67].[4] The total flux from the primary species at the position of the Sun ($r = r_\odot$) from annihilating Majorana DM particles can be expressed as

$$\Phi_{\bar{N}}(T, \boldsymbol{r}_\odot) = \frac{v_{\bar{N}}}{4\pi} \left(\frac{\rho_\odot}{M_{\mathrm{DM}}}\right)^2 R_{\bar{N}}(T) \frac{1}{2} \langle \sigma v \rangle \frac{\mathrm{d}N_{\bar{d}}}{\mathrm{d}E}, \tag{6.9}$$

---

[3] Note that the model in Ref. [68] have an additional parameter V_a called the Alfvénic speed. This leads to a re-acceleration in the thin disk, but this can be neglected. See Ref. [52] for more information.

[4] When energy loss and tertiaries are taken into account, one must solve the diffusion equation numerically using for example the method detailed in Ref. [76].

where $v_{\bar{N}}$ is the antinucleus speed and $\langle\sigma v\rangle$ is the annihilation cross section for the process. All of the astrophysical information is encoded in $R_{\bar{N}}(T)$. The propagation function $R_{\bar{N}}(T)$ is independent on the source spectrum and the DM mass, and one therefore only need to evaluate it once. It is given by

$$R_{\bar{N}}(T) = \sum_{i=1}^{\infty} J_0\left(\zeta_i \frac{r_\odot}{R}\right) \exp\left(-\frac{V_c L}{2K}\right) \frac{y_i(L)}{A_i \sinh(S_i L/2)}, \tag{6.10}$$

where J_n is the nth order Bessel function, and

$$Q_i(z) = \frac{2}{[J_1(\zeta_i)R]^2} \int_0^R \mathrm{d}r\, r J_0\left(\frac{\zeta_i r}{R}\right)\left(\frac{\rho(r,z)}{\rho_\odot}\right)^2, \tag{6.11}$$

$$y_i(z) = 2\int_0^z \mathrm{d}z' \exp\left(\frac{V_c}{2K}(z-z')\right) \sinh\left(\frac{S_i}{2}(z-z')\right) Q_i(z'), \tag{6.12}$$

$$S_i = \sqrt{\frac{V_c^2}{K^2} + 4\frac{\zeta_i^2}{R^2}}, \tag{6.13}$$

$$A_i = 2h\Gamma_{\mathrm{ann}}^{\bar{N}} + V_c + KS_i \coth\left(\frac{S_i L}{2}\right). \tag{6.14}$$

The expression for the propagation of the secondary flux is similar, but is simpler since the source contains the factor $n(\boldsymbol{r}) \propto 2h\delta(z)$.

6.2.2 Numerical evaluation of the propagation function

We evaluate the propagation function for antideuteron and antihelium for the three benchmark parameter sets ‘min’, ‘med’ and ‘max’ in table 6.1 and the three DM distributions isothermal, Einasto and NFW considered in section 2.1.2. The propagation function $R(T)$ is hard to evaluate numerically for two main reasons. Firstly, the hyperbolic functions diverges. Secondly, the sum converges only slowly and the evaluation time of each new term increases fast. These problems can be treated by combining the exponentials and the hyperbolic functions, and choosing the convergence conditions wisely. When $R(T)$ as a function of the number of included terms, $R_i(T)$, is plotted, one notices that the sum has a damped oscillating behaviour with a period of five terms. The average of the last five $R_i(T)$ evaluations converges far faster than $R_i(T)$. We thus require that $\sum_i^{i+5} R_i(T)/5 < \epsilon$.[5] We use $\epsilon = 10^{-4}$ for the sum and use an adaptive integration method with an absolute and relative tolerance less than 10^{-7} to evaluate the integrals.[6]

---

[5] With this condition, the evaluation of $R(0.1\,\mathrm{GeV})$ with the NFW distribution and the ‘min’ parameter set — which is the considered function evaluation that converges most slowly — uses about 3000 steps and 45 CPU minutes with $\epsilon = 10^{-4}$. The evaluation of the next term increases fast, and so this evaluation becomes undoable both due to time constraints and floating point errors if a standard stopping criterion, such as $|R_{i+1} - R_i| < \epsilon$, is used.

[6] The function *QAG* from QuadPack [77] is used.

The final propagation functions for primary antideuteron and antihelium-3 are shown in figure 6.4. As can be seen from the figure, the uncertainty related to the different distribution profiles is smaller than for the different parameters. The propagation function for the secondary species is similar, but does not depend on the DM distribution. In addition, the difference between the parameters sets is, as we will see later, small.

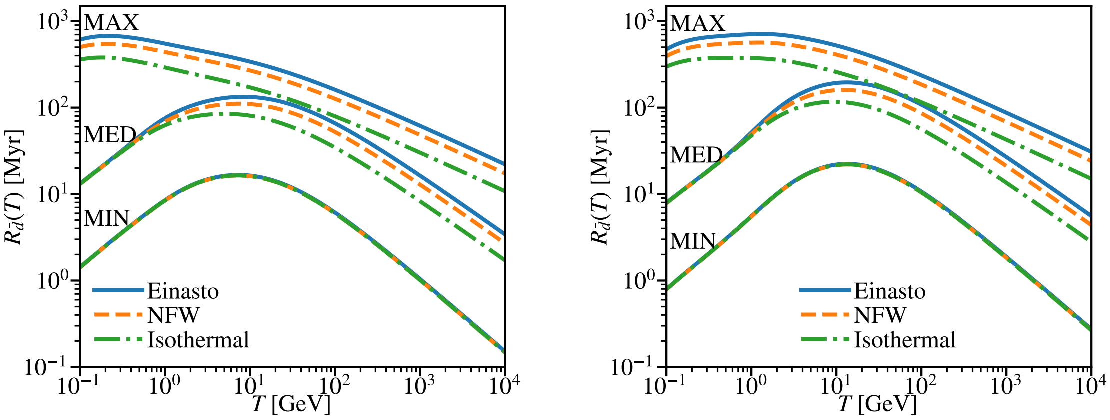

Figure 6.4: The primary antideuteron and antihelium-3 propagation functions $R(T)$ for the considered DM distribution profiles and propagation parameters.

6.2.3 Solar modulation

When the antideuterons approaches the Solar system, they will start to be modulated by the Solar magnetic field. One should therefore consider the propagation through the heliosphere separately. Due to the magnetic field, the charged particles will follow the magnetic field lines and suffer an additional adiabatic energy loss that can be described by the diffusion equation [78, 79]

$$\frac{\partial f}{\partial t} = -(\boldsymbol{V}_{\text{sw}} + \boldsymbol{v}_d) \cdot \nabla f + \nabla \cdot (\mathrm{K} \cdot \nabla f) + \frac{p}{3}(\nabla \cdot \boldsymbol{V}_{\text{sw}}) \frac{\partial f}{\partial p}, \tag{6.15}$$

where f is the antideuteron momentum distribution, p is the antideuteron momentum, K is the diffusion tensor, $\boldsymbol{V}_{\text{sw}}$ is the velocity of the Solar wind and $\boldsymbol{v}_d$ is the velocity of the antideuteron drift. In order to solve this equation, one needs to specify the Solar system geometry, as well as diffusion, winds and drift properties. By amongst other assuming that the heliosphere is spherically symmetric, one obtains the force-field solution (lowest-order approximation)[79, 80]

$$j(r, E) = j_{\text{lis}}(E + Ze\phi) \frac{E^2 - m^2}{(E + Ze\phi)^2 - m^2}, \tag{6.16}$$

where j is the flux at a radial distance r, j_{lis} is the local interstellar flux, Ze is the particle charge, m is the particle rest mass and ϕ is the Fisk potential.[7] The Fisk potential is a pseudo-steady state solution that is correlated to the Solar activity, most notably the $\sim$ 11 year solar activity cycle. The value of ϕ should thus be tuned to experimental data, such as antiproton measurements, around the same time period as the antideuteron measurements. The Fisk potential is typically in the range from 300 to 700 MV [8]. In the next section, we will be using $\phi = 500\,\text{MV}$.

Ideally, the solar modulation should be treated numerically, for example by using the HelioProp code as done in Ref. [52]. This has the advantage of taking into account the polarisation of the Sun and the antideuteron velocity $\boldsymbol{v}_d$, as well as the opposite polarisations on the two Solar hemispheres. Moreover, the force-field approximation reproduces only the average modulation while Monte Carlo method can also take into account fluctuations as well as spectral features of the particle flux. The uncertainties arising from solar modulation modelling are not very large, but can reach a maximum of a factor 2.5 for light DM particles at the top of the atmosphere [52]. All the same, the uncertainty remains small compared to the uncertainties related to the propagation through the Galaxy and the antideuteron formation ($\approx 20\,\%$ [8, 52]).

There will be some additional effects due to geomagnetic deflection and atmospheric influences [8]. Here we will compute the antinucleus flux at the top of the atmosphere and neglect these effects.

6.3 Final spectra and detection prospects

The expected flux on Earth from WIMP annihilations and secondary production can now be estimated by employing the two-zone propagation model and force-field approximation, discussed in section 6.2, on the source spectra computed in section 6.1. For concreteness, we consider only the Einasto distribution profile and the same benchmark cases as for the source spectra. The estimated antideuteron flux is shown in figure 6.5 with the 'med' parameters. The shaded area corresponds to the expected GAPS long duration balloon flight (105 days) (yellow) and five year AMS-02 sensitivity (purple) [8, 81]. The flux is regarded as detectable if it reaches the shaded area. The opaque regions around the fluxes corresponds to a typical uncertainty range related to the different formation models. For the new models $\Delta\sigma = 1\,\text{GeV}^{-1}$ has been used. This corresponds the uncertainty related to the ALEPH experiment considered in sections 4.2 and 5.3. The uncertainty in the old model is not shown in order to make the figure clearer, but it is similar to the new model with constant ζ.

Note that the ALICE experiment includes more data points with smaller uncertainty bands, but the estimated uncertainties in table 4.4 includes only the fit uncertainty. In

---

[7] The parameter ϕ is also known as the force-field potential or modulation potential.

addition, one expects that the models induces additional uncertainties. In particular, the old model and the new model with constant ζ does not describe the ALICE data well at large p_T. In order to obtain a proper uncertainty estimate, more experiments should be considered. However, there are currently few e^+e^- and pp experiments with small uncertainties available that can be used. Note that the estimated sensitivity of AMS-02 and GAPS are based on studies during the development phases of the experiments. Updated studies based on the final configurations is therefore warranted.

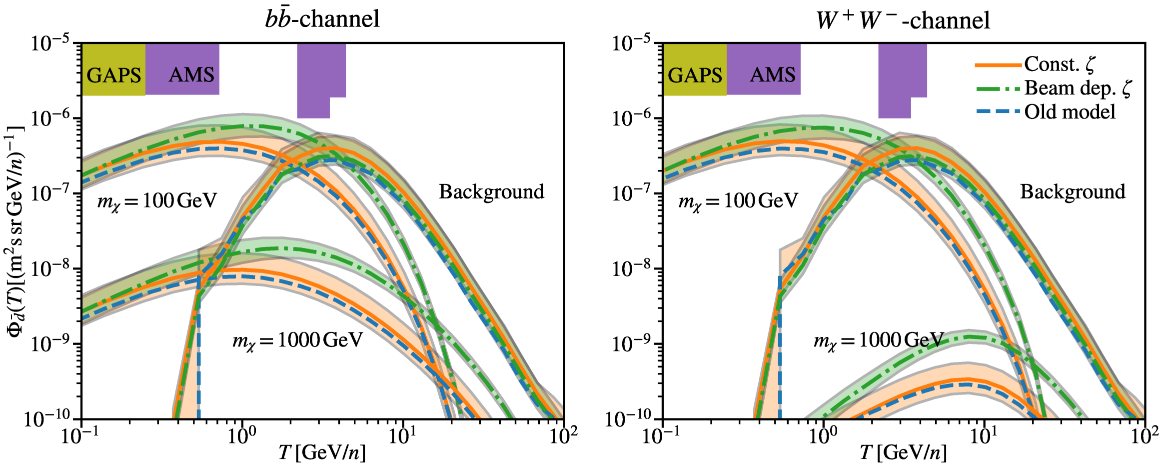

Figure 6.5: Estimated antideuteron flux on Earth from WIMP annihilations and secondary production for the considered benchmark cases and the 'med' propagation parameters. The shaded area around the flux for the new models corresponds the uncertainty $\Delta\sigma = 1\,\mathrm{GeV}^{-1}$. The shaded area on the top is the estimated AMS-02 and GAPS sensitivities.

The antideuteron flux with the 'med' and 'max' parameters are shown in figure 6.6, which corresponds to a typical uncertainty in the propagation. The uncertainties in the primary fluxes are larger than the uncertainties related to the coalescence models, and it it clear that a new complete study of the different parameters and recent constraints is needed. Alternatively, one may employ a complete numerical treatment using e.g. the GALPROP code [71]. The uncertainties related to the propagation of the secondaries are smaller than the uncertainties in the models. Two reasons for this are that we have not considered the uncertainties in the cross section parametrisations and the solar modulation, and that the parameter sets do not capture the entire uncertainty range. In any case, the uncertainties in the propagation of the secondaries are smaller than for the primaries, which may be expected as these spend a smaller time in the diffusion zone.

The new model with constant ζ is similar to the old model in all cases. The beam dependent ζ, on the other hand, differs notably from the other cases at $T \gtrsim 1\,\mathrm{GeV}/n$,

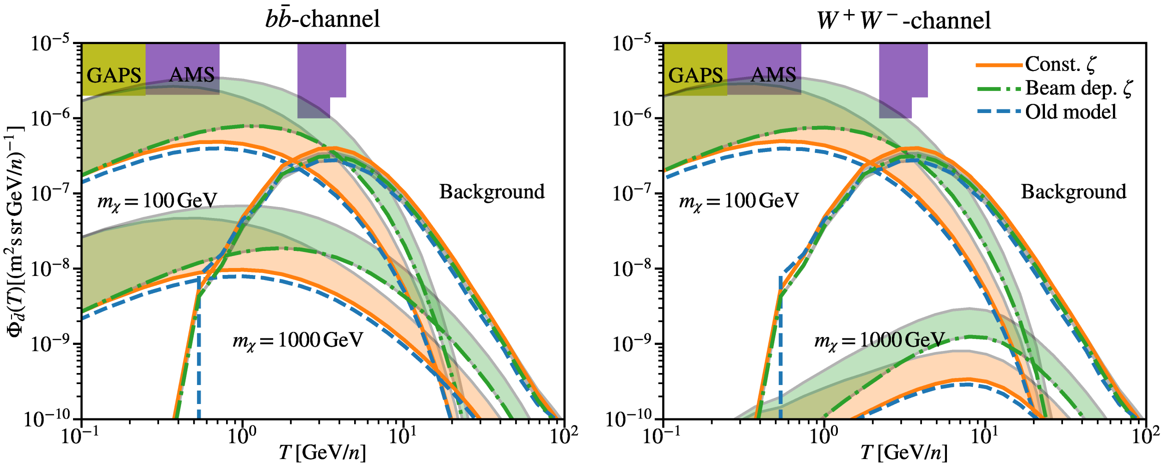

Figure 6.6: Estimated antideuteron flux on Earth from WIMP annihilations and secondary production for the considered benchmark cases and the 'med' propagation parameters. The shaded area around the flux for the new models corresponds the difference in the 'med' and 'max' parameters. The shaded area on the top is the estimated AMS-02 and GAPS sensitivities.

but by at most a factor 2–3. This is much smaller than the uncertainty related to the propagation and does not change current detection prospects significantly.

As apparent from figure 6.5, the flux at low T increases with decreasing WIMP mass. This includes for example also the antiproton flux. Thus, it is simple to contrive a DM candidate that can be detected by existing and previous experiments, which in turn implies that bounds on the WIMP properties can be made using cosmic ray antideuteron and antiproton. Optimistic scenarios, such as small DM masses, may overshoot the antiproton data. Therefore one should cross check optimistic approaches with current constraints (see for example [38, 39] for constraints from the AMS-02 antiproton data).

The estimated antihelium-3 flux on Earth for the same benchmark cases as in the antideuteron case is shown in figure 6.7 with uncertainties related to the models, and in figure 6.8 with the propagation uncertainties. For the uncertainty in the models, we use $\Delta\tau = 2\,\mathrm{GeV}^{-1}$ to account for a larger uncertainty in the helium-3 data. The uncertainties related to the old model have been omitted due to low statistics and to make the figures clearer. We estimated the antihelium-3 sensitivity of AMS-02 by multiplying the 18-year $^3\overline{\mathrm{He}}/\mathrm{He}$ sensitivity [82] by the measured helium flux by AMS-02 [83]. The increased sensitivity may explain why, as discussed in section 2.5, AMS-02 has reported the detection of eight possible antihelium events — one each year — while yet no antideuteron events. From figures 6.7 and 6.8, one can see that the secondary production is more likely to be detected than the considered WIMP particles. Reference [84] finds that some of the events may be accounted for in an optimistic approach, but it is hard to account for all of them. However, as can be seen in the figures, the antideuteron flux is closer to the expected detection efficiency, meaning that it is hard to explain the antihelium events from secondary production without any antideuteron events. In addition, the two reported antihelium-4 events should be even more suppressed compared to the six antihelium-3 events (a factor $\sim p_0^3 \sim 10^{-3}$), which is hard to explain even with an increased sensitivity. In any case, eight events are not enough to draw a firm conclusion and the detection of the events has not yet been published.

Finally, one can note that other works on the helium-3 flux usually use a value of p_0 that is about twice as large as ours [53, 54, 84]. The reason is that they use the value obtained for antideuterons using the ALEPH experiment and rescale it according to the the binding energies of the nuclei. Both the antideuteron production spectra measured by ALICE and the scaling of the new model we developed suggest that this value is too large.

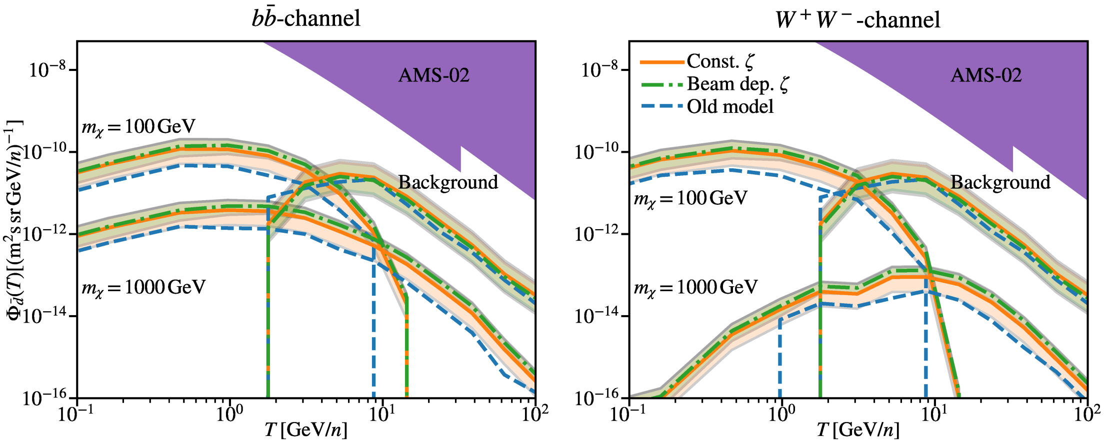

Figure 6.7: Estimated antihelium-3 flux on Earth from WIMP annihilations and secondary production for the considered benchmark cases and the 'med' propagation parameters. The shaded area around the flux for the new models corresponds the uncertainty $\Delta\sigma = 2\,\mathrm{GeV}^{-1}$. The shaded area on the top right is the estimated 18-year AMS-02 sensitivity.

The analyses performed here indicate that no antideuterons nor antihelium nuclei from secondary production and WIMP annihilations with $m_\chi \gtrsim 100\,\mathrm{GeV}$ should be detected by the 5-year sensitivity of AMS-02 and the long duration balloon flight of GAPS. In an optimistic approach, however, one may account for some events. In particular, some of the antihelium-3 events reported by AMS-02 may be accounted for by the secondary species, although it is hard to account for all of them. In any case, an updated sensitivity analysis including local effects such as geomagnetic deflection and atmospheric influences

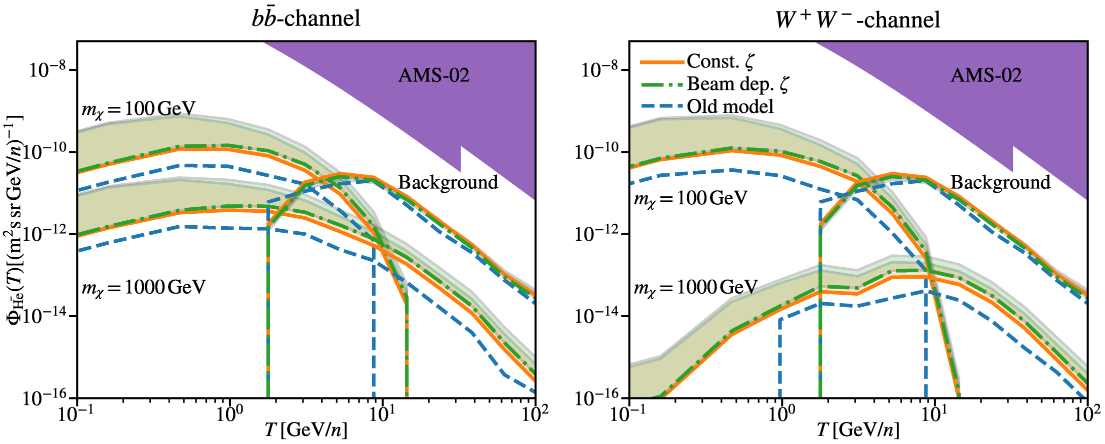

Figure 6.8: Estimated antihelium-3 flux on Earth from WIMP annihilations and secondary production for the considered benchmark cases and the 'med' propagation parameters. The shaded area around the flux for the new models corresponds the difference in the 'med' and 'max' parameters. The shaded area on the top right is the estimated 18-year AMS-02 sensitivity.

is highly needed in order to obtain a more certain conclusion. It it worth noting that our analyses contains several uncertainties related to amongst other the propagation model, nuclear cross sections, formation models, the DM distribution profiles and the sensitivity analyses. In order to improve the results, one should amongst other use a complete numerical treatment for the propagation. In addition, future experiments on the antinucleus production in pp and e^+e^- collisions may increase the accuracy of the formation models.

7 Summary and conclusion

The production of light (anti)nuclei in e^+e^-, pp and DM interactions is usually described by the coalescence model in a MC framework, thereby taking momentum correlations of the nucleons into account. This model is however phenomenological, lacks an underlying microphysical picture and the numerical value of its free parameter varies considerably between different experiments. In this thesis, we therefore developed a new coalescence model for light (anti)nuclei based on the Wigner function representation of the produced (anti)nuclei states. This approach allowed us to include in a semi-classical treatment both the size of the formation region and the momentum correlations of the nucleons forming the nuclei. The universal free parameter of the model is process dependent and accounts therefore naturally for the difference in the observed antideuteron yields in e^+e^- and pp collisions. Fitting the free parameter to recent experimental data on the antideuteron production in pp collisions at LHC yielded $\sigma_{(pp)} \simeq 7\,\mathrm{GeV}^{-1}$, which corresponds well to its physical interpretation as the size of the formation region of the nuclei. In turn, this value describes well the helium-3 production in pp collisions and antideuteron production in e^+e^- annihilations with $\sigma_{(e^+e^-)} = \sigma_{(pp)}/\sqrt{2} \simeq 1\,\mathrm{fm} \simeq 5\,\mathrm{GeV}^{-1}$ as expected from the physical interpretation. Even so, the exact value depends on amongst other the event generator used, meaning that it should be fine-tuned for each analysis. The model leads to a notable better fit to the considered experiments, but more importantly, the model includes a semi-classical description of the particles and has a microphysical picture that can be used to estimate the free parameter.

Several different approximations of the (anti)deuteron wave function and implementations of the spatial distribution factor ζ were examined. The fits to the antideuteron production in pp collisions at the ALICE experiment favoured the two-Gaussian wave functions. In the simplest case of a constant ζ, the results were similar to the old coalescence model, although the new models had a notably improved goodness-of-fit parameter. When the Lorentz transformation between the deuteron and lab frames was included in ζ, the fit to the data improved. In particular, the fits using a Lorentz contracted transverse size $\sigma_\perp$ of the formation region (ζ beam dependent) improved the fits to the ALICE antideuteron data significantly compared to the old model. Note that the best fit was obtained for the physically expected choices: the two-Gaussian wave function takes into account that the deuteron wave function has a distinct peak at $r = 0$, while $\sigma_\perp \approx R_p$ is expected to hold in the lab frame. Only an one-Gaussian wave function for helium-3 and tritium was studied, which may explain the difference in σ between the antideuteron and antihelium-3 data sets.

The new Wigner function based formation model was in turn used to estimate the antideuteron and antihelium-3 production in DM annihilations and secondary production in the Galaxy. The estimated secondary flux was similar for all considered models. The model with constant ζ gave similar primary fluxes to the old model. On the other hand, the beam dependent ζ gave primary fluxes that was at most a factor 2–3 larger than the old model for $T \gtrsim 0.1\,\mathrm{GeV}/n$, which is small compared to the uncertainties related to the propagation. Thus, the new model does not change the existing detection prospects significantly compared to the old model.

We find that the reported antihelium events by AMS-02 is difficult to account for by the secondary production and the considered WIMP masses $m_\chi = \{10^2, 10^3\}\,\mathrm{GeV}$ with the annihilation channels W^+W^- and $\bar{b}b$. Furthermore, we find that the detection prospects for both AMS-02 and GAPS are grim for the considered benchmark cases, both for antideuteron and antihelium. However, the analysis consists of several uncertainties related to the propagation and updated sensitivity analyses of the experiments are warranted.

In the future, the model should be fitted to a larger range of experiments such that a proper uncertainty in the free parameter σ can be determined. However, there are currently few available and relevant experiments with small uncertainties. In turn, in order to obtain a proper estimate for the antinucleus flux, a complete numerical treatment of the propagation should be used.

Appendix A

Special relativity

This chapter lists formulas and concepts from special theory of relativity that are used in this thesis. A more thorough discussion of the concepts and derivations can be found in any introductory textbook on gravitation or particle physics (see e.g. Refs. [14, 22, 44, 85]).

Line element, proper time and Lorentz transformation

The space-time coordinates of an event in an inertial reference frame S can be written as the four-vector $x^\mu = (t, \boldsymbol{x})$. The space-time coordinate of the same event in a coordinate system S' moving at constant velocity $\boldsymbol{v} = (v, 0, 0)$ with respect to S is given by the Lorentz transformation

$$x'^\nu = \Lambda^\nu_\mu x^\mu, \tag{A.1}$$

where Λ^ν_μ may be regarded as elements in the matrix

$$\Lambda = \begin{bmatrix} \gamma & -\gamma v & 0 & 0 \\ -\gamma v & \gamma & 0 & 0 \\ 0 & 0 & 1 & 0 \\ 0 & 0 & 0 & 1 \end{bmatrix}. \tag{A.2}$$

The Lorentz factor γ is as usual defined as

$$\gamma \equiv \frac{1}{\sqrt{1 - v^2}}. \tag{A.3}$$

A general four-vector is defined as a vector with four components that transforms as the space-time coordinates under Lorentz transformation.

The Lorentz transformation given above is a special case of the Lorentz boost in a general direction $\boldsymbol{n} = (n_x, n_y, n_z)$ given by the matrix

$$B(\boldsymbol{v}) = \begin{bmatrix} \gamma & -\gamma v n_x & -\gamma v n_y & -\gamma v n_z \\ -\gamma v n_x & 1 + (\gamma - 1) n_x^2 & (\gamma - 1) n_x n_y & (\gamma - 1) n_x n_z \\ -\gamma v n_y & (\gamma - 1) n_y n_x & 1 + (\gamma - 1) n_y^2 & (\gamma - 1) n_y n_z \\ -\gamma v n_z & (\gamma - 1) n_z n_x & (\gamma - 1) n_z n_y & 1 + (\gamma - 1) n_z^2 \end{bmatrix} . \tag{A.4}$$

In most cases, however, it is more convenient to rotate the coordinate system such that the transformation is on the form (A.2). The boost $B(\boldsymbol{v})$ constitutes together with three rotations $R(\theta)$ the Lorentz group.

The line element in Minkowski space is

$$\mathrm{d}s^2 = \mathrm{d}t^2 - \mathrm{d}x^2 - \mathrm{d}y^2 - \mathrm{d}z^2 = \mathrm{d}x^\mu \, \mathrm{d}x_\mu = \eta_{\mu\nu} x^\mu x^\nu \equiv \mathrm{d}\tau^2 \, , \tag{A.5}$$

which is invariant under Lorentz transformation. Due to this invariance, the proper time τ can be defined by the differential $\mathrm{d}s = \mathrm{d}\tau$ for time-like separated events. The proper time interval is in other words found by integrating $\mathrm{d}s$. For time-like separated event $\mathrm{d}s^2 < 0$, while for space-like separated events $\mathrm{d}s^2 > 0$.

Energy and momentum

The velocity $\boldsymbol{v}$ of a particle constitutes a part of the four-vector $u^\mu = \mathrm{d}x^\mu / \mathrm{d}\tau = \gamma(1, \boldsymbol{v})$ known as the four-velocity. The four-momentum is in turn defined as

$$p^\mu \equiv m u^\mu = (E, \boldsymbol{p}), \tag{A.6}$$

where m is the rest mass, $\boldsymbol{p} = \gamma m \boldsymbol{v}$ is the three-momentum of the particle and $E \equiv \gamma m$ is the relativistic energy. The energy can further be divided into a rest energy m and kinetic energy T as

$$E \equiv T - m, \tag{A.7}$$

where $T \equiv m(\gamma - 1)$. By taking the inner product of the four-momentum by itself, one obtains the important formula

$$p_\mu p^\mu = E^2 - \boldsymbol{p}^2 = m^2. \tag{A.8}$$

Note that this implies $E = |\boldsymbol{p}|$ for a massless particle.

All of the relativistic quantities that were introduced above reduces to the corresponding classical quantities in the low energy limit $v \ll 1$. The four-momentum is conserved and it transforms under the Lorentz transformation (A.1) as

$$p^\mu \to p'^\mu = (\gamma[E - v p_x], \gamma[p_x - E v], p_y, p_z) \, . \tag{A.9}$$

Lorentz invariant quantities

It is often convenient to consider Lorentz invariant quantities, such that one may evaluate an expression in any frame rather than performing the transformation. All four-vectors, for example, have the intrinsic property that their norm transforms as scalars under Lorentz transformations. In two-body particle scatterings, $1 + 2 \to 3 + 4$, it is often convenient to introduce the Mandelstam variables,

$$s \equiv (p_1 + p_2)^2 = (p_3 + p_4)^2, \tag{A.10a}$$

$$t \equiv (p_1 - p_3)^2 = (p_2 - p_4)^2, \tag{A.10b}$$

$$u \equiv (p_1 - p_4)^2 = (p_2 - p_3)^2, \tag{A.10c}$$

where p_i is the four-momentum of particle i. These quantities describes the momentum transfer in the three possible tree-level channels, and it can be shown that these transforms as scalars under Lorentz transformation.

As an example, consider the CoM energy of particle 1, $E_{1,\mathrm{CoM}}$. The CoM frame of particle 1 and particle 2 is characterised by $\boldsymbol{p}_{1,\mathrm{CoM}} = -\boldsymbol{p}_{2,\mathrm{CoM}}$, which implies that s can be expressed as $s = (E_{1,\mathrm{CoM}} + E_{2,\mathrm{CoM}})^2$. Finally, inserting $E_{2,\mathrm{CoM}}^2 = m_2^2 - m_1^2 + E_{1,\mathrm{CoM}}^2$ and solving for $E_{1,\mathrm{CoM}}$ gives

$$E_{1,\mathrm{CoM}} = \frac{s + m_1^2 - m_2^2}{2\sqrt{s}}. \tag{A.11}$$

Another important Lorentz scalar is $\mathrm{d}^3p\,/E$. One can use this to show that

$$\mathrm{d}^3p' = \frac{E'}{E}\,\mathrm{d}^3p = \gamma\left(1 - \frac{vp_x}{E}\right)\mathrm{d}^3p\,. \tag{A.12}$$

Appendix B

Wigner functions and Weyl transforms

The Wigner function and Weyl transform of operators offer an alternative formulation of quantum mechanics. In this chapter, some of the main features and characteristics of the time independent Weyl transformation and Wigner function for one-body systems in one dimension will be discussed, but the concepts can easily be generalised to more dimensions and to N particles. Most of this content is taken from Refs. [86, 87].

The one-dimensional one-particle Wigner function $f^{\mathrm{W}}(p,x)$ is defined as

$$f^{\mathrm{W}}(p,x) = \int \rho(x+y/2, x-y/2) e^{-\mathrm{i}py}\,\mathrm{d}y\,, \tag{B.1}$$

where $\rho(x,x')$ is the one-particle density matrix of the system in position space.[1] As a direct consequence $f^{\mathrm{W}}(p,x)$ is always real.[2] Note, however, that $f^{\mathrm{W}}(p,x)$ is by itself only a quasi-probability distribution since it, amongst other, in general can be negative. The inverse relation is

$$\rho(x,x') = \int \frac{\mathrm{d}p}{2\pi} f^{\mathrm{W}}\left(p, \frac{x+x'}{2}\right) \exp[\mathrm{i}p(x-x')]. \tag{B.2}$$

The Wigner function f^{W} thus contains the same information as ρ. A key property of the Wigner function is that the probability distribution in position space is found by integrating over the momentum,

$$\int f^{\mathrm{W}}(p,x)\frac{\mathrm{d}p}{2\pi} = \rho(x,x) = P(x), \tag{B.3}$$

while the probability distribution in momentum space is found by integrating over space the position,

$$\int f^{\mathrm{W}}(p,x)\,\mathrm{d}x = \rho(p,p) = P(p). \tag{B.4}$$

In other words, the Wigner function $f^{\mathrm{W}}(p,x)$ expresses the distribution in phase space corresponding to the density matrix in position space.

---

[1] This definition can be "derived" in the following way: Fourier transform $\rho(x,x')$ with respect to $y \equiv x - x'$ and then write $(x+x')/2$ as x.

[2] Take the complex conjugate of equation (B.1) and change the integration variable as $y \to -y$.

The Weyl transform of an operator $\hat{A}$ is defined as

$$\tilde{A}(x,p) = \int \mathrm{d}y\, e^{-\mathrm{i}py} \langle x + y/2|\, \hat{A}\, |x - y/2\rangle\,, \tag{B.5}$$

where the operator is expressed in position space through the matrix elements $\langle x|\, \hat{A}\, |x\rangle$. This can, however, equally well be expressed with matrix elements of the operator in momentum space. Comparison to the definition of the Wigner function (B.1) reveals that the Wigner function is simply the Weyl transform of the density operator. One important property of the Weyl transform is that the trace of the product of two operators, $\hat{A}$ and $\hat{B}$, can be expressed by the integral of the corresponding Weyl transforms,

$$\mathrm{tr}\Big(\hat{A}\hat{B}\Big) = \iint \mathrm{d}x\, \frac{\mathrm{d}p}{2\pi} \tilde{A}(x,p)\tilde{B}(x,p). \tag{B.6}$$

This property implies that the expectation value of A can be written as

$$\langle A\rangle = \mathrm{tr}\Big(\rho\hat{A}\Big) = \int f^{\mathrm{W}}(p,x)\tilde{A}(x,p)\, \mathrm{d}x\, \frac{\mathrm{d}p}{2\pi}. \tag{B.7}$$

Let now $\hat{A} = \hat{A}(\hat{x})$ be an operator which depends only on $\hat{x}$. In this case the Weyl transform becomes

$$\tilde{A}(x) = \int \mathrm{d}y\, e^{\mathrm{i}py} A(x - y/2)\delta(y) = A(x). \tag{B.8}$$

A similar result is obtained for $\hat{A} = \hat{A}(\hat{p})$ by using the Weyl transform in the momentum basis. More generally, the Weyl transform of an operator $\hat{A}(\hat{x},\hat{p})$ that can be written as a sum where each term is purely a function of $\hat{x}$ or $\hat{p}$, is simply the original function with $\hat{x}$ and $\hat{p}$ replaced by x and p: $\tilde{A}(x,p) = A(x,p)$. In this case, (B.7) simplifies to

$$\langle A(x,p)\rangle = \int A(x,p) f^{\mathrm{W}}(p,x)\frac{\mathrm{d}p}{2\pi}\, \mathrm{d}x\,. \tag{B.9}$$

Appendix C

Cross section parametrisations

In this chapter, we review the parametrisations for cross sections relevant for the antideuteron and antihelium-3 propagation in the Galaxy. This appendix follows the approach by Delahaye and Grefe [49] for antideuterons and Carlson et al. [53] for antihelium.

We redo the fits by Delahaye and Grefe. Data for the antiproton-proton total collision cross section was obtained from Ref. [14], and we account for uncertainties by adding the statistical and systematic errors in a quadrature. Possible correlation of statistical errors was not taken into account. There are no data on proton-antinucleus cross sections, and we therefore assume that $\sigma^i_{p\bar{N}} = \sigma^i_{\bar{p}N}$. Furthermore, there exists little data on the antiproton-deuteron cross sections, and some scaling of the antiproton-proton cross section will therefore be used. For the propagation of antinuclei, we need the annihilating antideuteron-proton cross section $\sigma^{\mathrm{ann}}_{\bar{N}p}(T) = \sigma^{\mathrm{tot}}_{\bar{N}p}(T) - \sigma^{\mathrm{el}}_{\bar{N}p}(T) - \sigma^{\text{non-ann}}_{\bar{N}p}(T)$. The final fits of the relevant cross sections is plotted in figure C.1.

Antiproton-proton cross section

There exists many different parametrisations for the antiproton-proton cross section, most of which are only applicable for high energies ($\sqrt{s} > 5\,\mathrm{GeV}$). One useful parametrisation valid for the entire domain of measurements is [88]

$$\sigma^{\mathrm{tot}}_{\bar{p}p} = \sigma^{\mathrm{tot}}_{\mathrm{asmpt}} \left[1 + \frac{c}{\sqrt{s - 4m_p^2 R_0^3(s)}} \left(1 + \frac{d_1}{\sqrt{s}} + \frac{d_2}{s} + \frac{d_3}{s^{3/2}} \right) \right], \tag{C.1}$$

where $s = 2m_p^2 + 2m_p\sqrt{m_p^2 + p_{\bar{p}}^2}$ is the CoM energy, and

$$\begin{aligned} \sigma^{\mathrm{tot}}_{\mathrm{asmpt}} &= \left[36.04 + 0.304 \ln^2(s/33.1\,\mathrm{GeV}) \right] \mathrm{mb}, \\ R_0^2 &= \left[0.40874044 \sigma^{\mathrm{tot}}_{\mathrm{asmpt}}\, \mathrm{mb}^{-1} - B(s) \right] \mathrm{GeV}^{-2}, \\ B(s) &= 11.92 + 0.3036 \ln^2(\sqrt{s}/20.74\,\mathrm{GeV}), \end{aligned}$$

where we have used the numerical values from Ref. [89]. The parameters c, d_1, d_2 and d_3 must be determined from a fit to experimental data. Note that both the high energy behaviour $\sigma^{\text{tot}}_{\text{asmpt}}$ and the slope of the diffraction cone $B(s)$ has been determined by fit to data.

We performed a χ^2-fit on available experimental data on $\bar{p}p$ cross section, as well pp cross section for $p_{\text{lab}} > 1\,\text{TeV}$. The result was

$$\begin{aligned} c &= (14.81 \pm 0.64)\,\text{GeV}^{-2}, d_1 = (-5.01 \pm 0.17)\,\text{GeV}, \\ d_2 &= (14.11 \pm 0.53)\,\text{GeV}^2, d_3 = (-13.95 \pm 0.50)\,\text{GeV}^3, \end{aligned} \tag{C.2}$$

giving a goodness-of-fit $\chi^2/\text{dof} = 2365/456$. Given that most of the data used do not state the systematic errors, this is acceptable.

For the elastic cross section $\sigma^{\bar{p}p}_{\text{el}}$, we use the parametrisation by Uzhinsky et al. [89]. Here, they use the same function (C.1) with an asymptotic behaviour[1]

$$\sigma^{\text{tot}}_{\text{asmpt}} = 4.5 + 0.101 \ln^2(s/33.0625\,\text{GeV}).$$

With this parametrisation, we found that

$$c = 60.78 \pm 3.00, d_1 = -7.03 \pm 0.16, d_2 = 23.68 \pm 0.52, d_3 = -25.37 \pm 0.56, \tag{C.3}$$

with a goodness-of-fit $\chi^2/\text{dof} = 165/138$, where we have included data for σ^{pp}_{tot} above $1\,\text{TeV}$.

For the non-annihilating cross section, we use the parametrisation by Ref. [60],[2]

$$\sigma^{\text{non-ann}}_{\bar{p}d}(p_{\bar{p}}) = 10^{-2.141+5.865\exp\{-\log_{10}(p_{\bar{p}}/\text{GeV})\}-3.398\exp\{-2\log_{10}(p_{\bar{p}}/\text{GeV})\}}. \tag{C.4}$$

Antideuteron-proton cross section

There are no experimental data for $\sigma^{\bar{d}p}_{\text{tot}}$. However, there exists some data for the charge conjugated reaction $\sigma^{\bar{p}d}_{\text{tot}}$ between $270\,\text{MeV}$ and $280\,\text{GeV}$ [14]. We therefore assume that $\sigma^{\bar{d}p}_{\text{tot}} = \sigma^{d\bar{p}}_{\text{tot}}$. Most previous work on the subject assume also that $\sigma^{\bar{d}p} \approx 2\sigma^{\bar{p}p}$, but as Ref. [49] notes, $2\sigma^{\bar{p}p}_{\text{tot}}$ is roughly 10 % larger than $\sigma^{\bar{d}p}_{\text{tot}}$ as expected due to Glauber screening. We will therefore follow Ref. [49] and rescale the high energy part of the antiproton-proton cross section data by a suitable factor.[3]

We found that equation (C.1) with the parameters (C.2) rescaled by a factor 1.89 gives a good fit on the antiproton-deuteron data above $5\,\text{GeV}$. The parametrisation for $\sigma^{\bar{d}p}_{\text{tot}}$ was in turn found by fitting (C.1) rescaled by the same factor to the experimental

---

[1] This numerical value is not explicitly given in the article, but can be found in the source code of the Geant4 software referred to in the article.

[2] This is not stated in the article, but written down by Delahaye and Grefe [49].

[3] Note that Ref. [49] uses different fit functions. They use the fit function by Ref. [88] for $\sigma^{\bar{p}p}_{\text{tot}}$ and a piecewise ansatz for $\sigma^{\bar{p}p}_{\text{tot}}$.

data. In addition to the $\sigma_{\mathrm{tot}}^{\bar{p}d}$ data, we included antiproton-proton data above 1 TeV and proton-proton data above 10 TeV. The result was

$$\begin{aligned} c = (16.00 \pm 0.38)\,\mathrm{GeV}^{-2}, d_1 = (-5.65 \pm 0.11)\,\mathrm{GeV}, \\ d_2 = (16.28 \pm 0.41)\,\mathrm{GeV}^2, d_3 = (-16.17 \pm 0.41)\,\mathrm{GeV}^3, \end{aligned} \tag{C.5}$$

with a goodness-of-fit $\chi^2/\mathrm{dof} = 388/144$.

There is not much data available for the elastic cross section. We therefore follow Ref. [49] and scale the parametrisation of $\sigma_{\mathrm{el}}^{\bar{p}p}$ to the available data [90]. We found that a scale factor 1.65 gave the best fit to the elastic antiproton-deuteron data.

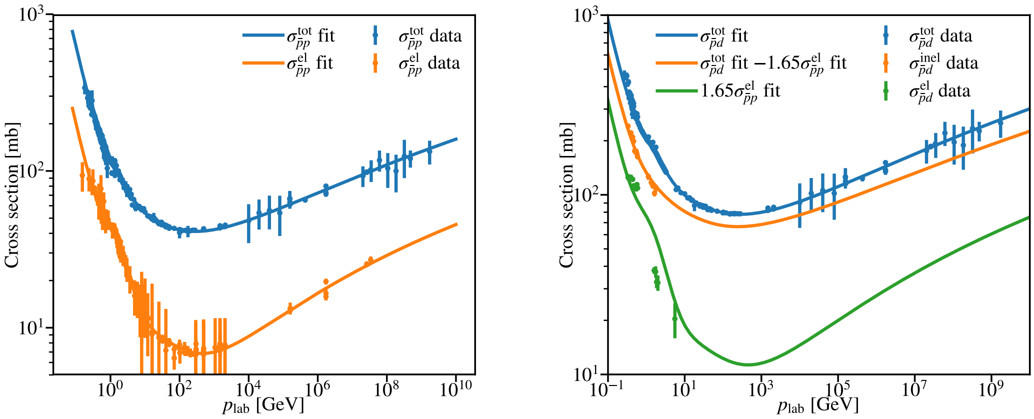

Figure C.1: Parametrisations and data for the total and elastic antiproton-proton cross sections (left) and total, elastic and inelastic antideuteron-proton cross sections (right). The parametrisations and the data are described in the text.

Antihelium-proton cross section

For the antihelium cross sections we use the parametrisations [53, 91]

$$\begin{aligned} \sigma_{\bar{p}A}^{\mathrm{tot}} =& A^{2/3}\left[48.2 + 19T^{-0.55} + (0.1 - 0.18T^{-1.2})Z \right. && \text{(C.6a)} \\ & \left. + 0.0012T^{-1.5}Z^2\right], && \text{(C.6b)} \\ \sigma_{\bar{p}A}^{\mathrm{ann}} =& \sigma_{\bar{p}A}^{\mathrm{tot}} - \sigma_{\bar{p}A}^{\text{non-ann, inel}}, && \text{(C.6c)} \\ \sigma_{\bar{p}A}^{\text{non-ann, inel}} =& \sigma_{pA}^{\text{non-ann, inel}}, && \text{(C.6d)} \\ \sigma_{pA}^{\text{non-ann, inel}} =& 45A^{0.7}\left[1 + 0.016\sin(5.3 - 2.63\ln A)\right] && \text{(C.6e)} \\ & \times \begin{cases} 1 - 0.62\mathrm{e}^{-T/0.2}\sin\left[10.9/(10^3T)^{0.28}\right] & \text{for } T \leq 3, \\ 1 & \text{for } T > 3, \end{cases} && \text{(C.6f)} \end{aligned}$$

where T is the kinetic energy per nucleon.

Bibliography

[1] F. Donato, N. Fornengo and P. Salati. "Anti-deuterons as a signature of supersymmetric dark matter". In: *Phys. Rev.* D62 (2000), p. 043003. arXiv: `hep-ph/9904481 [hep-ph]`.

[2] T. Aramaki et al. "Antideuteron Sensitivity for the GAPS Experiment". In: *Astropart. Phys.* 74 (2016), pp. 6–13. arXiv: `1506.02513 [astro-ph.HE]`.

[3] R. Battiston. "The Antimatter Spectrometer (AMS-02): A Particle Physics Detector in Space". In: *Nucl. Instrum. Meth.* 588.1 (Apr. 2008). Proceedings of the First International Conference on Astroparticle Physics, pp. 227–234.

[4] S. Ting. *Latest Results from the AMS Experiment on the International Space Station*. Talk at CERN Colloquium. May 2018.

[5] A. Schwarzschild and Č. Zupančič. "Production of Tritons, Deuterons, Nucleons, and Mesons by 30-GeV Protons on A1, Be, and Fe Targets". In: *Phys. Rev.* 129.2 (Jan. 1963), pp. 854–862.

[6] S. T. Butler and C. A. Pearson. "Deuterons from High-Energy Proton Bombardment of Matter". In: *Phys. Rev.* 129.2 (Jan. 1963), pp. 836–842.

[7] M. Kadastik, M. Raidal and A. Strumia. "Enhanced anti-deuteron Dark Matter signal and the implications of PAMELA". In: *Phys. Lett.* B683 (2010), pp. 248–254. arXiv: `0908.1578 [hep-ph]`.

[8] T. Aramaki et al. "Review of the theoretical and experimental status of dark matter identification with cosmic-ray antideuterons". In: *Phys. Rept.* 618 (2016), pp. 1–37. arXiv: `1505.07785 [hep-ph]`.

[9] S. Acharya et al. "Production of deuterons, tritons, ^{3}He nuclei and their antinuclei in pp collisions at $\sqrt{s} = 0.9$, 2.76 and 7 TeV". In: *Phys. Rev.* C97.2 (2018), p. 024615. arXiv: `1709.08522 [nucl-ex]`.

[10] S. Schael et al. "Deuteron and anti-deuteron production in e+ e- collisions at the Z resonance". In: *Phys. Lett.* B639 (2006), pp. 192–201. arXiv: `hep-ex/0604023 [hep-ex]`.

[11] R. Akers et al. "Search for heavy charged particles and for particles with anomalous charge in e^+e^- collisions at LEP". In: *Z. Phys.* C67 (1995), pp. 203–212.

[12] Y. Sofue. "Rotation and Mass in the Milky Way and Spiral Galaxies". In: *PASJ* 69.1 (Dec. 2017), R1. arXiv: `1608.08350 [astro-ph.GA]`.

[13] M. L. Kutner. *Astronomy: A Physical Perspective*. 2nd ed. Cambridge: Cambridge University Press, 2003.

[14] C. Patrignani et al. "Review of Particle Physics". In: *Chin. Phys.* C40.10 (2016), p. 100001.

[15] Y. Sofue, M. Honma and T. Omodaka. "Unified Rotation Curve of the Galaxy – Decomposition into de Vaucouleurs Bulge, Disk, Dark Halo, and the 9-kpc Rotation Dip –". In: *Publ. Astron. Soc. Jap.* 61 (2009), p. 227. arXiv: `0811.0859 [astro-ph]`.

[16] J. N. Bahcall and R. M. Soneira. "The Universe at faint magnetidues. 2. Models for the predicted star counts". In: *Astrophys. J. Suppl.* 44 (1980), pp. 73–110.

[17] J. F. Navarro, C. S. Frenk and S. D. M. White. "The Structure of cold dark matter halos". In: *Astrophys. J.* 462 (1996), pp. 563–575. arXiv: `astro-ph/9508025 [astro-ph]`.

[18] G. Bertone, ed. *Particle Dark Matter: Observations, Models and Searches*. Cambridge: Cambridge University Press, 2010.

[19] M. Cirelli et al. "PPPC 4 DM ID: A Poor Particle Physicist Cookbook for Dark Matter Indirect Detection". In: *JCAP* 1103 (2011). [Erratum: JCAP1210,E01(2012)], p. 051. arXiv: `1012.4515 [hep-ph]`.

[20] B. Ryden. *Introduction to cosmology*. 2nd ed. New York: Cambridge University Press, 2016.

[21] M. Bradac et al. "Revealing the properties of dark matter in the merging cluster MACSJ0025.4-1222". In: *Astrophys. J.* 687 (2008), p. 959. arXiv: `0806.2320 [astro-ph]`.

[22] M. Kachelriess. *Quantum Fields: From the Hubble to the Planck Scale*. Oxford Graduate Texts. Oxford: Oxford University Press, 2018.

[23] P. A. R. Ade et al. "Planck 2015 results. XIII. Cosmological parameters". In: *Astron. Astrophys.* 594 (2016), A13. arXiv: `1502.01589 [astro-ph.CO]`.

[24] R. Adam et al. "Planck 2015 results. I. Overview of products and scientific results". In: *Astron. Astrophys.* 594 (2016), A1. arXiv: `1502.01582 [astro-ph.CO]`.

[25] G. Jungman, M. Kamionkowski and K. Griest. "Supersymmetric dark matter". In: *Phys. Rept.* 267 (1996), pp. 195–373. arXiv: `hep-ph/9506380 [hep-ph]`.

[26] K. Griest and M. Kamionkowski. "Unitarity Limits on the Mass and Radius of Dark Matter Particles". In: *Phys. Rev. Lett.* 64 (1990), p. 615.

[27] J. Smirnov and J. F. Beacom. "TeV-Scale Thermal WIMPs: Unitarity and its Consequences". In: *Preprint* (Apr. 2019). arXiv: `1904.11503 [hep-ph]`.

[28] J. L. Feng, M. Kaplinghat and H.-B. Yu. “Sommerfeld Enhancements for Thermal Relic Dark Matter”. In: *Phys. Rev.* D82 (2010), p. 083525. arXiv: `1005.4678 [hep-ph]`.

[29] K. Kohri, D. H. Lyth and A. Melchiorri. “Black hole formation and slow-roll inflation”. In: *JCAP* 0804 (2008), p. 038. arXiv: `0711.5006 [hep-ph]`.

[30] A. Kashlinsky. “LIGO gravitational wave detection, primordial black holes and the near-IR cosmic infrared background anisotropies”. In: *Astrophys. J.* 823.2 (2016), p. L25. arXiv: `1605.04023 [astro-ph.CO]`.

[31] B. Carr et al. “Primordial black hole constraints for extended mass functions”. In: *Phys. Rev.* D96.2 (2017), p. 023514. arXiv: `1705.05567 [astro-ph.CO]`.

[32] M. Drewes. “The Phenomenology of Right Handed Neutrinos”. In: *Int. J. Mod. Phys.* 22 (2013), p. 1330019. arXiv: `1303.6912 [hep-ph]`.

[33] B. Famaey and S. McGaugh. “Modified Newtonian Dynamics (MOND): Observational Phenomenology and Relativistic Extensions”. In: *Living Rev. Rel.* 15 (2012), p. 10. arXiv: `1112.3960 [astro-ph.CO]`.

[34] O. Adriani et al. “Ten years of PAMELA in space”. In: *Riv. Nuovo Cim.* 40.10 (2017), p. 1. arXiv: `1801.10310 [astro-ph.HE]`.

[35] O. Adriani et al. “Cosmic-Ray Positron Energy Spectrum Measured by PAMELA”. In: *Phys. Rev. Lett.* 111 (2013), p. 081102. arXiv: `1308.0133 [astro-ph.HE]`.

[36] M. Boezio et al. “PAMELA and indirect dark matter searches”. In: *New J. Phys.* 11 (2009), p. 105023.

[37] M. Aguilar et al. “Antiproton Flux, Antiproton-to-Proton Flux Ratio, and Properties of Elementary Particle Fluxes in Primary Cosmic Rays Measured with the Alpha Magnetic Spectrometer on the International Space Station”. In: *Phys. Rev. Lett.* 117.9 (2016), p. 091103.

[38] A. Cuoco, M. Krämer and M. Korsmeier. “Novel Dark Matter Constraints from Antiprotons in Light of AMS-02”. In: *Phys. Rev. Lett.* 118.19 (2017), p. 191102. arXiv: `1610.03071 [astro-ph.HE]`.

[39] N. Fornengo, L. Maccione and A. Vittino. “Constraints on particle dark matter from cosmic-ray antiprotons”. In: *JCAP* 1404.04 (2014), p. 003. arXiv: `1312.3579 [hep-ph]`.

[40] A. Coogan and S. Profumo. “Origin of the tentative AMS antihelium events”. In: *Phys. Rev.* D96.8 (2017), p. 083020. arXiv: `1705.09664 [astro-ph.HE]`.

[41] V. Poulin et al. “Where do the AMS-02 antihelium events come from?” In: *Phys. Rev.* D99.2 (2019), p. 023016. arXiv: `1808.08961 [astro-ph.HE]`.

[42] R. K. Ellis, W. J. Stirling and B. R. Webber. *QCD and Collider Physics*. Cambridge: Cambridge University Press, 1996.

[43] G. Dissertori, I. G. Knowles and M. Schmelling. *Quantum Chromodynamics: High Energy Experiments and Theory*. Oxford: Oxford University Press, 2003.

[44] D. J. Griffiths. *Introduction to Elementary Particles*. 2nd ed. Weinheim: Wiley-VCH, 2011.

[45] T. Sjostrand, S. Mrenna and P. Z. Skands. "PYTHIA 6.4 Physics and Manual". In: *JHEP* 05 (2006), p. 026. arXiv: `hep-ph/0603175 [hep-ph]`.

[46] T. Sjöstrand et al. "An Introduction to PYTHIA 8.2". In: *Comput. Phys. Commun.* 191 (2015), pp. 159–177. arXiv: `1410.3012 [hep-ph]`.

[47] Y. L. Dokshitzer et al. *Basics of Perturbative QCD*. (Basics Of). France: Ed. Frontieres, 1991.

[48] C. B. Bräuninger and M. Cirelli. "Anti-deuterons from heavy Dark Matter". In: *Phys. Lett.* B678 (2009), pp. 20–31. arXiv: `0904.1165 [hep-ph]`.

[49] T. Delahaye and M. Grefe. "Antideuterons from Decaying Gravitino Dark Matter". In: *JCAP* 1507 (2015), p. 012. arXiv: `1503.01101 [hep-ph]`.

[50] R. Duperray et al. "Flux of light antimatter nuclei near Earth, induced by cosmic rays in the Galaxy and in the atmosphere". In: *Phys. Rev.* D71 (2005), p. 083013. arXiv: `astro-ph/0503544 [astro-ph]`.

[51] A. Ibarra and S. Wild. "Prospects of antideuteron detection from dark matter annihilations or decays at AMS-02 and GAPS". In: *JCAP* 1302 (2013), p. 021. arXiv: `1209.5539 [hep-ph]`.

[52] N. Fornengo, L. Maccione and A. Vittino. "Dark matter searches with cosmic antideuterons: status and perspectives". In: *JCAP* 1309 (2013), p. 031. arXiv: `1306.4171 [hep-ph]`.

[53] E. Carlson et al. "Antihelium from Dark Matter". In: *Phys. Rev.* D89.7 (2014), p. 076005. arXiv: `1401.2461 [hep-ph]`.

[54] M. Cirelli et al. "Anti-helium from Dark Matter annihilations". In: *JHEP* 08 (2014), p. 009. arXiv: `1401.4017 [hep-ph]`.

[55] R. Scheibl and U. W. Heinz. "Coalescence and flow in ultrarelativistic heavy ion collisions". In: *Phys. Rev.* C59 (1999), pp. 1585–1602. arXiv: `nucl-th/9809092 [nucl-th]`.

[56] K. Blum et al. "Cosmic rays, antihelium, and an old navy spotlight". In: *Phys. Rev.* D96.10 (2017), p. 103021. arXiv: `1704.05431 [astro-ph.HE]`.

[57] D.-M. Gomez-Coral et al. “Deuteron and Antideuteron Production Simulation in Cosmic-Ray Interactions”. In: *Phys. Rev.* D98.2 (2018), p. 023012. arXiv: `1806.09303 [astro-ph.HE]`.

[58] L. A. Dal and A. R. Raklev. “Alternative formation model for antideuterons from dark matter”. In: *Phys. Rev.* D91.12 (2015). [Erratum: Phys. Rev. D92, no.8, 089901 (2015)], p. 123536. arXiv: `1504.07242 [hep-ph]`.

[59] L. A. Dal and A. R. Raklev. “Antideuteron Limits on Decaying Dark Matter with a Tuned Formation Model”. In: *Phys. Rev.* D89.10 (2014), p. 103504. arXiv: `1402.6259 [hep-ph]`.

[60] L. A. Dal and M. Kachelriess. “Antideuterons from dark matter annihilations and hadronization model dependence”. In: *Phys. Rev.* D86 (2012), p. 103536. arXiv: `1207.4560 [hep-ph]`.

[61] S. Navin. “Diffraction in ALICE and Trigger Efficiencies”. PhD Thesis. Birmingham U., 2011.

[62] J. Adam et al. “Measurement of pion, kaon and proton production in proton–proton collisions at $\sqrt{s} = 7$ TeV”. In: *Eur. Phys. J.* C75.5 (2015), p. 226. arXiv: `1504.00024 [nucl-ex]`.

[63] M. Kachelriess, S. Ostapchenko and J. Tjemsland. “Alternative coalescence model for deuteron, tritium, helium-3 and their antinuclei”. In: *Submitted to JHEP* (2019). arXiv: `1905.01192 [hep-ph]`.

[64] V. I. Zhaba. “Deuteron: properties and analytical forms of wave function in coordinate space”. In: *arXiv e-prints* (2017). arXiv: `1706.08306 [nucl-th]`.

[65] R. Mattiello et al. “Nuclear clusters as a probe for expansion flow in heavy ion reactions at 10-A/GeV - 15-A/GeV”. In: *Phys. Rev.* C55 (1997), pp. 1443–1454. arXiv: `nucl-th/9607003 [nucl-th]`.

[66] S. G. Karshenboim et al., eds. *Precision Physics of Simple Atoms and Molecules*. Vol. 745. Lecture Notes in Physics. Berlin, Heidelberg: Springer Berlin Heidelberg, 2008.

[67] D. Maurin, R. Taillet and C. Combet. “Approximate formulae for exotic GCR antiprotons and anti-deuterons: Fluxes and astrophysical uncertainties”. In: *arXiv e-prints* (2006). arXiv: `astro-ph/0609522 [astro-ph]`.

[68] F. Donato, N. Fornengo and D. Maurin. “Antideuteron fluxes from dark matter annihilation in diffusion models”. In: *Phys. Rev.* D78 (2008), p. 043506. arXiv: `0803.2640 [hep-ph]`.

[69] A. Ibarra and S. Wild. “Determination of the Cosmic Antideuteron Flux in a Monte Carlo approach”. In: *Phys. Rev.* D88 (2013), p. 023014. arXiv: `1301.3820 [astro-ph.HE]`.

[70] R. Kappl, A. Reinert and M. W. Winkler. "AMS-02 Antiprotons Reloaded". In: *JCAP* 1510.10 (2015), p. 034. arXiv: `1506.04145 [astro-ph.HE]`.

[71] A. W. Strong, I. V. Moskalenko and O. Reimer. "Diffuse continuum gamma-rays from the galaxy". In: *Astrophys. J.* 537 (2000). [Erratum: Astrophys. J. 541, 1109 (2000)], pp. 763–784. arXiv: `astro-ph/9811296 [astro-ph]`.

[72] D. Maurin et al. "Cosmic rays below z=30 in a diffusion model: new constraints on propagation parameters". In: *Astrophys. J.* 555 (2001), pp. 585–596. arXiv: `astro-ph/0101231 [astro-ph]`.

[73] D. Maurin, R. Taillet and F. Donato. "New results on source and diffusion spectral features of galactic cosmic rays: I- B/C ratio". In: *Astron. Astrophys.* 394 (2002), pp. 1039–1056. arXiv: `astro-ph/0206286 [astro-ph]`.

[74] G. Di Bernardo et al. "Cosmic Ray Electrons, Positrons and the Synchrotron emission of the Galaxy: consistent analysis and implications". In: *JCAP* 1303 (2013), p. 036. arXiv: `1210.4546 [astro-ph.HE]`.

[75] M. Aguilar et al. "Precision Measurement of the Boron to Carbon Flux Ratio in Cosmic Rays from 1.9 GV to 2.6 TV with the Alpha Magnetic Spectrometer on the International Space Station". In: *Phys. Rev. Lett.* 117.23 (2016), p. 231102.

[76] F. Donato et al. "Anti-protons from spallations of cosmic rays on interstellar matter". In: *Astrophys. J.* 563 (2001), pp. 172–184. arXiv: `astro-ph/0103150 [astro-ph]`.

[77] R. Piessens et al. *Quadpack: A Subroutine Package for Automatic Integration*. Vol. 1. Springer Series in Computational Mathematics. Code available at `http://www.netlib.org/quadpack/`. Berlin Heidelberg: Springer-Verlag, 1983.

[78] E. Parker. "The Passage of Energetic Charged Particles through Interplanetary Space". In: *Planetary and Space Science* 13.1 (Jan. 1965), pp. 9–49.

[79] H. Moraal. "Cosmic-Ray Modulation Equations". In: *Space Sci. Rev.* 176 (2013), pp. 299–319.

[80] L. J. Gleeson and W. I. Axford. "Solar Modulation of Galactic Cosmic Rays". In: *Astrophys. J.* 154 (1968), p. 1011.

[81] T. Aramaki et al. "Antideuteron Sensitivity for the GAPS Experiment". In: *Astropart. Phys.* 74 (2016), pp. 6–13. arXiv: `1506.02513 [astro-ph.HE]`.

[82] A. Kounine. "Status of the AMS Experiment". In: *arXiv e-prints* (2010). arXiv: `1009.5349 [astro-ph.HE]`.

[83] M. Aguilar et al. "Precision Measurement of the Helium Flux in Primary Cosmic Rays of Rigidities 1.9 GV to 3 TV with the Alpha Magnetic Spectrometer on the International Space Station". In: *Phys. Rev. Lett.* 115.21 (2015), p. 211101.

[84] Y.-C. Ding et al. "Prospects of detecting dark matter through cosmic-ray antihelium with the antiproton constraints". In: *arXiv e-prints* (2018). arXiv: `1808.03612 [hep-ph]`.

[85] J. B. Hartle. *Gravity: An Introduction to Einstein's General Relativity*. San Francisco: Addison-Wesley, 2003.

[86] W. B. Case. "Wigner Functions and Weyl Transforms for Pedestrians". en. In: *Am. J. Phys.* 76.10 (Oct. 2008), pp. 937–946.

[87] R. P. Feynman. *Statistical Mechanics: A Set of Lectures*. Advanced Book Classics. Boulder, Colo: Westview Press, 1998.

[88] A. A. Arkhipov. "On global structure of hadronic total cross-sections". In: (1999). arXiv: `hep-ph/9911533 [hep-ph]`.

[89] V. Uzhinsky et al. "Antinucleus-nucleus cross sections implemented in Geant4". In: *Phys. Lett.* B705 (2011), pp. 235–239.

[90] A. Baldini et al. "Reaction 531 - 599". In: *Subvolume B*. Ed. by H. Schopper. Vol. 12b. Berlin/Heidelberg: Springer-Verlag, 1988, pp. 271–284.

[91] I. V. Moskalenko et al. "Secondary anti-protons and propagation of cosmic rays in the galaxy and heliosphere". In: *Astrophys. J.* 565 (2002), pp. 280–296. arXiv: `astro-ph/0106567 [astro-ph]`.